INSTITUTO SUPERIOR TÉCNICO
Universidade Técnica de Lisboa

Transmission of OFDM-UWB radio signals along multimode fiber in in-building networks

Filipa Andreia Fernandes Henriques

Dissertação para obtenção do Grau de Mestre em

Engenharia Electrotécnica e de Computadores

Júri

Presidente:	Prof. José Bioucas Dias
Orientador:	Prof. Adolfo da Visitação Tregeira Cartaxo
Vogal:	Prof. Paula Raquel Laurêncio

6 de Dezembro de 2010

Acknowledgments

First of all, I would like to thank to my supervisor, Professor Adolfo Cartaxo, for all the effort and availability for helping me to complete successfully my master thesis. I would also like to thank him for providing me access to all the materials I need during the development of this dissertation.

I would like to thank to my boyfriend André Neves for all the love, help, support and patience during this chapter of my life. There is no words to describe how much it meant to me.

I would like to thank to my parents and to my close family for always giving me what I needed to be happy. Their love and support helped me to get through the difficulties and always keep smiling.

I want to thank to my closest friends Rui Trindade, Nuno Couto, Filipe Wiener, André Chibeles, André Esteves, Gonçalo Carmo, João Cabrita and Clara Sá Couto for being the best friends I could have.

I would like to thank to Instituto de Telecomunicações (IT) for providing me a monthly scholarship and great facilities.

I would also like to thank to the PhD students Tiago Alves and Nelson da Costa, for all the availability and kindness they had in answer to all my questions and helped me as much as they can.

Abstract

Nowadays, in-building networks are facing a new challenge of upgrading their capacity to exceeding 1 Gbit/s, in order to provide high definition television (HDTV) and new advanced multimedia-based applications requiring even higher capacity than HDTV. The main characteristics of multimode fibers (MMF) like the low cost and their efficiency in short-range links make these fibers adequate to be used in in-building networks. The main features of orthogonal frequency division multiplexing (OFDM) ultra-wideband (UWB) signals like the low intersymbol interference (ISI) and the tolerance to multipath fading, make these signals appropriate to be used in MMF systems.

In this dissertation, the transmission of OFDM-UWB radio signals along multimode fibers in in-building networks is analysed. A numerical model of the fiber modal dispersion is developed in MATLAB. The transmission performance of the OFDM-UWB signals along the MMF is evaluated using the semi-analytical Gaussian approach and the maximum distance for single and multi-band transmission is assessed.

The numerical results show that the maximum transmission distance is very dependent on the power launching conditions, on the fiber length and on the number of sub-bands used. The maximum assessed distance ranges from 560 m (achieved for single-band transmission and for centred launching conditions) to less than 50 m (achieved for simultaneous transmission of 3 OFDM-UWB sub-bands and for centred launching conditions).

Keywords: Multimode optical fiber, OFDM-UWB signals, modal dispersion, launching conditions, in-building networks.

Resumo

Actualmente, as redes dentro de edifícios começam a ter necessidade de aumentar a sua capacidade para débitos superiores a 1 Gbit/s, devido ao aparecimento da televisão de alta definição (HDTV) e outras aplicações multimédia que exigem ainda mais capacidade que a HDTV. O custo reduzido das fibras multimodo (MMF) e a sua elevada capacidade em ligações de curto alcance, tornam a sua utilização vantajosa em redes ópticas dentro de edifícios. O uso de sinais de banda ultra-larga (UWB) e com multiplexagem ortogonal por divisão na frequência (OFDM) de banda ultra-larga (UWB) é adequado para a propagação em fibras multimodo devido à sua tolerância ao desvanecimento por multi-percurso e à sua baixa interferência intersimbólica.

Nesta dissertação, a transmissão de sinais rádio OFDM-UWB em fibras multimodo é analisada. Esta análise é feita através de um modelo numérico desenvolvido em MATLAB que simula a propagação nas fibras multimodo.O desempenho do sistema é avaliado através do método gaussiano semi-analítico e as distâncias máximas de transmissão para mono e multi-banda são identificadas.

Os resultados numéricos demonstram que a distância máxima de transmissão é fortemente dependente das condições de lançamento de potência, do comprimento da fibra e do número de sub-bandas usadas simultaneamente. A distância máxima de transmissão deste sistema varia entre 560 m (para transmissão numa única banda e lançamento de potência centrado) e menos de 50 m (para transmissão simultânea em três sub-bandas e lançamento de potência centrado).

Palavras-chave: Fibra óptica multimodo, sinais OFDM-UWB, dispersão modal, condições de lançamento, redes ópticas dentro de edifícios.

Contents

List of Figures

List of Tables

List of acronyms

3DHD	3D High definition
ADC	Analogue to digital converter.
BER	Bit error ratio
DAC	Digital to analogue converter
FFT	Fourier fast transform
HD	High definition
IFFT	Inverse fast fourier transform
IFT	Inverse fourier transform
ISI	Intersymbol interference
LASER	Light amplification by stimulated emission of radiation.
LED	Light emitting diode.
LPF	Low pass filter
MMF	Multimode fiber.
MZM	Mach-Zehnder modulator.
M-PSK	Phase Shift Key of order M
M-QAM	Quadrature Amplitude Modulation of order M
OFDM	Orthogonal frequency division multiplexing
OFDM-RX	OFDM-UWB receiver
OFDM-TX	OFDM-UWB transmitter
QPSK	Quadrature phase shift key modulation
P2P	Peer to peer
PIN	Positive-intrinsic-negative
PSD	Power spectral density
QAM	Quadrature amplitude modulation
RF	Radio frequency.

SMF Single mode fiber.

SNR Signal to noise ratio

TFI time-frequency interleaving

UWB Ultra wide band.

List of Symbols

0_{MMF}	Centre of Multimode fiber referential
0_{SMF}	Centre of Multimode fiber referential
A_{SMF}	Amplitude coefficient of the single mode fiber field
a	Modal amplitude
$B_{e,n}$	Equivalent bandwidth of the electrical noise
c_k	Data symbols at the kth subcarrier
$\mathbf{E}$	Electric field
$\mathbf{E}_{clad,n}$	Normal electric field component in the cladding
$\mathbf{E}_{co,n}$	Normal electric field component in the core
$\mathbf{E}_{clad,t}$	Transversal electric field component in the cladding
$\mathbf{E}_{co,t}$	Transversal electric field component in the core
$\mathbf{E}_{rad}$	Electric radiated modes
$\mathbf{E}_s$	Source electric field
$\mathbf{E}_t$	Transversal electric field component
$\mathbf{E}_z$	Longitudinal electric field component
EH	Hybrid modes
$\mathbf{e}$	Envelop of electric field
$\mathbf{e_t}$	Transversal of electric field
F_l	Normalized Bessel function of first kind of order l
f	Operating frequency
f_c	Central frequency of an OFDM-UWB signal
f_k	Frequency of the kth subcarrier
$f_{n,e}$	Electrical noise figure
$\mathbf{H}$	Magnetic field
$\mathbf{H}_{clad,n}$	Transversal magnetic field component in the cladding
$\mathbf{H}_{clad,t}$	Transversal magnetic field component in the cladding

$\mathbf{H}_{co,n}$	Transversal magnetic field component in the core
$\mathbf{H}_{co,t}$	Transversal magnetic field component in the core
$\mathbf{H}_{rad}$	Magnetic radiated modes
$\mathbf{H}_{s}$	Source magnetic field
$\mathbf{H}_{t}$	Transversal magnetic field component
$\mathbf{H}_{z}$	Longitudinal magnetic field component
H_{filter}	Transfer function of OFDM receiver low pass filter
H_{MMF}	Multimode fiber transfer function
HE	Hybrid modes
$\mathbf{h}$	Envelop of magnetic field
(h,b)	Vector coordinates which represents the distances between the MMF and the SMF centre in the MMF referential
$\mathbf{h}_{t}$	Transversal of magnetic field
J_l	Bessel function of first kind of order l
K_l	Modified Bessel function of the second kind of order l
K_b	Boltzman constant
k	Free-space wavenumber
κ^2	Transverse wave constant
L_{MMF}	Length of multimode fiber
l	Radial dependence of each propagated
M	Number of eigenvalue solutions available
m	Azimuthal dependence of each propagated
N_{sc}	Number of subcarriers
n	Refractive index profile
n_b	Number of subband used
n_{clad}	Refractive index of the cladding region
n_{co}	Refractive index of the core region
$n_{smf,clad}$	Refractive index of the cladding region of the single mode fiber
$n_{smf,co}$	Refractive index of the core region of the single mode fiber
P	Modal Power
P_{clad}	Existing power in the cladding region
P_{co}	Existing power in the core region
P_{coup}	Power coupling losses
P_{MMF}	Coupled power at the multimode fiber
P_{Noise}	Noise Power

P_{Signal}	Signal Power
P_{SMF}	Total power carried by the single mode fiber
P_{tot}	Total bound power
p	Fraction of power
$p_{noise,in}$	Thermal noise spectral density
R	Normalized radius
R_b	Bit ratio
R_p	Polarization resistance
$\mathbf{S}$	Pointing vector
$\mathbf{S}_z$	Longitudinal Pointing vector component
$\sqrt{S_c}$	Electrical power spectral density noise
T	Temperature
TE	Transversal electric modes
TH	Transversal magnetic modes
Ts	Symbol Period
U	Normalized transversal frequency in core region
V	Normalized frequency
V_{bias}	bias point
V_{OFDM}	Voltage of the OFDM-UWB signal applied to the MZM arms
V_{RMS}	Square mean root voltage
V_π	Voltage needed to cause a π phase shift in each MZM arm
X_{MMF}	X axis of Multimode fiber referential
X_{SMF}	X axis of Single mode fiber referential
x_{MMF}	Multimode fiber coordinates of a point P
x_{SMF}	Single mode fiber coordinates of a point P
W	Normalizer transversal frequency in cladding region
Y_{MMF}	Y axis of Multimode fiber referential
Y_{SMF}	Y axis of Single mode fiber referential
y_{MMF}	Multimode fiber coordinates of a point P
y_{SMF}	Single mode fiber coordinates of a point P
Z	Free-space Impedance
α	Attenuation coefficient
β	Propagation constant or eigenvalue
ε_0	Electric permittivity of free-space
λ	Wavelength

μ_0	Magnetic permeability of free-space
ρ	Fiber core radius
ρ_{clad}	Fiber cladding radius
$\rho_{smf,clad}$	Cladding radius of the single mode fiber
$\rho_{smf,co}$	Core radius of the single mode fiber
σ_c^2	Electrical noise or noise circuit
τ	Delay per unit
Δ	Profile height
Δ_t^2	Laplacian Vector
Ψ	Solutions of the scalar wave equation

Chapter 1

Introduction

In this chapter, the characteristics and current challenges of the optical fiber systems, namely the multimode ones, are presented and discussed. In Section 1.2, the motivation of this work is presented. In Section 1.3, the objectives and the structure of the dissertation are presented. The contributions of this work are presented in Section 1.4.

1.1 Scope of the work

The human being always tried to communicate at long distances, firstly using smoke signs or even letters, and more recently using telephones, internet and other even more sophisticated types of networks. As the ways of communicating evolved, the structure that supported those networks had to evolve as well. New communications systems started to emerge and soon it was possible to make a phone call that travelled around the world before reaching its destination, [1]. Unfortunately, the expansion of the network didn't bring only benefits. The increasing number of telephones and the disadvantages of using cooper wires was brought to the light. The fact that the attenuation introduced by the cooper wire network strongly increases with distance made undesirable the use of this kind of cables to bridges long distances. To overcome these difficulties, the coaxial cable started being used. During the following years, telecommunications networks continued to spread over the world. A great advance was made when the first photograph was transmitted at a long distance through a telephone line [2]. The era of the data communications has started. The internet started to rise and demand more bandwidth of the transporting networks [3] [4]. The data traffic increased and become dominant, due to the variability of the services offered. To face these new challenges, the actual coaxial networks were not enough. In the late 1970s, a new technology created to suppress the bandwidth needs had been invented: the optical fiber cables [5]. This new technology allowed to improve data rate transmission and the network capacity. Although the capacity in the access networks in already high, the tendency is that the demand for more

capacity continues growing. So, in order to keep up the capacity demands, the optical fiber network performance needs to be improved. The use of technologies like the orthogonal frequency division multiplexing (OFDM) ultra-wide band (UWB) signals, due to its main features like, tolerance to multipath and multi-band providing helps to enhance the multimode fiber (MMF) advantages in high-speed transmissions. The present dissertation focus on the problem of providing an efficient in-building network structure to support an advanced communication system. The main objective of this work is to study and characterize the OFDM-UWB signals transmission along multimode fiber in in-building networks.

1.2 Motivation

1.2.1 Evolution and challenges of the communication networks - Capacity demands

The human being is always communicating and trying to improve the existing communication systems, in order to do it better and faster. The first long-distance communication system of the modern era appeared about 1876 with the telephone invention by Alexander Bell [6]. This invention allowed people to communicate by voice over distances of thousands of kilometers. With the world spread of the telephone network, the high losses of the copper cables used in the transmission system and the increasing of the voice traffic communications, stimulated the search for more efficient ways of communicating. In 1970, the first optical fiber cables with attenuation losses of less than 20 dB/km [7] and its enhanced features like high bandwidth, immunity to cross-talk, small size and weight, low cost and high raw material availability, made optical fibers the main booster of the high-speed transmissions [8]. The benefits of the optical fiber networks became even more clear with the appearance of the internet. The internet appeared in the 1980s and quickly become one of the the most used technology used to transfer data in long distance communications [9]. In the last 30 years, the internet has been growing at unprecedented rates [10]. Figure 1.1 shows the growth of the internet users in the last 15 years.

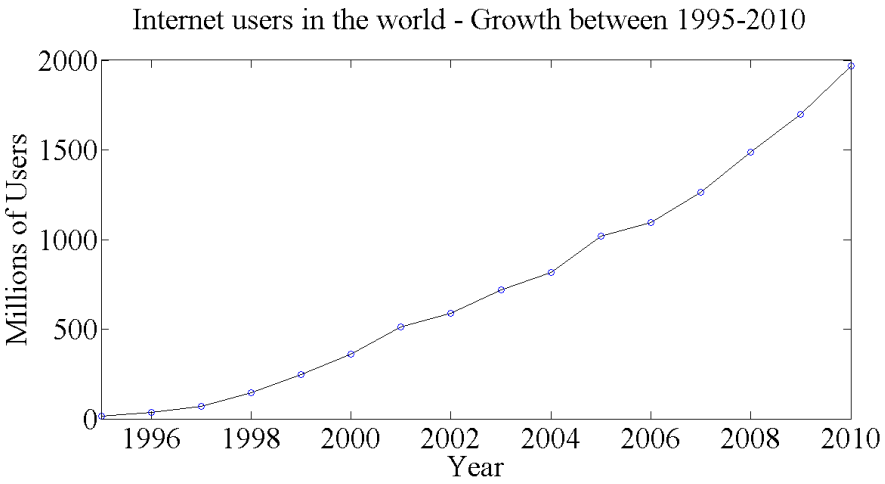

Figure 1.1: Growth of the internet users in the last 15 years (Source: `http://www.internetworldstats.com/emarketing.htm`). The 2010 results are relative to the estimated number of users in September of the same year.

Figure 1.1 shows that in the last 15 years, the number of internet users has always been increasing, reaching almost 2000 millions users by September 2010. It is also possible to see that the big boom of the internet was from 2000 to 2010, when the internet users increased in 1500 millions. The ever growing internet traffic demands a extremely high capacity of the optical networks.

The internet is the major traffic source of the current communication networks and the internet users are becoming more and more demanding, demanding higher upload capacities [10]. The peer-to-peer (P2P) technology present in the Emule and the social networks like the Facebook, twitter and Youtube had a major contribute to the increase of the optical networks traffic. In the mid 1990s, the download capacity in the access network was significantly higher than the upload capacity, since the internet was only used to access information. The appearance of peer-to-peer and social networks changed the current paradigm and stimulated the users to be more content producers. The current internet users like to share all the available resources with each others like video, music, data, photos, games and text. And they want to do it as faster and as much as they can. This new internet culture demands a more symmetric network system, that can satisfy the needs of every single user, without limiting the overall system. So, it is necessary to increase the up and down-link capacity of the current networks.

The high-definition television (HDTV) and the interactive contents offered by the principal TV operators, also demand a higher capacity of the current networks. Nowadays, concepts like triple-play (telephone, television and internet) are being sold by the major telecommunication companies. These services usually use high speed internet connections that can go up to 200 Mbps [11]. The television operators offer a large number of HD channels [12], that is likely to grow in the next years. Another

feature that will increase the data traffic in the networks is the widespread of the 3-Dimensional (3-D) technology, or even the 3D-HD technology [13]. Some of the portuguese telecommunication operators are also starting to offering 3-D contents, with experimental transmissions of some major events like the 3-D transmission of the World-cup 2010 [14]. When these operators start to transmit most of their contents in 3-D, the transport network will have to support a even bigger amount of traffic.

The introduction of interactive channels by the TV operators gives to the user the possibility to participate actively in the program he/she is watching. This fact will also contribute to increase the data traffic, not only in the downstream, but also in the upstream. Another service that is responsible for the increasing of data in the networks is the video-on-demand. This service gives the user the possibility to watch a movie, and to do so, the movie has to be downloaded to the users television set, [15]. If the most of the users decided to ask for a video-on-demand in the same building, the current network does not have capacity to support this amount of traffic. Figure 1.2 shows an example of the challenge of the current in-building networks.

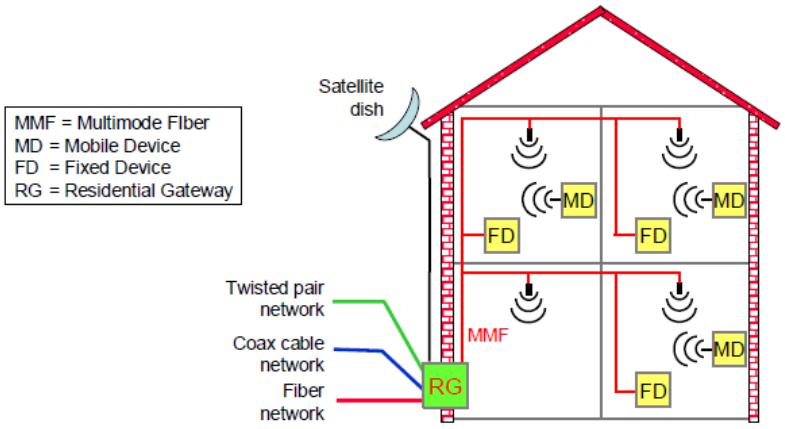

Figure 1.2: Representation of an in-building network (Source: `http://alexandria.tue.nl/extra2/200712406.pdf`).

Figure 1.2 shows the paradigm of the current networks: the co-existence of old (satellite, copper and coax cables) and the new (optical fibers) transmission systems must be able to support the new services provided by the telecommunication operators.

All the subjects approached in this text show that there is a clear need of increasing the capacity of the current network systems. The introduction of new services like the P2P, Youtube, HD and 3D-HD television generated a large amount of data that didn't existed before. These new services compelled the networks to improve in order to face the challenges brought by these technologies. The use of advanced

transmission systems based on optical fibers networks may be the answer for this problem.

1.2.2 Optical fiber networks - Why to use multimode fibers?

In the last few years, the optical fiber networks have been gradually replacing the cooper networks, due to its increased transmission capabilities like high available bandwidth, low transmission losses and immunity to electromagnetic interference. There are two types of optical fibers: the single-mode fiber (SMF) and multimode fiber (MMF). The single-mode fiber has a core diameter small enough to only support one mode, in opposition to the multimode fiber, which has a large core that can support hundreds of modes in a single fiber [16]. The existence of more than one propagation mode in MMF leads to the degradation of the performance of this type of fiber in long-distance transmission. Nevertheless, the MMF are commonly used in short range optical networks. Another advantage of the multimode fibers is that they are easy to handle, since they have a larger core size which gives more tolerance in the required alignment for the light coupling in the MMF [17]. The multimode fiber has been widely used in in-building and in-campus networks. The reason for that is that, in these networks, the length of fiber required to complete the connections is smaller than a few hundred meters long, [17], which is perfectly adequate to the MMF characteristics. The importance of providing low cost solutions made clear the necessity of using MMF instead of other fiber solutions.

1.3 Objectives and structure of the dissertation

The main objectives of this dissertation are:

- To study and characterize the OFDM-UWB radio signals, in the time and frequency domain;
- To study the multimode fiber propagation theory and develop a numerical model based on that;
- To analyze the impact of the fiber transmission and the power launching conditions on the performance of the system, by evaluating the degradation of the quality of the received signal and the bit error probability;
- To assess the maximum transmission distance in single- and multi-channel OFDM-UWB systems along multimode fiber.

This dissertation is organized in five chapters.

In Chapter 1, the evolution and the challenges of the current optical networks are presented and analysed. The main characteristics of the multimode fibers are presented, namely why they are adequate to be used in in-building networks. The objectives and the dissertation organization are also described in this chapter. Finally, the main contributions of this work are presented.

In Chapter 2, the description of the OFDM-UWB transmission system is presented and analysed. They main components of the system are presented and the performance of the OFDM-UWB system is analysed in back-to-back configuration.

In Chapter 3, the multimode fiber propagation model is presented and discussed. A numerical model is developed and the multimode fiber power transfer function is analysed for different power launching conditions.

In Chapter 4, the performance of the OFDM-UWB system along multimode fiber is presented and discussed. The maximum transmission distances is assessed for different launching conditions and for single- and multi-band transmission.

In Chapter 5, the final conclusions of this work and suggestions for future work on this subject are presented.

1.4 Contributions of this work

The main contributions of this work are:

- demonstration of the impact of the multimode fiber propagation on the performance of OFDM-UWB signals;
- development of a multimode fiber propagation numerical model based on the modal dispersion;
- study of the contribution of each existing mode in the multimode fiber, to the multimode fiber transfer function;
- demonstration of the impact of power launching conditions on the multimode fiber transfer function and on the performance of the overall system;
- demonstration of the reliability of the OFDM-UWB transmission system along the multimode fiber for single-band transmission;
- demonstration of the impact of multi-band propagation on the performance of the overall system.

Chapter 2

OFDM-UWB system description and analysis

In this chapter, the main components of the OFDM-UWB system are characterized. The block diagram of the overall system used in this work is presented in Section 2.1. In Section 2.1.1, the OFDM-UWB signals are presented. The OFDM-UWB transmitter is shown and analysed in Section 2.1.2. The Mach-Zehnder modulator is presented in Section 2.1.3. The PIN is presented in Section 2.1.4. In Section 2.1.5, the OFDM-UWB receiver is presented and studied. The system's performance in back-to-back configuration is shown in Section 2.2.

2.1 Description of the OFDM-UWB system

In Figure 2.1, a block diagram of the OFDM-UWB system used in this work is presented.

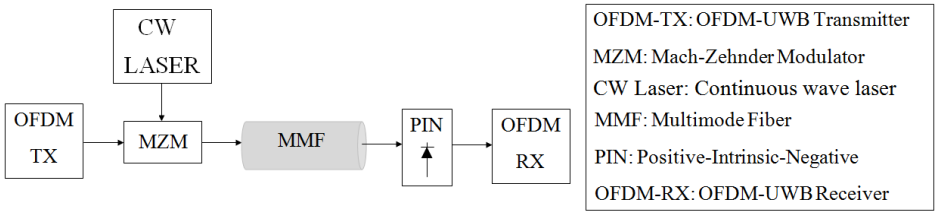

Figure 2.1: Block diagram of the OFDM-UWB system used in this work.

The first element of the OFDM-UWB system is the transmitter, where the OFD-UWB signals are generated. Once these signals are built, the next step is to do the electro-optic conversion through the Mach-Zehnder modulator, which allows the signal to be transmitted over the multimode optical fiber. At the fiber's output, the signal is converted from optic to electric by the Positive-Intrinsic-Negative (PIN), and it is ready to be processed by the OFDM-UWB receiver. The main components of this system are

presented with more detail in the following sections.

2.1.1 OFDM-UWB signals

Ultra wide band (UWB) technology is being widely recognised due to its main features like low self-interference, tolerance to multipath fading and low probability of interception [18]. This technology is being used for high bitrate high definition (HD) in picocells, replacing the existing HD cabling [19]. UWB is a radio modulation technique with 500 MHz minimum bandwidth or, at least, 20% greater than the centre frequency operation [20]. There are two UWB signal formats: Impulse Radio (IR) and OFDM-UWB [21]. In this work, it is used the OFDM-UWB format, since it presents a better performance for high bit rates [22].

This modulation format distributes the data over a large number of orthogonal subcarriers that are spaced apart at frequencies multiples of inverse of the symbol periods, T_s. The main idea is that the transmission channel affects each sub-carrier as a flat channel [23]. Some of the benefits of using OFDM modulation are high-spectral efficiency, resiliency to radio frequency (RF) interference and lower multi-path distortion [24]. The OFDM-UWB approach divides the UWB spectrum (3.1 to 10.6 GHz) into 14 sub-bands, each with 528 MHz wide [22], as it possible to see in Figure 2.2.

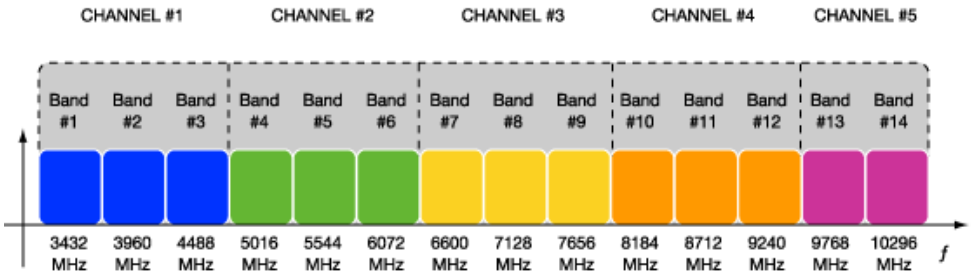

Figure 2.2: Standardized sub-bands division.

The center frequency of OFDM-UWB signal in each 528-MHz band is given by:

$$f_{RF}[n_b] = 2904 + 528n_b, \qquad [MHz] \;\; n_b = 1,2,\ldots,14 \;\; [MHz] \tag{2.1}$$

where n_b is the number of the sub-band used.

Each OFDM-UWB symbol is composed by 128 sub-carriers, carrying different types of information:

- 100 data sub-carriers, using simple modulations formats such as M-PSK and M-QAM;
- 12 pilots sub-carriers, which are used for distortion equalization;

- 10 guard sub-carriers, used for different purposes;
- 6 null sub-carriers, located at band edges in order to relax electrical filter requirements [25];

In this work, the 100 data sub-carriers are using QPSK modulation. The OFDM-UWB symbol results from the superposition of all the sub-carriers used and has the duration of T_s seconds. The OFDM signal $s(t)$ is constructed using a inverse fourier transform (IFT) [26]:

$$s(t) = \sum_{k=1}^{N_{sc}} c_k s_k(t), \tag{2.2}$$

with

$$s_k(t) = e^{j2\pi f_k t}\Pi(t),\ \Pi(t) = \begin{cases} 1\ , & 0 < t < T_s \\ 0\ , & t \leq 0\ ,\ T_s < t \end{cases}$$

where N_{sc} represents the number of sub-carriers, c_k represents the data symbols at the k^{th} sub-carrier and f_k represents the frequency of the sub-carrier number k.

Figure 2.3 shows how the OFDM-UWB symbols are interleaved over different sub-bands, across time and frequency domain. The first OFDM-UWB symbol is transmitted on channel number 1, the second OFDM-UWB symbol is transmitted on channel number 3, the third OFDM-UWB symbol is transmitted on channel number 2, the fourth OFDM symbol is transmitted on channel number 1, and so on [27]. In this example, the time-frequency interleaving (TFI) is performed across just three OFDM-UWB symbols (in practice the TFI is much longer).

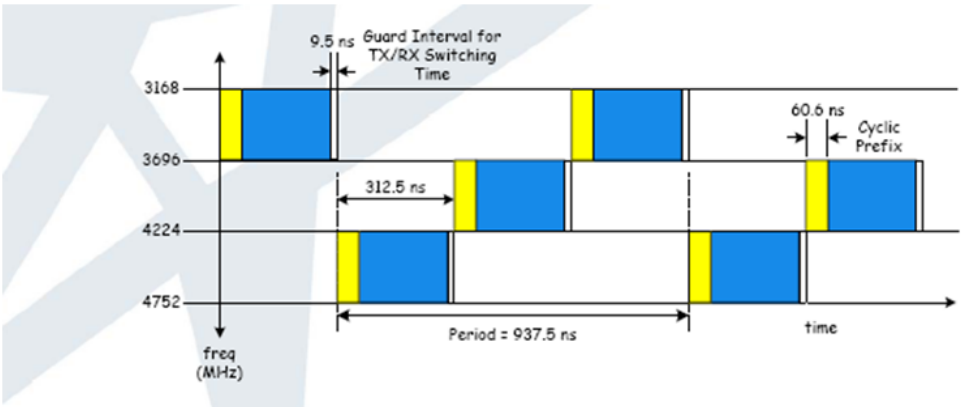

Figure 2.3: Representative scheme of the time-frequency interleaving of the OFDM-UWB symbols.

Figure 2.3 also shows that the OFDM-UWB symbol period has the duration of 312.5 ns. The cyclic prefix (CP) used to mitigate the intersymbol interference (ISI) is appended to the OFDM-UWB symbol. The guard-time (G) is inserted at the end of the OFDM-UWB block, to ensure that only a single radio frequency (RF) is transmit and there is sufficient time for the transmitter and receiver to switch to the

next channel [27]. The cyclic prefix duration is $T_{CP} = 60.6$ ns and the guard-time duration is $T_G = 9.47$ ns. The OFDM-UWB modulation/demodulation is implemented using the inverse fast Fourier transform (IFFT)/fast Fourier transform (FFT), respectively.

2.1.2 OFDM-UWB transmitter

A block diagram of the OFDM-UWB transmitter is presented in Figure 2.4.

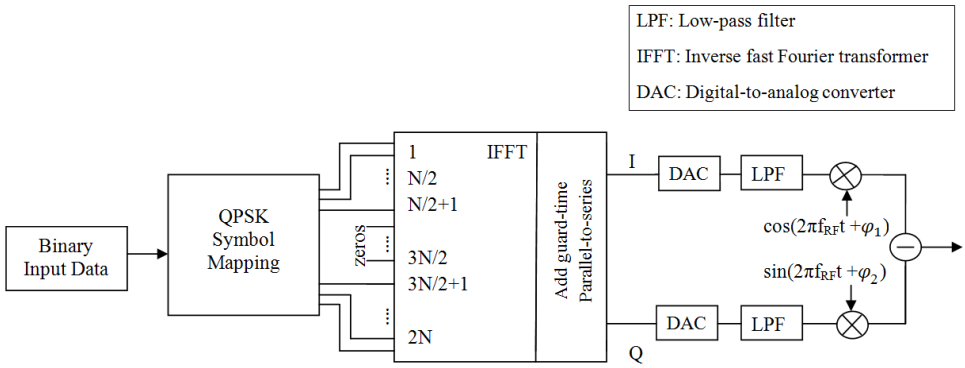

Figure 2.4: Block diagram of the OFDM-UWB transmitter.

An input binary deBruijn sequence with 2^{13} symbols is converted into a complex-valued sequence using QPSK modulation. Figure 2.5 show the QPSK constellation generated at the OFDM-UWB transmitter input.

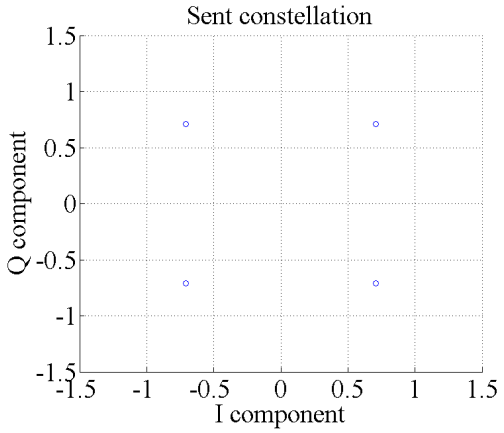

Figure 2.5: QPSK constellation generated at the OFDM-UWB transmitter.

After that, the complex-valued signal is converted from series to parallel and an inverse fast Fourier transform (IFFT) is applied. At this point, the resulting complex signal is converted again but this time from parallel to series. The transmitted signal is now splitted in an in-phase (I) component and in a quadrature (Q) component, which contains the real and the imaginary values of the original signal,

respectively. These components are first converted to the analogue domain using digital-to-analogue (DAC) converters. The analogue signals are then used to modulate cosine and sine waves at the carrier frequency, respectively. A low pass filter (LPF) is now applied to each component, in order to reduce the influence of the aliasing components on the system performance [28]. After that, the I and Q components are up-converted to the carrier frequency of the UWB sub-band used. At the OFDM-UWB transmitter, 32 OFDM-UWB symbols are generated.

The bit rate of the system is given by [26]:

$$R_b = \frac{N_{sc}}{T_s} \log_2 M \tag{2.3}$$

So, for $N_{sc} = 100$, $T_s = 312.5$ ns and $M = 4$, the system presents a bit rate of 640 Mbit/s.

Figure 2.6 shows the OFDM-UWB signal at the transmitter output, in the time and frequency domain, for the first UWB sub-band ($f_{RF} = 3.4$ GHz). In the numerical simulation, a 6^{th} order Bessel filter with a -3 dB bandwith of 400 MHz is used.

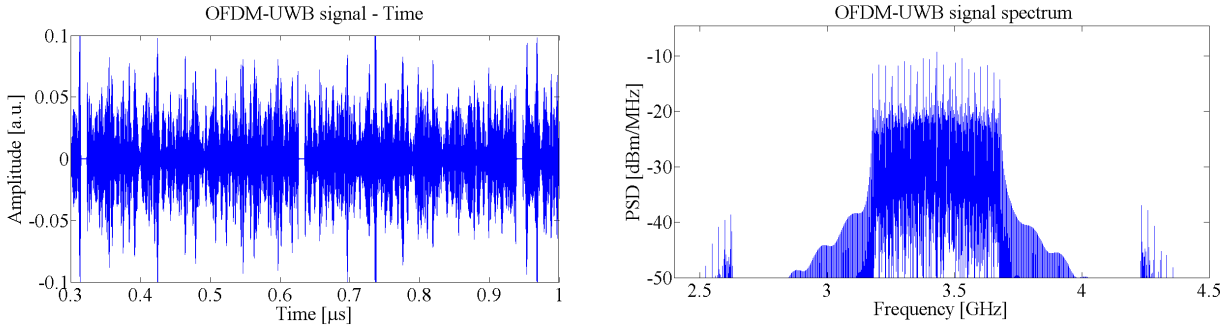

(a) Time domain.

(b) Frequency domain.

Figure 2.6: OFDM-UWB signal at the transmitter's output, in the time and frequency domain.

In the time domain in Figure 2.6, it is possible to identify some OFDM-UWB blocks. In the frequency domain, it possible to see that the signal is centred at the carrier frequency, f_{RF}.

2.1.3 Mach-Zehnder modulator

The Mach-Zehnder modulator (MZM) performs the electro-optic conversion of the transmitted signal, by modulating the amplitude of the carrier frequency. The envelope of the electric field at the modulator output is given by [29]:

$$E(t) = E_0(t) \cos\left(\frac{\pi}{2V_\pi}(2V_{OFDM}(t) - V_{bias})\right) \tag{2.4}$$

where $E_0(t)$ represents the electric field at the modulator input, V_π represents the voltage needed to cause

a π phase shift in each MZM arm, $V_{OFDM}(t)$ represents the voltage of the OFDM-UWB signal applied to the MZM arms and V_{bias} represents the bias point voltage.

The optical carrier is modulated according to the modulation index used. This parameter is given by $m = \frac{V_{RMS}}{V_{bias}}$, where V_{RMS} represents the root mean square (rms) voltage of the OFDM-UWB signal. So, the modulation index determines the fraction of the OFDM-UWB signal used to modulate the transmitted information. The higher is the modulation index, the higher will be the distortion of the signal, so it is convenient to choose a modulation index adequate to the type of system used. Table 2.1 show the values of V_π and V_{bias} used to perform the numerical simulations presented in this dissertation. These values were optimized in order to provide a good quality of the received signal when it is transmitted along the multimode fiber. The optimizations performed to the MZM modulator are presented in the Appendix E.

Table 2.1: Parameters used for simulate the Mach-Zehnder modulator.

MZM Parameters	
V_π [V]	5
V_{bias} [V]	2.5
m [%]	10

Figure 2.7 shows the modulator output for the first UWB sub-band.

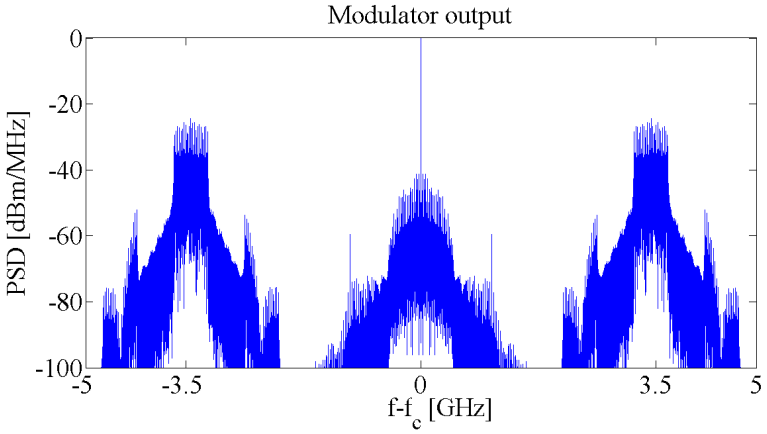

Figure 2.7: Mach-Zehnder modulator output for the first UWB sub-band, where f_c represents the optical carrier frequency.

The PSD at the modulator output presented in Figure 2.7 shows the OFDM-UWB signal centred at $-f_{RF}$ and f_{RF}.

2.1.4 PIN

The PIN performs the opto-electric conversion of the received signal. First, the signal is photodetected and then is pre-amplified and filtered, before it reaches the OFDM-UWB receiver. A simplified scheme of the system PIN + pre-amplifier is presented in Figure 2.8.

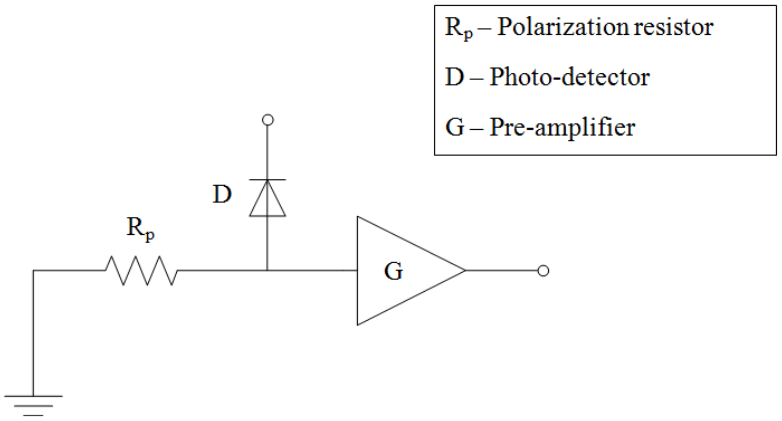

Figure 2.8: Block diagram of the system PIN + pre-amplifier.

The polarization resistor and the pre-amplifier introduce electrical noise into the system, due to the existence of resistive and active elements on them, respectively. This electric noise is also known as circuit noise and is represented by σ_c^2. The noise associated with the polarization resistor R_p, can be determined by the current variance associated with it [30]:

$$\sigma_b^2 = \frac{4k_BT}{R_p}B_{e,n} \tag{2.5}$$

where k_B is the Boltzman constant, T is the temperature (in Kelvin degrees), R_p is the polarization resistor at the pre-amplifier input and $B_{e,n}$ is the equivalent bandwidth of the electric noise. The pre-amplifier noise can be described by its noise figure, $f_{n,e}$. So, the total noise circuit of the system is given by the contributions of the resistive noise and of the amplifier noise figure:

$$\sigma_c^2 = \sigma_b^2 \cdot f_{n,e} = \frac{4k_BT}{R_p} \cdot f_{n,e} \cdot B_{e,n} \tag{2.6}$$

The expression of the circuit noise does not take into account the gain of the pre-amplifier. This decision does not affect the performance of the system, since this gain is not considered in the transmission of the OFDM-UWB signal [30]. Finally, from the analysis of the Equation 2.6 ,it is possible to determine the power spectral density (PSD) of the circuit noise, once $B_{e,n}$ is the equivalent bandwidth of the electric noise:

$$S_c(f) = \frac{\sigma_c^2}{B_{e,n}} = \frac{4k_B T}{R_p} f_{n,e} \tag{2.7}$$

Table 2.2 shows the numerical values used for the circuit noise of the OFDM-UWB system.

Table 2.2: Parameters used for the electrical noise.

Parameters	
Boltzman constant	$k_B = 1.38 \times 10^{-23}$ J/K
Polarization resistor	$R_p = 50\ \Omega$
Temperature	$T = 290$ K
Noise figure	$f_{n,e} = 10$
Electrical PSD noise	
$S_c(f) = 3.2 \times 10^{-21}$ A^2/Hz	

2.1.5 OFDM-UWB receiver

A block diagram of the OFDM-UWB receiver is shown in Figure 2.9.

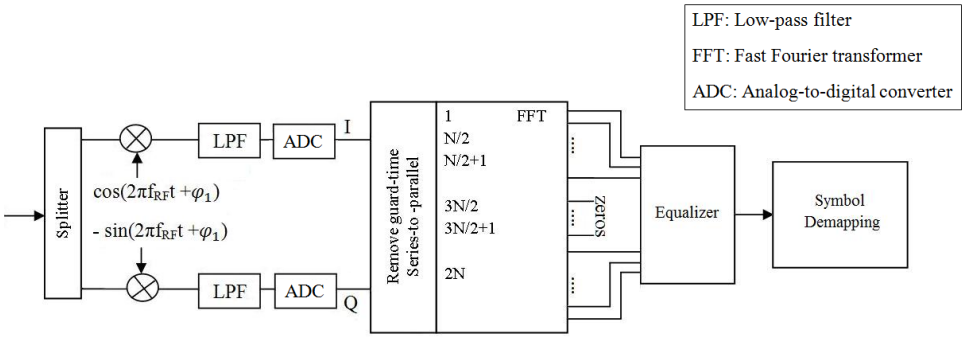

Figure 2.9: Block diagram of the OFDM-UWB receiver.

At the OFDM-UWB receiver firstly, the transmitted signal is splitted in two components: an in-phase component, which leads to the real values of the original signal and a quadrature component, which leads to the imaginary values of the original signal. After this, each of these signals is down-converted and filtered. Figure 2.10 show the received I and Q components of the transmitted OFDM-UWB signal. The numerical results presented in Figure 2.10 are performed for 32 OFDM-UWB symbols, using a 6^{th} order Bessel filter with a -3 dB bandwidth of 400 MHz, and for $f_{RF} = 3.4$ GHz.

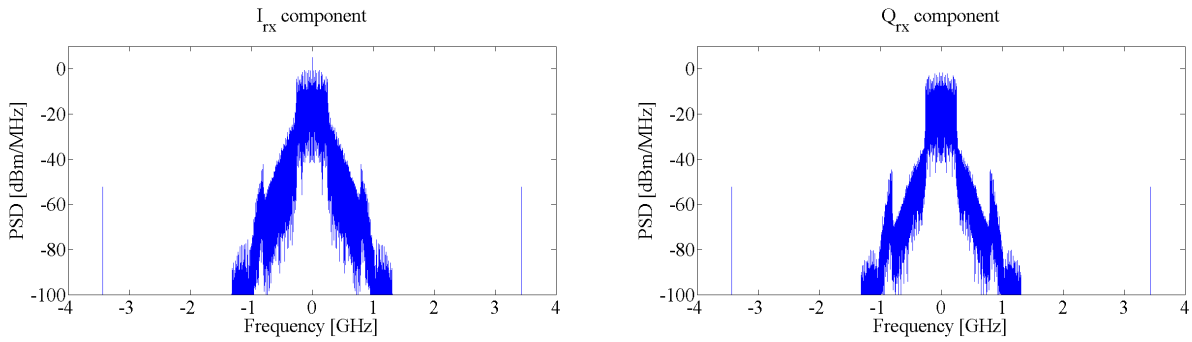

(a) I component.

(b) Q component.

Figure 2.10: Received I and Q components of the OFDM-UWB signal at the LPF's output.

Figure 2.10 shows that the two components are centred at the zero frequency. It is also possible to see that there are spurious at $-f_{RF}$ and f_{RF}, resulting from the filtering process. The baseband signals are then sampled and digitised using analogue-to-digital (ADC) converters. The guard-time of the OFDM-UWB signals is removed and the signals are converted from series to parallel. Then, a fast Fourier transform (FFT) is applied to the resulting waveform and the equalizer transfer function is estimated from the pilot subcarrier information. The pilots information is used to compensate for the amplitude and phase distortions induced on the signal along the transmission system [28], by providing a polynomial interpolation of the channel between the pilots. The final step is to do the symbol demapping and the received constellation is obtained.

2.2 Back-to-back system results

In order to study the OFDM-UWB system performance, firstly the back-to-back configuration (with no fiber transmission), shown in Figure 2.11, is analysed.

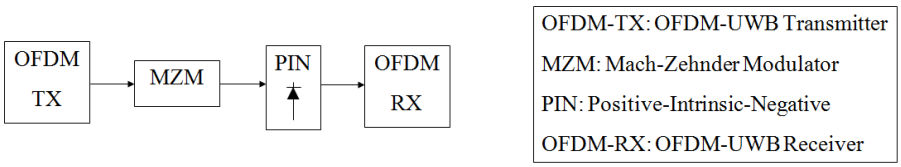

Figure 2.11: Block diagram of the OFDM-UWB system in back-to-back configuration.

The performance analyse of the block diagram represented in Figure 2.11 allows studying how the transmitted signal is affected by the different components of the system, without taking into account the multimode fiber propagation effect. This study allows verifying the reliability of the transmission

system. In the following sections, the results for single- and multi-band transmission are presented. The bit error ratio (BER) of the system is determined by using the semi-analytic gaussian approach presented in [31].

2.2.1 Single-channel transmission

Figure 2.12 and Figure 2.13 show the received constellations without noise at the OFDM-UWB receiver output in back-to-back configuration, for the first four UWB sub-bands.

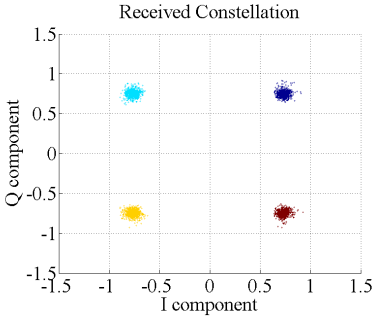

(a) First UWB sub-band.

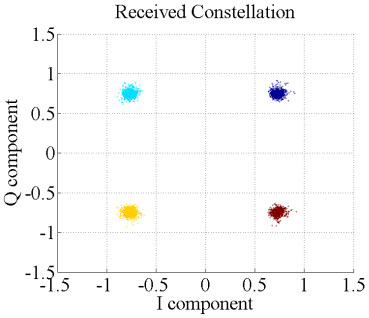

(b) Second UWB sub-band.

Figure 2.12: Received constellations for the first and the second UWB sub-bands.

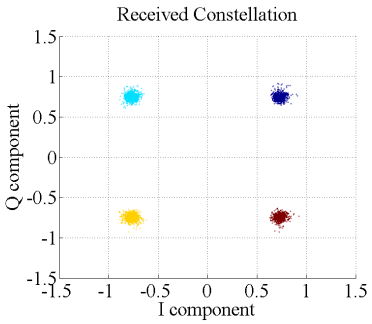

(a) Third UWB sub-band.

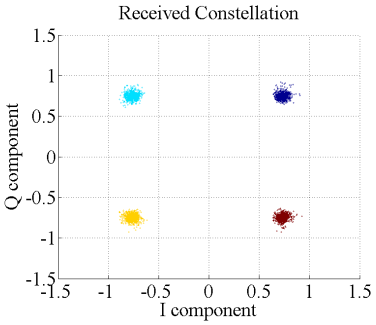

(b) Fourth UWB sub-band.

Figure 2.13: Received constellations for the third and the fourth UWB sub-bands.

The results presented in Figure 2.12 and in Figure 2.13 show that the received constellations for the first four UWB sub-bands are identical. The received constellations are not equal to the sent one since the system components are not ideal. The Bessel filters used in this system introduce some distortion into the signal, originating the non-ideal constellations presented in Figure 2.12 and in Figure 2.13. Nevertheless, the received constellations are very good, which allows a correct demapping of the received signal.

It is also interesting to study the dependence of the bit error ratio of the system on the signal optical power. Figure 2.14 and Figure 2.15 show the bit error ratio as a function of the optical power of the

OFDM-UWB signal, for the first four OFDM-UWB sub-bands.

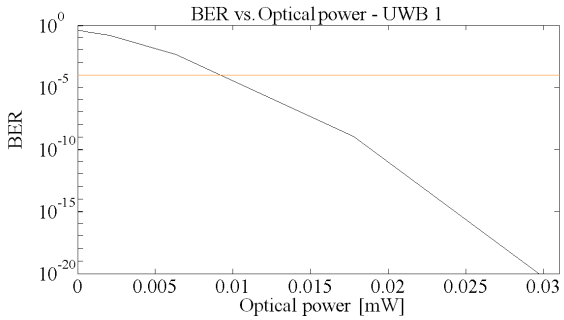

(a) First UWB sub-band.

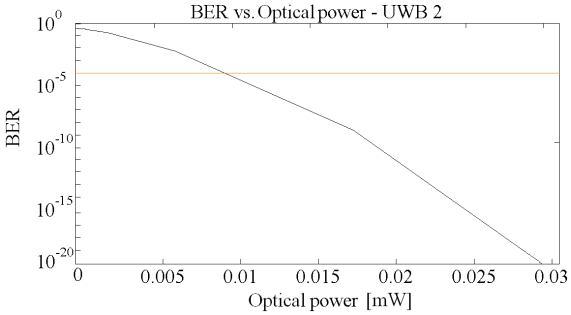

(b) Second UWB sub-band.

Figure 2.14: Bit error ratio as a function of the optical power of the OFDM-UWB signal, for the first and the second UWB sub-bands. The orange line represents a bit error ratio of 10^{-4}.

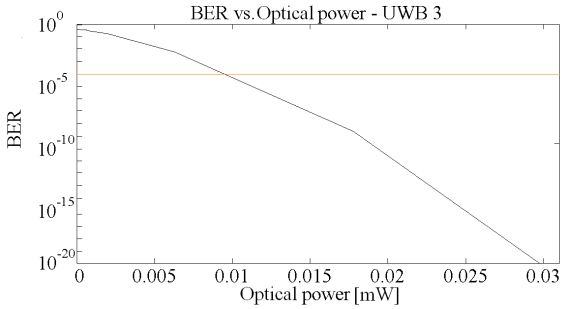

(a) Third UWB sub-band.

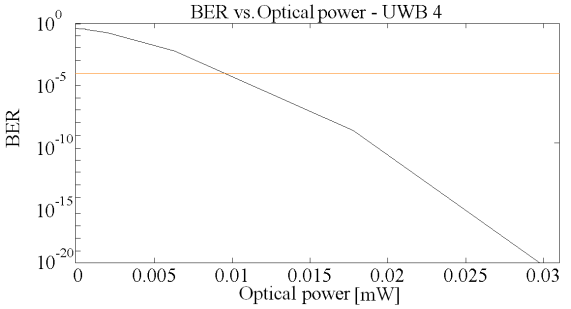

(b) Fourth UWB sub-band.

Figure 2.15: Bit error ratio as a function of the optical power of the OFDM-UWB signal, for the third and the fourth UWB sub-bands. The orange line represents a bit error ratio of 10^{-4}.

Figure 2.14 and Figure 2.15 show that the BER of the system is quite similar for the four sub-bands analysed in this work. It is also possible to see that the system presents a good performance, even for a low optical power of the signal. For example, in order to have a BER of 10^{-4}, it is only needed an optical power of 0.01 mW.

2.2.2 Multi-channel transmission

Figure 2.16, Figure 2.17 and Figure 2.18 show the received constellations without noise at the OFDM-UWB receiver output in back-to-back configuration, when more than one sub-band is used simultaneously. For the multi-band situation, it is assumed that the performance of the system is given by the performance of the worst sub-band.

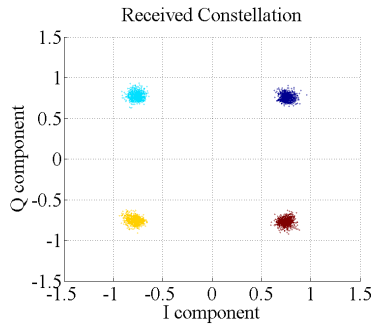

(a) First OFDM-UWB sub-band.

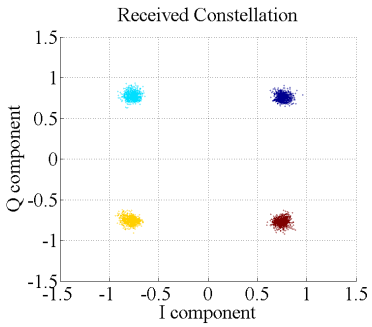

(b) Second OFDM-UWB sub-band.

Figure 2.16: Received constellations for simultaneous transmission of the first two OFDM-UWB sub-bands.

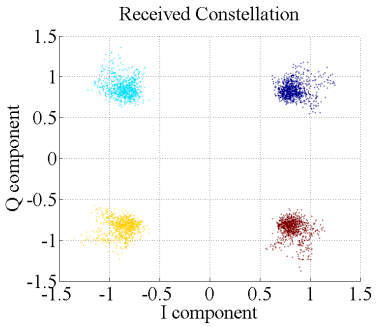

(a) First OFDM-UWB sub-band.

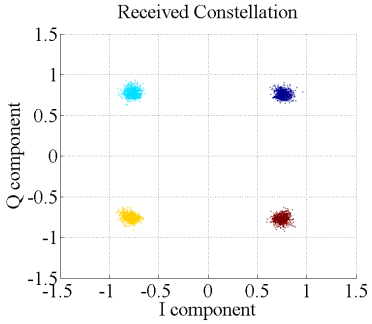

(b) Second OFDM-UWB sub-band.

Figure 2.17: Received constellations of the first and the second OFDM-UWB sub-band for simultaneous transmission of the first three OFDM-UWB sub-bands.

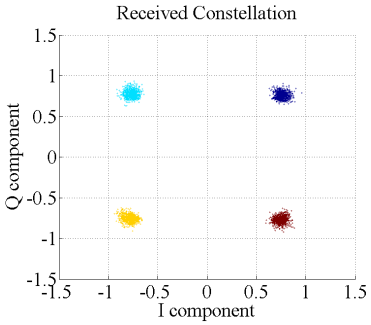

Figure 2.18: Received constellation of the third OFDM-UWB sub-band for simultaneous transmission of the first three OFDM-UWB sub-bands.

The results presented in Figure 2.16, Figure 2.17 and Figure 2.18 show that the multi-band transmission has a significant impact on the received constellations. Figure 2.17 and Figure 2.18 show that the

performance of the system for simultaneous transmission of the first three UWB sub-bands is limited by the performance of the first UWB sub-band, which presents a significant distortion when compared with the other two sub-bands used in this multi-band transmission. So, the use of more than two sub-bands simultaneously leads to the increase of the distortion of the received signal. One justification of this effect is the interference between the UWB sub-bands, since adjacent sub-bands are used. Figure 2.19 presents the bit error ratio of the system as a function of the optical power of the OFDM-UWB signal, for simultaneous transmission of two and three sub-bands.

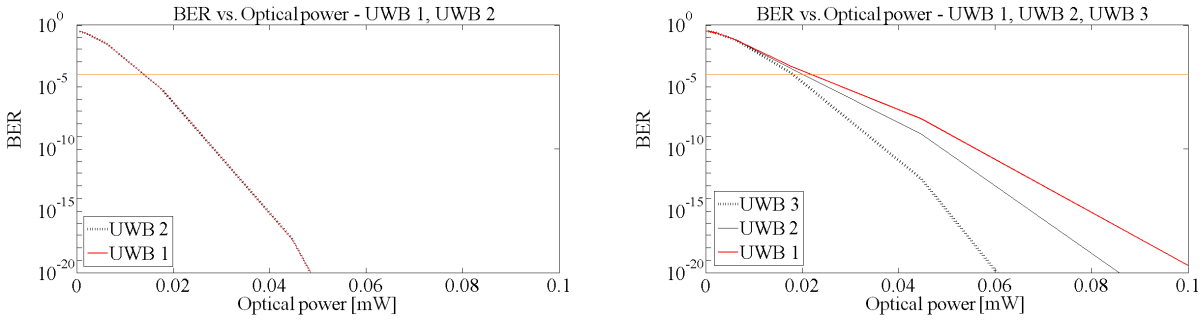

(a) First two UWB sub-bands.

(b) First three UWB sub-bands.

Figure 2.19: Bit error ratio as a function of the optical power of the OFDM-UWB signal, for simultaneous transmission of two and three sub-bands. The orange line represents a bit error ratio of 10^{-4}.

Figure 2.19 shows that the multi-band transmission has impact on the performance of the overall system. It is possible to see that the higher is the number of sub-bands used, the higher is the power needed to achieve the same bit error ratio. For example, in order to have a BER of 10^{-4}, it is needed an optical power of 0.015 mW, for the simultaneous transmission of two sub-bands, and an optical power of 0.025 mW, for the simultaneous transmission of three sub-bands.

2.3 Conclusions

In this chapter, the main components of the OFDM-UWB system are presented and the performance of the system in back-to-back configuration is analysed. The results presented in this chapter confirm that the OFDM-UWB system used in this work presents a good performance (low distortion and a bit error ratio inferior to 10^{-4}) for single-band transmission (for an optical power equal or superior to 0.01 mW) and for multi-band transmission (for an optical power equal or superior to 0.015 mW). The performance of the system for simultaneous transmission of three UWB sub-bands is limited by the distortion of the signal on the first OFDM-UWB sub-band, which presents a received constellation significantly worse than for the other two UWB sub-bands used. The performance degradation of the system for this situation is due to the interference between the UWB sub-bands.

Chapter 3

Propagation model of the step-index multimode fiber

In this chapter, the mathematical theory of the propagation model of the step-index multimode fiber is presented and discussed. In section 3.1, the modal field theory is presented and analysed. The number of modes supported by the multimode fiber are presented in section 3.2. In section 3.3, the modal field amplitudes and the modal powers are presented and studied. The multimode fiber transfer function and its analysis are shown in section 3.4 and the conclusions are presented in Section 3.5.

3.1 Modal field theory

As it was mentioned in Chapter 1, due to its high core-size, multimode fibers can support more than one propagation mode. This happens because the light inside the multimode fiber travels through several different paths, which means that some rays will travel faster than others, as it is possible to see in Figure 3.1, [25]. The rays that travel through shorter paths, which are the ones that will arrive first at the fiber output, are called low order modes and the ones that travel through longer paths are denominated as high order modes. This effect is known by intermodal or modal dispersion [30].

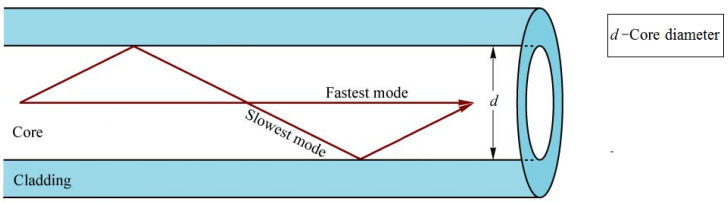

Figure 3.1: Representation of the geometry used for the calculation of the modal dispersion in the multimode fiber (Source: Light Emitting-Diodes, E. Schubert).

Another effect that has a significant impact on the multimode fiber propagation is the chromatic dispersion. This type of dispersion happens due to the different wavelengths that travel in the fiber have different propagation velocities [30]. An illustrative example of the effect of the chromatic dispersion in the multimode fiber propagation is shown in Figure 3.2. In this work, only the impact of the modal dispersion is considered and studied. The chromatic dispersion effect is not taken into account due to the extension of the developed work.

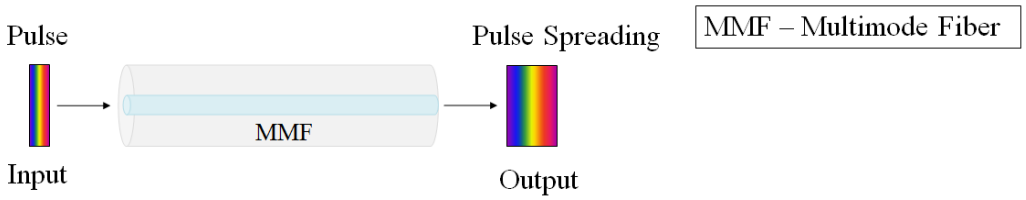

Figure 3.2: Representation of the chromatic dispersion effect in multimode fiber propagation.

3.1.1 Field solutions in the core and cladding regions

Like all electromagnetic phenomena, the propagation of optical fields in multimode fiber is ruled by the Maxwell equations. The cylindrical symmetry of the optical fibers suggests the adoption of a cylindrical polar coordinate system to represent the spatial dependence of each Cartesian field component, as it can be seen in Figure 3.3. However, the mathematical description of the differential operators present in the Maxwell equations becomes simpler if Cartesian field components are used.

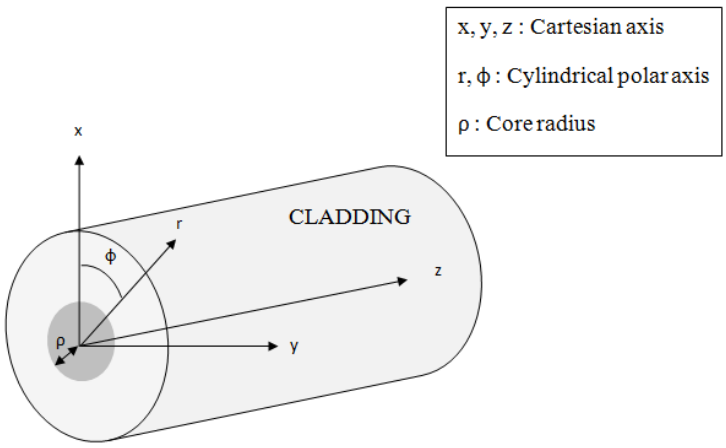

Figure 3.3: Representation of the two coordinates systems used to represent the electric and magnetic fields in the multimode fiber.

Expressing the spatial dependence of each Cartesian field component in the cylindrical polar coordinate system (r, ϕ, z) makes possible to determined each modal field as a function of the radial and

azimuthal coordinates. Due to this fact, each propagated mode can be described by its radial and azimuthal mode number. In this dissertation, the m character is used to identify the radial dependence and the l character is used to identify the azimuthal dependence of each propagated mode.

The existing electromagnetic fields of the multimode fiber are expressed by 3.1 [32]:

$$\begin{cases} \mathbf{E}(x,y,z) = \sum\limits_{l,m} a_{lm}\mathbf{E}_{lm}(x,y,z) + \mathbf{E}_{rad}(x,y,z) \\ \\ \mathbf{H}(x,y,z) = \sum\limits_{l,m} a_{lm}\mathbf{H}_{lm}(x,y,z) + \mathbf{H}_{rad}(x,y,z) \end{cases} \tag{3.1}$$

where lm represents the index of each propagated mode, a_{lm} represents the modal amplitude of the lm propagated mode, $\mathbf{E}_{lm}$ and $\mathbf{H}_{lm}$ represent the electric and magnetic field of the lm propagated mode, respectively, and $\mathbf{E}_{rad}$ and $\mathbf{H}_{rad}$, represent the electric and magnetic radiated modes, respectively. The electric and the magnetic field vectors $\mathbf{E}(x,y,z)$ and $\mathbf{H}(x,y,z)$ presented in Equation 3.1 can be separated in two components: one representing the power that is guided along the fiber and the other one representing the power that is radiated from it. Since the optical fiber is a dielectric waveguide, the number of guided modes supported by it is finite, in opposition to the radiated ones, which are infinite. In this work, only the guided modes are considered, since theses are the modes that carry the biggest amount of power [33].

The longitudinal dependence of each field component is represented by the complex phasor term $e^{j(wt-\beta z)}$, characteristic of the time-harmonic field [32]:

$$\begin{cases} \mathbf{E}_{lm}(x,y,z) = \mathbf{e}_{lm}(x,y)e^{j(wt-\beta_{lm}z)} \\ \\ \mathbf{H}_{lm}(x,y,z) = \mathbf{h}_{lm}(x,y)e^{j(wt-\beta_{lm}z)} \end{cases} \tag{3.2}$$

where β_{lm} represents the propagation constant or eigenvalue of each mode, and $\mathbf{e}_{lm}$ and $\mathbf{h}_{lm}$ represent the envelope of the electrical and magnetic field, respectively.

According to Snyder and Love [32], the wave equation for the step-index fiber presented in Equation 3.3 [34]:

$$\{\nabla_t{}^2 + n^2k^2 - \beta_{lm}{}^2\}\Psi_{lm}(r,\phi) = 0 \tag{3.3}$$

where $\Psi_{lm}(r,\phi)$ corresponds to solutions of the scalar wave equation of the electric or magnetic field of each mode. The quantity $\kappa^2 \equiv n^2k^2 - \beta^2{}_{lm}$ is called transverse phase constant. In order to have a consistent physical solution, $\kappa^2 > 0$ is chosen in the core region, while $\kappa^2 < 0$ is chosen for the cladding

region. The refractive-index in the core region is represented by n_{co} and the refractive-index in the cladding region is represented by n_{clad}. Since $n_{clad} < n_{co}$ for all modes, it is possible to determine the following fundamental property of the propagation constant for every guided modes:

$$kn_{clad} < \beta_{lm} < kn_{co} \tag{3.4}$$

By solving the transversal Laplacian presented in cylindrical coordinates, it is possible to achieve the following second order partial differential equations, for the two fiber regions [32]:

$$\begin{aligned} &\left\{\frac{d^2}{dR^2} + \frac{1}{R}\frac{d}{dR} + \frac{1}{R^2}\frac{d^2}{d\phi^2} + U_{lm}^2\right\}\Psi_{lm}(R\rho,\phi) = 0\ , \quad 0 \leq R \leq 1 \\ &\left\{\frac{d^2}{dR^2} + \frac{1}{R}\frac{d}{dR} + \frac{1}{R^2}\frac{d^2}{d\phi^2} - W_{lm}^2\right\}\Psi_{lm}(R\rho,\phi) = 0\ , \quad 1 \leq R \leq \infty \end{aligned} \tag{3.5}$$

where $R = r/\rho$ is the normalized radius, U_{lm} and W_{lm} are the normalized transversal frequencies in the core and cladding region of each propagated mode, respectively:

$$\begin{cases} U_{lm} = \rho\sqrt{k^2 n_{co}^2 - \beta^2{}_{lm}} \\ W_{lm} = \rho\sqrt{\beta^2{}_{lm} - k^2 n^2{}_{clad}} \end{cases} \tag{3.6}$$

where ρ is the fiber core radius.

It is important to know that the sum of the squared values of the normalized transversal frequency in the core and in the cladding region is a constant for the modal solution of the optical fiber. This quantity is called normalized frequency or parameter V and is given by:

$$V \equiv \sqrt{U_{lm}^2 + W_{lm}^2} = \frac{2\pi\rho}{\lambda}\sqrt{n_{co}^2 - n_{clad}^2} \tag{3.7}$$

The normalized frequency V gives also information about the type of fiber used: for values of V between 0 and 2.405, the fiber propagates a single mode and for values superiors to 2.405 the fiber shows multimode operation [32]. Another important dimensionless quantity is the profile height parameter, which describes the relative difference between the core and the cladding refractive index:

$$\Delta = \frac{n_{co} - n_{clad}}{n_{co}} \tag{3.8}$$

After established the modal parameters, it is possible to solve the differential wave equation. Analysing Equation 3.5, it is possible to see that the differential wave equation coincides with the well-known Bessel differential equation presented in Equation A.3 in Appendix A.

In fact, separable solutions of the wave equation, which are bounded everywhere, vary as $J_l(UR)\cos(l\phi)$ or $J_l(UR)\sin(l\phi)$ in the core region and as $K_l(WR)\cos(l\phi)$ or $K_l(WR)\sin(l\phi)$ in the cladding region, for $l \geq 0$ [32]. $J_l(UR)$ represents the Bessel function of the first kind and $K_l(WR)$ represents the modified

Bessel function of the second kind. The Bessel function of first kind and the modified Bessel function of the second kind are shown in Figure 3.4, [34].

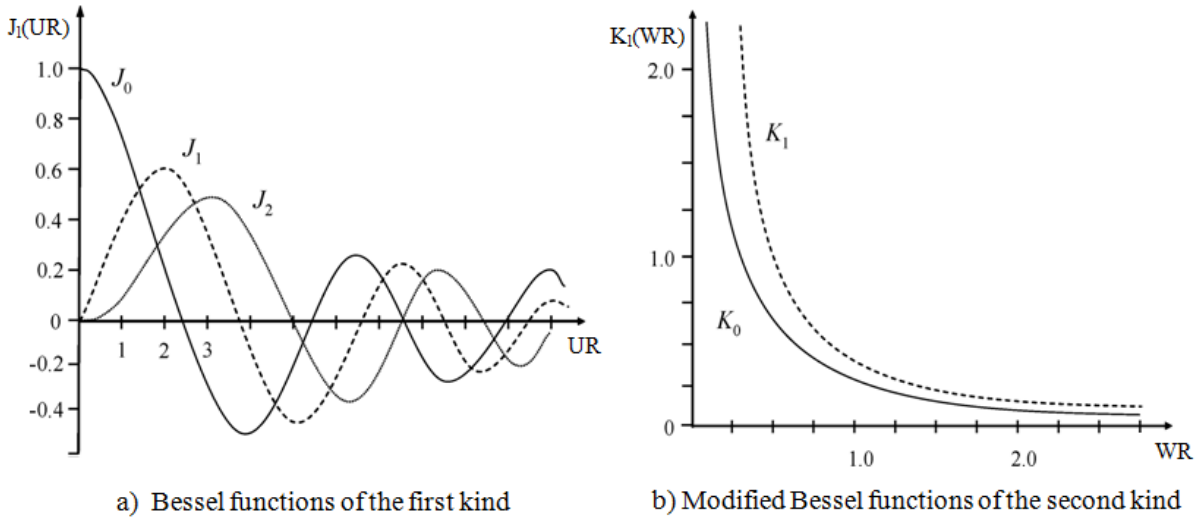

Figure 3.4: Representation of the Bessel function of the first kind for $l = 0, 1, 2$ and of the modified Bessel function of the second kind for $l = 0, 1$. (Source: Multi-gigabit Transmission Over Multimode Optical Fiber: Theory and Design Methods for 10 GbE Systems, S. Bottacchi)

The electromagnetic modes in all waveguide structures are classified according to their electric and magnetic field components. Multimode fibers can support electromagnetic field solutions that can be classified into the three following modes [34]:

- Transversal electric (TE) modes;
- Transversal magnetic (TM) modes;
- Degenerated hybrid modes.

The TE modes have no longitudinal component of the electric field and, consequently, lie on the transversal plane to the waveguide axis, while the magnetic field has longitudinal and transversal components. The (designated) TM modes have no longitudinal component of the magnetic field and, consequently, lie on the transversal plane to the waveguide axis, while the electric field has both components. Due to the weakly guiding properties of optical fibers designed for telecommunications purposes, there is mode degeneracy. The degenerated EH and HE modes are called hybrid modes and they both have the longitudinal component of the electric and magnetic field, simultaneously [34].

According to Snyder and Love [32], the transversal normalized modal fields of the weakly guiding circular fibers are the ones presented in Table 3.1:

Table 3.1: Transversal modal fields of the weakly guiding step-profile multimode fiber.

Modal Field expressions		
Mode	$\mathbf{e}_{ti}$	$\mathbf{h}_{ti}$
$TE_{0,m}$	$\{\mathbf{x}\sin(\phi)-\mathbf{y}\cos(\phi)\}F_1$	$n_{co}\sqrt{\frac{\varepsilon_0}{\mu_0}}\{\mathbf{x}\cos(\phi)+\mathbf{y}\sin(\phi)\}F_1$
$TM_{0,m}$	$\{\mathbf{x}\cos(\phi)+\mathbf{y}\sin(\phi)\}F_1$	$-n_{co}\sqrt{\frac{\varepsilon_0}{\mu_0}}\{\mathbf{x}\sin(\phi)-\mathbf{y}\cos(\phi)\}F_1$
$HE_{l+1,m}$	$\{\mathbf{x}\cos(l\phi)-\mathbf{y}\sin(l\phi)\}F_l$	$n_{co}\sqrt{\frac{\varepsilon_0}{\mu_0}}\{\mathbf{x}\sin(l\phi)+\mathbf{y}\cos(l\phi)\}F_l$
$EH_{l-1,m}$	$\{\mathbf{x}\cos(l\phi)+\mathbf{y}\sin(l\phi)\}F_l$	$-n_{co}\sqrt{\frac{\varepsilon_0}{\mu_0}}\{\mathbf{x}\sin(l\phi)-\mathbf{y}\cos(l\phi)\}F_l$
$F_l = A\frac{J_l(UR)}{J_l(U)}, \quad 0 \le R \le 1$ $F_l = C\frac{K_l(WR)}{K_l(W)}, \quad 1 \le R < \infty$ for $l = 0,1,2,...$		

The characters A and C represent the integration constant pairs resulting from the solutions of the wave (or eigenvalue) equation [34]. These constants can be determined by specifying the boundary conditions at the fiber core-cladding interface.

3.1.2 Boundary conditions

Across the core-cladding interface of the step-index fiber, the boundary conditions of the electromagnetic fields require the continuity of the both electric and magnetic fields [34]:

$$\begin{aligned} \mathbf{E}_{co,t} &= \mathbf{E}_{clad,t} \\ n_{co}^2\mathbf{E}_{co,n} &= n_{clad}^2\mathbf{E}_{clad,n} \\ \mathbf{H}_{co,t} &= \mathbf{H}_{clad,t} \\ \mathbf{H}_{co,n} &= \mathbf{H}_{clad,n} \end{aligned} \tag{3.9}$$

where $\mathbf{E}_{co,t}$ and $\mathbf{E}_{clad,t}$ represent the transversal component of the electric field in the core and in the cladding region, respectively, $\mathbf{E}_{co,n}$ and $\mathbf{E}_{clad,n}$ represent the normal component of the electric field in the core and cladding region, respectively, $\mathbf{H}_{co,t}$ and $\mathbf{H}_{clad,t}$ represent the transversal component of the magnetic field in the core and in the cladding region, respectively, $\mathbf{H}_{co,n}$ and $\mathbf{H}_{clad,n}$ represent the normal component of the magnetic field in the core and cladding region, respectively.

In summary, every component of the electromagnetic fields must be continuous across the core-cladding interface. So, all the existing electric and magnetic fields must be equal at the radial coordinate

$r = \rho$ or, equivalently, $R = 1$, which allows to determinate the unknown coefficients A and C. By applying the boundary conditions to the field expressions presented in Table 3.1 at the core-cladding interface $(R = 1)$, it is easy to conclude that:

$$A\frac{J_l(U)}{J_l(U)} = C\frac{K_l(W)}{K_l(W)} \tag{3.10}$$

$$\Leftrightarrow \tag{3.11}$$

$$A = C$$

In this work, the chosen values for the unknown integration coefficients are $A = C = 1$.

3.2 Mode classification

The number of allowed modes in the multimode fiber is given by the number of solutions of the Equation 3.5, for every existing azimuth mode number. Once the azimuth mode number is fixed, due to the smooth oscillatory behavior of the Bessel function of the first kind, a finite number of solutions is determined. It is clear from the mathematical structure of the modal solutions in Equation 3.5, that the azimuth mode number identifies the order of the Bessel functions in the core and cladding regions. So, all the modes characterized by the same azimuth mode number have the same Bessel order function. The radial mode number m acts like a scaling factor of the radial dependence [34].

By substituting Equation 3.6 in Equation3.5, it is possible to see that the only unknown variable in the eigenvalue equation is the propagation constant β_{lm}, since the fiber core radius ρ, the refractive indexes n_{co} and n_{clad} and the operating wavelength λ are fixed and characteristics of the type of fiber used. The physical multimode fiber parameters used in this dissertation are shown in Table 3.2.

Table 3.2: Parameters used for simulate a step-profile multimode fiber.

Fiber parameters	
Multimode fiber core radius [μm]	$\rho = 25$
Multimode fiber cladding radius [μm]	$\rho_c lad = 125$
Wavelength [nm]	$\lambda = 1550$
Core refractive index	$n_{co} = 1.48$
Cladding refractive index	$n_{clad} = 1.465$
Attenuation coefficient [dB/km]	$\alpha = 1.5$ [35]

The attenuation coefficient value used is the one presented in standard TIA-568 C.3 for $\lambda = 1300$ nm. It was not found any information about the attenuation coefficient for $\lambda = 1550$ nm, so it is assumed

that it is the same as for $\lambda = 1300$ nm. This is a large value of the attenuation coefficient, once this value was dimensioned for in-building installation, so it has to take into account the bends of the fiber along the building and, eventually, the use of fiber slices, which contributes to increase the overall fiber attenuation. Since this work is about in-building networks, it makes sense to use this value of attenuation coefficient.

For every value of the azimuth mode number, the solutions of the eigenvalue equation are ordered according to the radial mode number m, which can vary from one to the maximum number of eigensolutions, for a given azimuth number. For each allowed mode, the solution of the eigenvalue equation relies on the corresponding pair of the normalized frequencies in the core and cladding region.

It is important to note that the eigenvalue equation exhibits wavelength cut-off properties for all guided modes except for the fundamental mode HE_{11}, which has no wavelength cut-off and can always be sustained by the fiber. This means that, when the multimode fiber reaches its cut-off value, it will behave like a single mode fiber, carrying only one propagated mode [32].

Another important statement is that the same value of the propagation constant can be common to different mode structures. This happens because for some different pairs of mode numbers, the eigenvalue equation has the same solution or, equivalently, the same propagation constant. This characteristic leads to mode degeneracy. The mode structures with the same propagation constants can be grouped and form the denominated *linearly polarized* (LP) mode groups [32]. In this work, the four types of allowed modes, namely HE, TE, TM and EH modes are considered separately.

3.2.1 $TE_{0,m}$ and $TM_{0,m}$ modes

The $TE_{0,m}$ and $TM_{0,m}$ modes are obtained by setting $l = 1$ in Equation 3.5. Since both $TE_{0,m}$ and $TM_{0,m}$ modes satisfies the same eigenvalue equation, they must necessarily have the same propagation constant for every fixed radial mode number m [34].

Substituting $l = 1$ on Equation 3.5 and using the recurrence relationships presented in the Appendix A, allows to determine the propagation constant of each $TE_{0,m}$ and $TM_{0,m}$ mode by solving numerically the following system [34]:

$$\begin{cases} U_{0,m}\frac{J_0(U_{0,m})}{J_1(U_{0,m})} + W_{0,m}\frac{K_0(W_{0,m})}{K_1(W_{0,m})} = 0 \\ U_{0,m} = \rho\sqrt{k^2 n_{co}^2 - \beta_{0,m}^2} \\ W_{0,m} = \rho\sqrt{\beta_{0,m}^2 - k^2 n_{clad}^2} \end{cases} \tag{3.12}$$

This system needs to be solved numerically. The only physical parameters envolved are the fiber core

radius ρ, the refractive indexes n_{co} and n_{clad} and the operating wavelength λ. In general, several solutions are available and they can be ordered according to the increasing value of the propagation constant or, equivalenty, to the decreasing value of $U_{0,m}$ [34], using the radial mode number m: $\beta_{0,1} > \beta_{0,2} > ..... > \beta_{0,M}$. The value M gives the number of eigensolutions available for the fixed azimuth number used (in this case, $l = 1$) and for the selected fiber parameters.

The numerical solutions of the eigenvalue equation of the $TE_{0,m}$ and $TM_{0,m}$ modes, for the given set of the fiber parameters presented in Table 3.2, are shown in Table 3.3. Figure 3.5 shows the graphical solutions of equation 3.12 plotted as function of the propagation constant. The total number of $TE_{0,m}$ and $TM_{0,m}$ modes is given by the number of intersections presented in the graphic of Figure 3.5.

Table 3.3: Computed eigenvalue for TE_{0m} and TM_{0m} modes.

$TE_{0,m}$, $TM_{0,m}$ modes			
m	U_{0m}	W_{0m}	β_{0m} [$10^6 \mathrm{m}^{-1}$]
1	21.2671	1.1814	5.9388
2	18.5760	10.4220	5.9532
3	15.6611	14.4365	5.9666
4	12.6984	17.1007	5.9779
5	9.7103	18.9577	5.9868
6	6.0725	20.2178	5.9934
7	3.6627	20.9826	5.9976

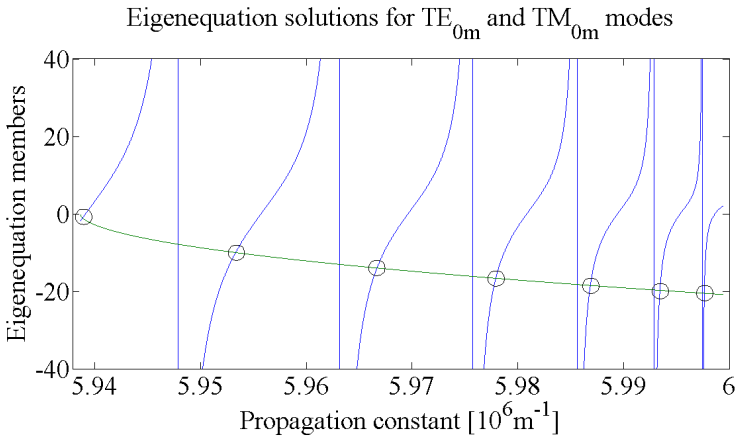

Figure 3.5: Graphical solutions of the eigenvalue equation for TE_{0m} and TM_{0m} modes. The blue and the green line represents the two parcels of the eigenequation presented in Equation 3.12, respectively. The intersection of the eigenequation members gives the total number of TE_{0m} and TM_{0m} modes.

3.2.2 $HE_{l+1,m}$ modes

The $HE_{l+1,m}$ modes are obtained by setting $l \geq 0$ in the Equation 3.5. By using the recurrence relationships presented in the Appendix A in the Equation 3.5, the propagation constant of each $HE_{l+1,m}$ modes is determined by solving numerically the following system [34]:

$$\begin{cases} U_{l+1,m}\frac{J_{l+1}(U_{l+1,m})}{J_l(U_{l+1,m})} - W_{l+1,m}\frac{K_{l+1}(W_{l+1,m})}{K_l(W_{l+1,m})} = 0 \\ \\ U_{l+1,m} = \rho\sqrt{k^2 n_{co}^2 - \beta_{l+1,m}^2} \\ \\ W_{l+1,m} = \rho\sqrt{\beta_{l+1,m}^2 - k^2 n_{clad}^2} \end{cases} \tag{3.13}$$

In this case, the eigenvalue equation depends on the azimuth mode number. So, for each fixed azimuth number, the Equation 3.13 will present several solutions. In Table 3.4, the numerical solutions of the eigenvalue equation for the superior $HE_{l+1,m}$ modes are presented for $l = 0, 1, 2, 3, 4$.

Table 3.4: Computed propagation constants for $HE_{l+1,m}$ modes for $l = 0, 1, 2, 3, 4$.

$HE_{l+1,m}$ superior modes					
m	β_{1m} $[10^6 \mathrm{m}^{-1}]$	β_{2m} $[10^6 \mathrm{m}^{-1}]$	$\beta_{3m}[10^6 \mathrm{m}^{-1}]$	$\beta_{4m}[10^6 \mathrm{m}^{-1}]$	β_{5m} $[10^6 \mathrm{m}^{-1}]$
1	5.9459	5.9388	5.9463	5.9394	5.9476
2	5.9601	5.9532	5.9606	5.9542	5.9620
3	5.9725	5.9666	5.9730	5.9672	5.9744
4	5.9826	5.9779	5.9831	5.9789	5.9846
5	5.9903	5.9868	5.9908	5.9879	5.9924
6	5.9957	5.9934	5.9962	5.9945	—
7	5.9987	5.9976	—	—	—

Table 3.4 shows that, for any value of the azimuth mode number l, the number of solutions of the eigenvalue equation is not constant. Instead, it decreases with the increase of the azimuth mode number l.

The graphical solution of the eigenvalue equation for the $HE_{1,m}$ and $HE_{5,m}$ modes are shown in Figure 3.6 and in Figure 3.7, respectively.

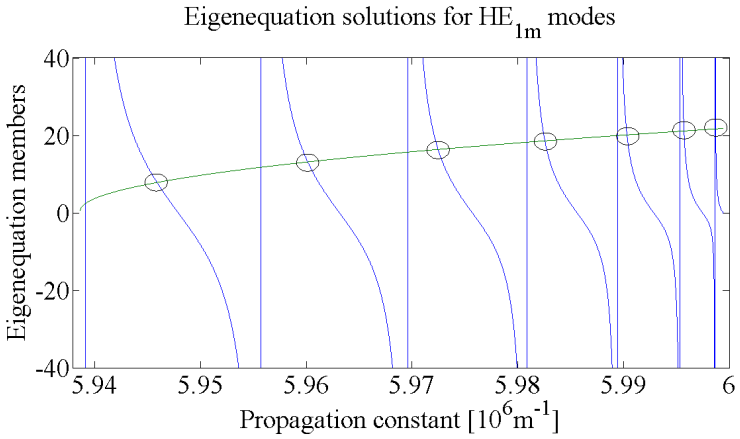

Figure 3.6: Graphical solutions of the eigenvalue equation for HE_{1m} modes. The blue and the green line represents the two parcels of the eigenequation presented in Equation 3.13 for $l = 0$, respectively. The intersection of the eigenequation members gives the total number of $HE_{1,m}$ modes.

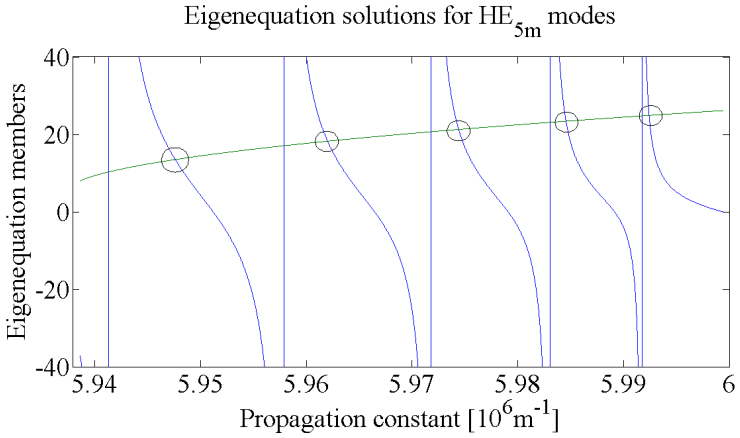

Figure 3.7: Graphical solutions of the eigenvalue equation for HE_{5m} modes. The blue and the green line represents the two parcels of the eigenequation presented in Equation 3.13 for $l = 4$, respectively. The intersection of the eigenequation members gives the total number of $HE_{5,m}$ modes. It is possible to see that for $l = 4$, the number of available solutions is smaller than for $l = 0$.

From Table 3.4 and from Equation 3.13, it is easy to verify that each azimuth mode number leads to different solutions of the eigenvalue equation and, consequently, to different allowed modes in the multimode fiber. The eigenvalue equation has solutions until the azimuth mode number does not exceed the cut-off value. From that point on, there are no more intersections between the eigenequation members, which will lead to no more mode solutions for that mode family [34].

Figure 3.8 shows the situation close to mode cut-off. In particular, for a fiber with the parameters presented in Table 3.2, the mode $HE_{18,1}$ is still supported but the successive mode $HE_{19,1}$ is not, leading

to no more mode solutions of the eigenvalue equation, which means that this mode can't be supported by the fiber used, as it is possible to see in Figure 3.9.

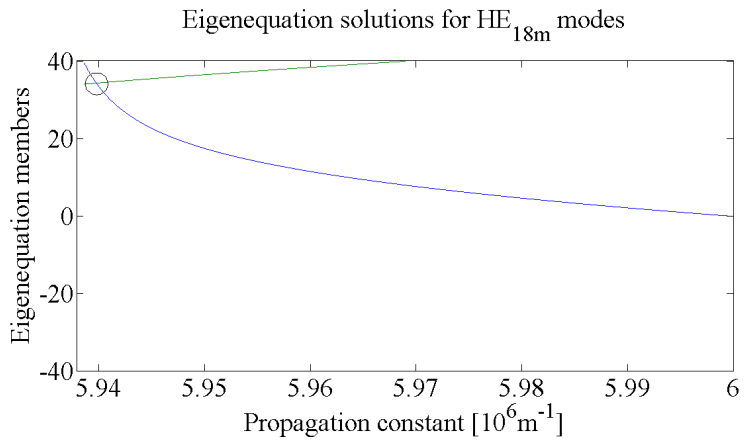

Figure 3.8: Graphical solutions of the eigenvalue equation for HE_{18m} modes.In this situation, there is only one interception between the eigenequation members.

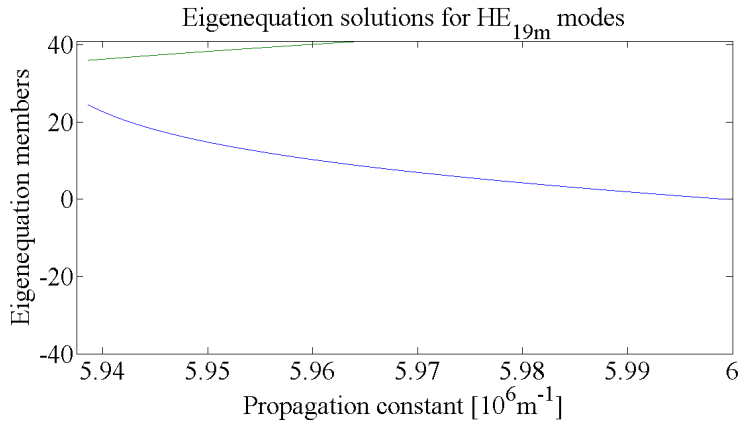

Figure 3.9: Graphical solutions of the eigenvalue equation for HE_{19m} modes. There is no intersection between the eigenequation members, so this mode will never be sustained by the fiber used.

3.2.3 $EH_{l-1,m}$ modes

The $EH_{l-1,m}$ modes are obtained by setting $l > 1$ on the Equation 3.5. By using the recurrence relationships presented in the Appendix A, it is possible to determine the propagation constant of each $EH_{l-1,m}$ modes by solving numerically the following system [34]:

$$\begin{cases} U_{l-1,m}\frac{J_{l-1}(U_{l-1,m})}{J_l(U_{l-1,m})} + W_{l-1,m}\frac{K_{l-1}(W_{l-1,m})}{K_l(W_{l-1,m})} = 0 \\ \\ U_{l-1,m} = \rho\sqrt{k^2 n_{co}^2 - \beta^2{}_{l-1,m}} \\ \\ W_{l-1,m} = \rho\sqrt{\beta^2{}_{l-1,m}{}^2 - k^2 n_{clad}^2} \end{cases} \tag{3.14}$$

Once again, the eigenvalue equation depends on the azimuth mode number, which means that there will be several solutions for every fixed azimuth number. In Table 3.5, the numerical solutions of the eigenvalue equation for the $EH_{l-1,m}$ modes are presented for $l = 2,3,4,5,6$.

Table 3.5: Computed propagation constants for $EH_{l-1,m}$ modes for $l = 2,3,4,5,6$.

$EH_{l-1,m}$ superior modes					
m	β_{1m} $[10^6\mathrm{m}^{-1}]$	$\beta_{2m}[10^6\mathrm{m}^{-1}]$	$\beta_{3m}[10^6\mathrm{m}^{-1}]$	$\beta_{4m}[10^6\mathrm{m}^{-1}]$	$\beta_{5m}[10^6\mathrm{m}^{-1}]$
1	5.9463	5.9394	5.9476	5.9409	5.9499
2	5.9606	5.9542	5.9620	5.9561	5.9645
3	5.9730	5.9676	5.9744	5.9696	5.9779
4	5.9831	5.9789	5.9846	5.9810	5.9874
5	5.9908	5.9879	5.9924	5.9901	—
6	5.9962	5.9945	—	—	—

Comparing the results presented in Table 3.5 with the results shown in Table 3.4, it is possible to see that, for the same given azimuth mode number, the number of allowed $EH_{l-1,m}$ modes is one unit smaller than the corresponding number of allowed $HE_{l+1,m}$ modes. For example, the $HE_{2,m}$ has seven allowed modes, when the $EH_{2,m}$ has only six. Figure 3.10 and Figure 3.11 show the numerical solutions of Equation 3.14 for the $EH_{1,m}$ and $EH_{5,m}$ modes.

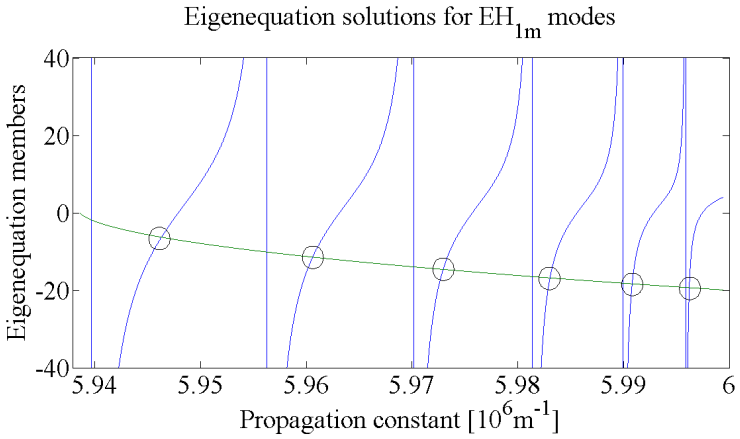

Figure 3.10: Graphical solutions of the eigenvalue equation for EH_{1m} modes.

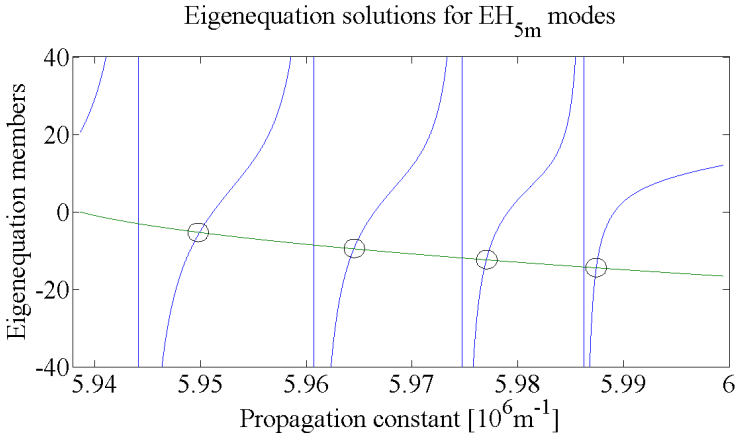

Figure 3.11: Graphical solutions of the eigenvalue equation for EH_{5m} modes.

As for the $HE_{l+1,m}$, the eigenvalue equation only has solutions until the azimuth mode number does not exceed the cut-off value. Figure 3.12 shows the situation close to mode cut-off, for a fiber with the parameters presented in Table 3.2. The successive mode $EH_{17,1}$ is no longer supported by this fiber, leading to no more mode solutions of the eigenvalue equation, as it possible to see in Figure 3.13.

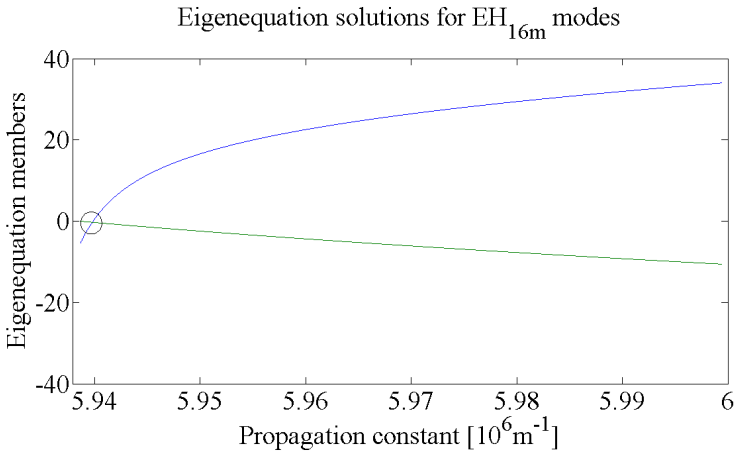

Figure 3.12: Graphical solutions of the eigenvalue equation for EH_{16m} modes.

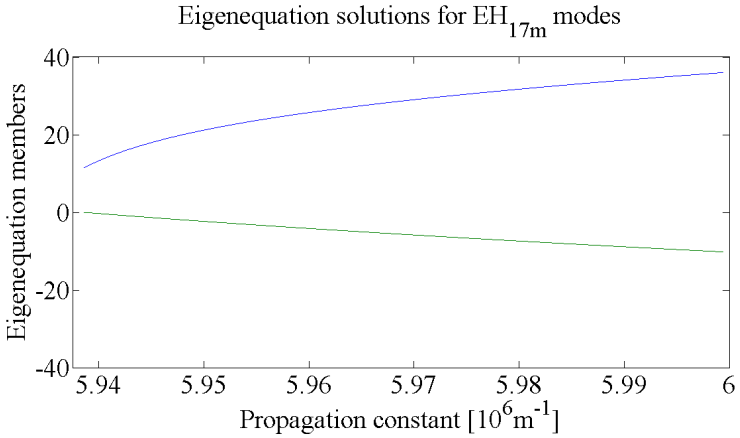

Figure 3.13: Graphical solutions of the eigenvalue equation for EH_{17m} modes. There is no intersection between the eigenequation members, so this mode will never be supported by the fiber used.

The number of allowed modes for $\lambda = 1310$ nm were also determined. These values are presented in Appendix B. It is possible to see that for $\lambda = 1310$ nm, there are more allowed modes then for $\lambda = 1550$ nm, since the smaller is the wavelength, the higher is the number of allowed modes by the multimode fiber. This consequence can be also achieved by the analysis of the V parameter.

3.3 Modal amplitude and modal power

The power generated by the electromagnetic fields of the optical fiber can be obtained from the Poynting vector. The Poynting vector represents the electromagnetic power flux density across the unit surface normal to the power flux direction [34]:

$$S \equiv \frac{1}{2}\mathrm{Re}\{\mathbf{E} \times \mathbf{H}^*\} \tag{3.15}$$

By expressing the electromagnetic fields in the multimode fiber presented in Equation 3.1 in its polar coordinates, and decomposing the general expression of electromagnetic field in its transversal and longitudinal components, we can write:

$$\begin{cases} \mathbf{E}(\rho,\phi) = \sum\limits_{l,m} a_{lm}\{\mathbf{E}_{t,lm}(\rho,\phi) + \mathbf{E}_{z,lm}(\rho,\phi)\mathbf{z}\} \\ \\ \mathbf{H}(\rho,\phi) = \sum\limits_{l,m} a_{lm}\{\mathbf{H}_{t,lm}(\rho,\phi) + \mathbf{H}_{z,lm}(\rho,\phi)\mathbf{z}\} \end{cases} \tag{3.16}$$

where $\mathbf{E}_{t,lm}$ and $\mathbf{H}_{t,lm}$ represent the electric and magnetic field transversal components, respectively, and $\mathbf{E}_{z,lm}$ and $\mathbf{H}_{z,lm}$ represent the electric and magnetic field longitudinal components, respectively.

By substituting Equation 3.16 in Equation 3.15 and assuming that the transversal component of the electromagnetic fields are real, it is possible to compute the corresponding longitudinal component of Poynting vector in the direction of the fiber axis, for a given (l,m) mode:

$$S_{z,lm}(\rho,\phi) = \frac{1}{2}|a_{lm}|^2\{\mathbf{E}_{t,lm}(\rho,\phi) \times \mathbf{H}^*_{t,lm}(\rho,\phi)\} \cdot \mathbf{z} \tag{3.17}$$

The modal power P_{lm} associated to each guided mode is given by the integration of the power flux density across the infinite fiber section A_∞ of that mode:

$$P_{lm} = \int_{A_\infty} S_{z,lm}(\rho,\phi)dA = \frac{1}{2}|a_{lm}|^2 \int_{A_\infty} \{\mathbf{E}_{t,lm}(\rho,\phi) \times \mathbf{H}^*_{t,lm}(\rho,\phi)\} \cdot \mathbf{z}dA \tag{3.18}$$

The total bound power P_{tot} is given by the sum of all allowed modes:

$$P_{tot} = \sum_{l,m} P_{lm} = \frac{1}{2}\sum_{l,m} |a_{lm}|^2 \int_{A_\infty} \{\mathbf{E}_{t,lm}(\rho,\phi) \times \mathbf{H}^*_{t,lm}(\rho,\phi)\} \cdot \mathbf{z}dA \tag{3.19}$$

So, in order to determine the total power carried by the multimode fiber, it is necessary to determine the modal amplitudes a_{lm} of each guided mode. To achieve this purpose, the orthogonal property of the bound mode set needs to be used. This property is derived from the Maxwell reciprocity theorem applied to a non-absorbing waveguide. The demonstration of this theorem is out of the scope of this work. A careful demonstration of this property can be seen in [32].

The modal amplitude of each guided mode under the weakly guiding approximation is given by Equation C.9(the mathematical derivation of the modal amplitude expression is presented in Appendix C):

$$a_{l,m} = \frac{\int_{A_\infty} \{\mathbf{E}_s(\rho,\phi) \times \mathbf{z} \times \mathbf{E}^*_{t,lm}(\rho,\phi)\} \cdot \mathbf{z}dA}{\int_{A_\infty} |\mathbf{E}_{t,lm}(\rho,\phi)|^2 dA} \tag{3.20}$$

Equation C.9 shows that once the source field $E_s(\rho,\phi)$ is known, the modal amplitude depends exclusively on the transversal component of the electric field. The total power carried by each mode, under the weakly guiding approximation, is given by the substitution of Equation C.9 on Equation 3.19:

$$P_{tot} = \frac{n_{co,clad}}{2Z_0} \sum_{l,m} \frac{|\int_{A_\infty} \{\mathbf{E}_s(\rho,\phi) \times \mathbf{z} \times \mathbf{E}^*_{t,lm}(\rho,\phi)\} \cdot \mathbf{z} dA|^2}{\int_{A_\infty} |\mathbf{E}_{t,lm}(\rho,\phi)|^2 dA} \tag{3.21}$$

Equation C.9 shows that once the source field $E_s(\rho,\phi)$ is known, the modal amplitude depends exclusively on the transversal component of the electric field.

3.3.1 Source Field

At this point, it is important to define the optical source used in this work. The most common type of source used to couple the light into a multimode fiber is from a single mode fiber. A representative scheme of the light launching from a SMF to a MMF is shown in Figure 3.14.

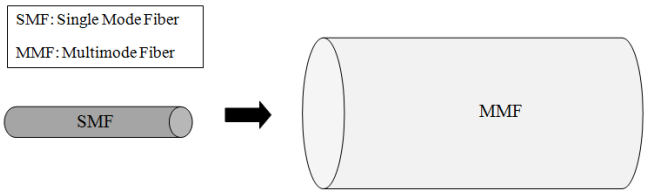

Figure 3.14: Representative scheme of the light launching from the SMF to the MMF. Only the core of both fibers are represented, since the largest amount of power is contained in these regions.

The small SMF core radius, where the most of the optical fiber power is contained, allows launching the light in any point of the MMF region, exciting different types of modes. So, by choosing the point in the MMF where we want to couple the power launched from the SMF, it is possible to study the modal power distribution in the multimode fiber, because different launch conditions will excite different types of modes. In order to do that, it is necessary to establish a relationship between the MMF coordinates and the SMF coordinates. The method developed to achieve this purpose is presented in the Appendix D.

A single mode fiber, in opposition to the multimode fiber, supports only one mode: the fundamental HE_{11} mode [18]. So, the field expression of the single mode fiber is similar the expression of the multimode fiber HE_{11} mode, presented in Table 3.1.

Table 3.6: Electromagnetic field of the single mode fiber.

Fundamental HE_{11} mode	
$\mathbf{e}_{ti}$	$\mathbf{h}_{ti}$
$\mathbf{x}F_0$	$n_{smf,co}\sqrt{\frac{\varepsilon_0}{\mu_0}}\mathbf{y}F_0$
$F_0 = A_{SMF}\frac{J_0(UR)}{J_0(U)}, \quad 0 \leq R \leq 1$ $F_0 = A_{SMF}\frac{K_0(WR)}{K_0(W)}, \quad 1 \leq R < \infty$	

where A_{SMF} represents the field amplitude coefficient and $n_{smf,co}$ represents the refractive index of the core region of the single mode fiber. Assuming the source is linearly polarized along the $\mathbf{x}$ axis, $\mathbf{E}_s(\rho,\phi) = E_s(\rho,\phi)\mathbf{x}$, the modal amplitude expression presented in Equation C.9 can be simplified:

$$a_{l,m} = \frac{\int_{A_\infty} \mathbf{E}_s(\rho,\phi)\mathbf{E}^*_{x,lm}(\rho,\phi)dA}{\int_{A_\infty} |\mathbf{E}_{t,lm}(\rho,\phi)|^2 dA} \tag{3.22}$$

The next step is to determine the amplitude coefficient of the source electric field A_{SMF}. The amplitude coefficient can be obtained by manipulating the expression of the total power carried by the fiber P_{SMF} [33]:

$$P_{SMF} = \frac{1}{2}\int_0^{2\pi}\int_0^{\infty} (E_x {H_y}^* - E_y {H_x}^*) r dr d\phi \tag{3.23}$$

The total power carried by the SMF is obtained by summing the existing power in the core and cladding regions, $P_{SMF} = P_{co} + P_{clad}$. So, it is possible to split Equation 3.23 in two parcels, one representing the power contained in the core region and the other representing the power contained in the cladding region:

$$P_{co} = \frac{1}{2}\int_0^{2\pi}\int_0^{\rho} (E_x {H_y}^* - E_y {H_x}^*) r dr d\phi \tag{3.24}$$

$$P_{clad} = \frac{1}{2}\int_0^{2\pi}\int_{\rho}^{\infty} (E_x {H_y}^* - E_y {H_x}^*) r dr d\phi \tag{3.25}$$

By substituting the SMF field expression presented in Table 3.6 in Equation 3.24 and in Equation 3.25 and using the indefinite Bessel integrals presented in the Appendix A, the following expressions are obtained:

$$P_{co} = \frac{\pi n_{smf,co}}{J_0^2(U)}\sqrt{\frac{\varepsilon_0}{\mu_0}}A_{SMF}^2\int_0^{\rho} J_0^2\left(\frac{Ur}{\rho}\right) r dr d\phi = \frac{\rho^2 \pi n_{smf,co}}{2}\sqrt{\frac{\varepsilon_0}{\mu_0}}A_{SMF}^2\left\{1 + \frac{J_1^2(U)}{J_0^2(U)}\right\} \tag{3.26}$$

$$P_{clad} = \frac{\pi n_{smf,clad}}{K_0^2(W)} \sqrt{\frac{\varepsilon_0}{\mu_0}} A_{SMF}^2 \int_{\rho}^{\infty} K_0^2 \left(\frac{Wr}{\rho} \right) r dr d\phi = \frac{\rho^2 \pi n_{smf,clad}}{2} \sqrt{\frac{\varepsilon_0}{\mu_0}} A_{SMF}^2 \left\{ \frac{K_1^2(W)}{K_0^2(W)} - 1 \right\} \quad (3.27)$$

Summing the power in the core and cladding regions and solving the result in order to A_{SMF}, the amplitude coefficient of the SMF field is obtained:

$$A_{SMF} = \sqrt{\frac{2P_{SMF}}{\rho^2 \pi \sqrt{\frac{\varepsilon_0}{\mu_0}} \left\{ n_{smf,co} \left(1 + \frac{J_1^2(U)}{J_0^2(U)} \right) + n_{smf,clad} \left(\frac{K_1^2(W)}{K_0^2(W)} - 1 \right) \right\}}} \quad (3.28)$$

So, it is obvious from Equation 3.23 that, by imposing the power transmitted by the electric source field, it is possible to determine the amplitude coefficient of the SMF field A_{SMF}.

The physical parameters of the single mode fiber used in this work are presented in Table 3.7.

Table 3.7: Parameters used for simulate a step-profile single mode fiber.

SMF parameters	
Core radius [μm]	$\rho_{smf,co} = 4$
Cladding radius [μm]	$\rho_{smf,clad} = 125$
Wavelength [nm]	$\lambda = 1550$
Core refractive index	$n_{smf,co} = 1.48$
Cladding refractive index	$n_{smf,clad} = 1.477$

A graphical interpretation of the amplitude distribution of the SMF electrical field, for the set of parameters presented in Table 3.7 is shown in Figure 3.15. The values of the vacuum electric permittivity and of the vacuum magnetic permeability are, respectively, $\varepsilon_0 = 8.854 \times 10^{-12}$ F/m and $\mu_0 = 4\pi \times 10^{-7}$ H/m.

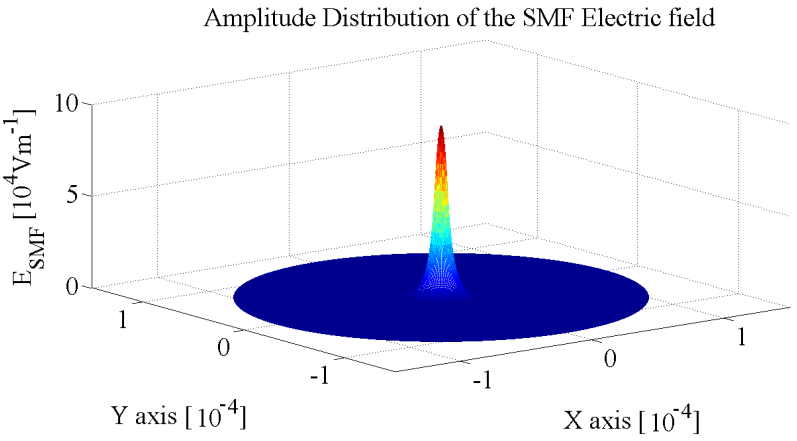

Figure 3.15: Color representation of the amplitude distribution of the SMF electric field for a launch power of 1 mW.

3.4 Multimode fiber transfer function

The multimode fiber transfer function can be represented as linear combination of the individual mode contributions. Each excited mode presents a fraction of the total launched optical power, associated with a given modal delay. The modal delay is defined by the product between the delay per unit length and the fiber length. The delay per unit length of each mode is given by the following expression [34]:

$$\tau_{lm} = \frac{\lambda}{2\pi c}\beta_{lm} \tag{3.29}$$

According to Bottacchi [34], the power transfer function of the multimode fiber is given by:

$$H_{MMF}(f) = \sum_{l,m} p_{lm} e^{-j2\pi f \tau_{lm} L_{MMF}} e^{-\alpha L_{MMF}} \tag{3.30}$$

where p_{lm} represents the fraction of power of each guided mode, f is transmission frequency, τ_{lm} represents the delay per unit length of each mode, L_{MMF} represents the length of fiber used and α represents the attenuation coefficient associated with the multimode fiber operating wavelength.

3.4.1 Results analysis

In order to analyse the power distribution by the different modes supported by the fiber, several launching conditions are considered. The multimode fiber propagation model was studied for the following launching conditions: centred, 5 μm, 20 μm and 25 μm offset launching. Due to the extension of the developed work, only the centred and the 20 μm offset launching are analysed in detail. Figure 3.16

and Figure 3.17 show the multimode amplitude responses for two different launching conditions of the optical source: zero and 20 μm offset, for fiber lengths of 100 m and 500 m, respectively.

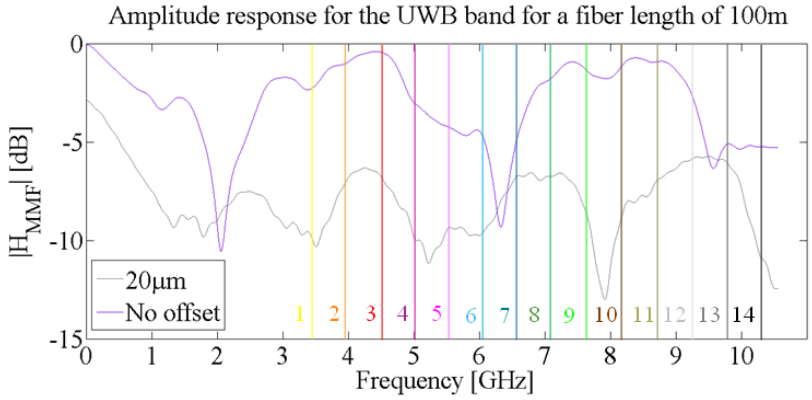

Figure 3.16: Amplitude response for a fiber length of 100m and for centred fiber axes and for a launch offset of 20 μm. The vertical colored lines represents the RF carrier frequency of each of the 14 UWB sub-bands.

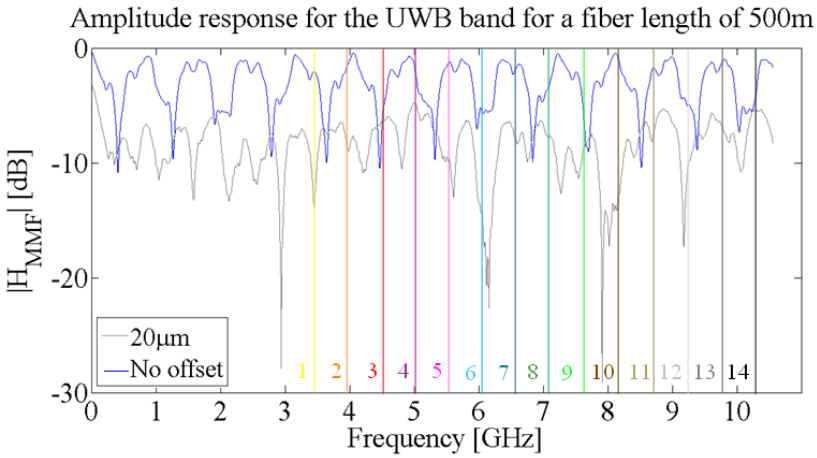

Figure 3.17: Amplitude response for a fiber length of 500m and for centred fiber axes and for a launch offset of 20 μm. The vertical colored lines represents the RF carrier frequency of each of the 14 UWB sub-bands.

The first important conclusion to take from the analysis of the amplitude frequency responses is that, for non-centred launching conditions of the source optical power, there is power coupling losses. These losses are due to the misalignment between the SMF and the MMF core axes. The power coupling losses can be determined by the following expression [30]:

$$L_c = 10\log\left(\frac{P_{SMF}}{P_{MMF}}\right) \tag{3.31}$$

So, for an offset launching of 20 μm, there are coupling losses of 2.8dB. From Figure 3.16 and Figure 3.17, it is possible to concluded that the multimode fiber frequency response is quite different from one subband to another. The RF carriers, which are located in a smoother region of the multimode fiber frequency response, will transmit information with better quality than the ones located in peak regions. This result will be confirmed and analysed in detail in Chapter 4. Another important and expected result is that, the amplitude response of the multimode mode fiber has significantly smoother behavior for a fiber length of 100 m than for a fiber of 500 m. This happens because the length of the fiber has a direct impact on the modal delay which, consequently, affects the multimode fiber amplitude response, as it possible to see in Equation 3.30. The higher is the length of the fiber, the higher is the modal delay. This effect creates more distortion in the transfer function and leads to a significant degradation of the amplitude and delay responses, as it possible to see by comparing the results presented in Figure 3.18 and in Figure 3.19.

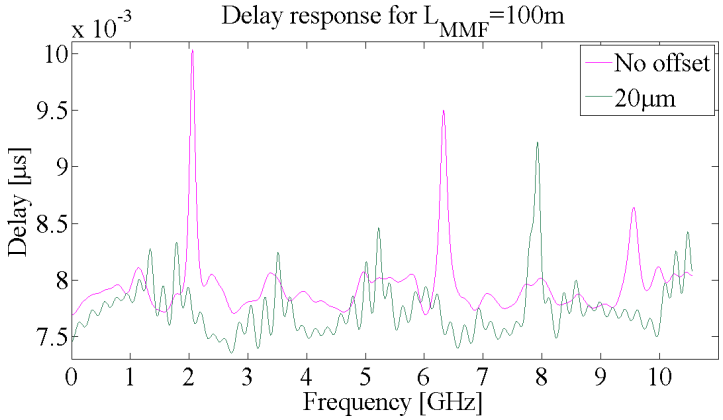

Figure 3.18: Delay response for a fiber length of 100 m and for centred fiber axes and for a launch offset of 20 μm.

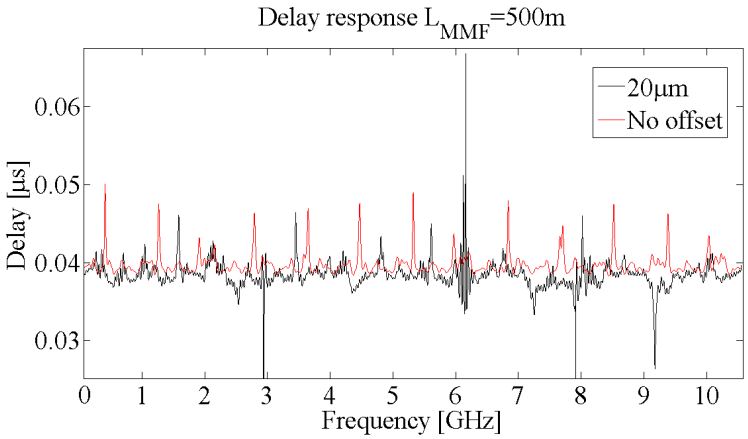

Figure 3.19: Delay response for a fiber length of 500 m and for centred fiber axes and for a launch offset of 20 μm.

It is important to understand the dependence of the power coupling losses on the launching offset. Table 3.8 shows the power coupling losses for all the launching conditions analysed in this work.

Table 3.8: Power coupling losses for different launching conditions.

Offset [μm]	P_{coup}[dB]
0	0
5	1.7
20	2.8
25	4.5

Table 3.8 shows that the increase of the offset of launching conditions increases the power coupling losses. This happens due to the increase of the distance between the SMF and the MMF centres, which increases the fibers misalignment. The offset increasing also leads to the cladding region proximity, where is more difficult to couple power without losses [26].

Another important feature of the multimode fiber propagation model is the modal power distribution. This distribution is strongly dependent on the launching conditions. Figure 3.20 presents the power fraction distribution for the existing fiber modes plotted as a function of its modal delay, for centred launching conditions. Figure 3.21, Figure 3.22, Figure 3.23 and Figure 3.24 show the power fraction distribution for the existing fiber modes plotted as function of its modal delay, for a 20 μm launch offset. The modal power distribution for $\lambda = 1310$ nm is presented in the Appendix B.

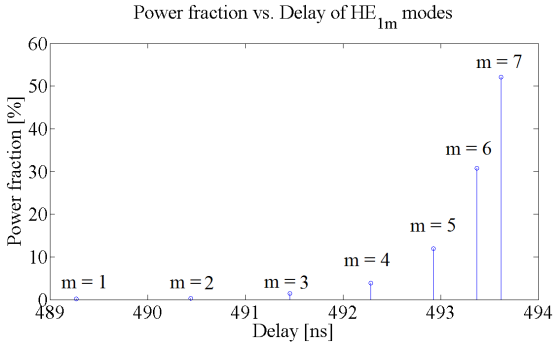

Figure 3.20: Power fraction of the HE_{1m} modes for a fiber length of 100 m and centred launching conditions. In this situation, only the lower order HE_{1m} modes are excited.

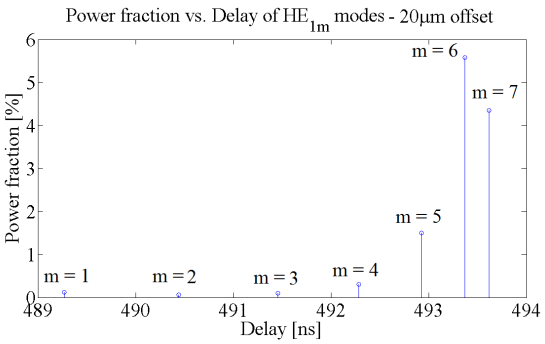

(a) HE_{1m} modes.

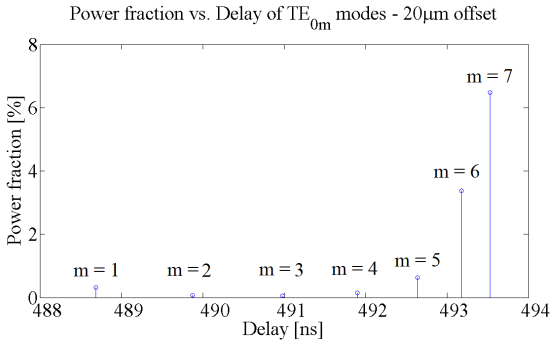

(b) TE_{0m} modes.

Figure 3.21: Power fraction of the HE_{1m} and TE_{0m} modes for a fiber length of 100 m and a launch offset of 20 μm.

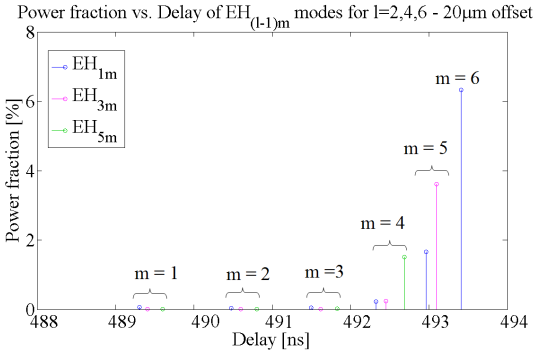

(a) EH_{1m}, EH_{3m} and EH_{5m} modes.

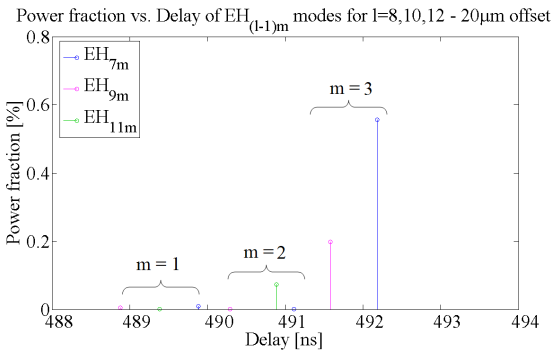

(b) EH_{7m}, EH_{9m} and EH_{11m} modes.

Figure 3.22: Power fraction of the $EH_{(l-1),m}$ modes for $l = 2,4,6,8,10,12$, for a fiber length of 100 m and a launch offset of 20 μm.

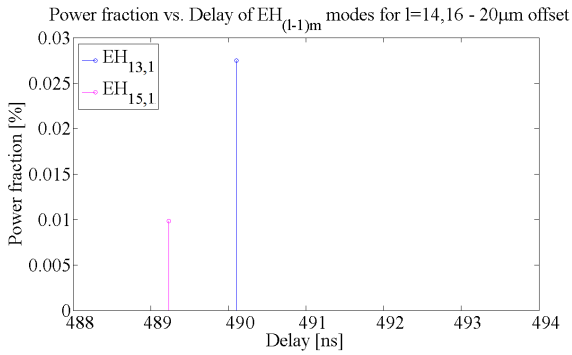

(a) EH_{13m} and EH_{15m} modes.

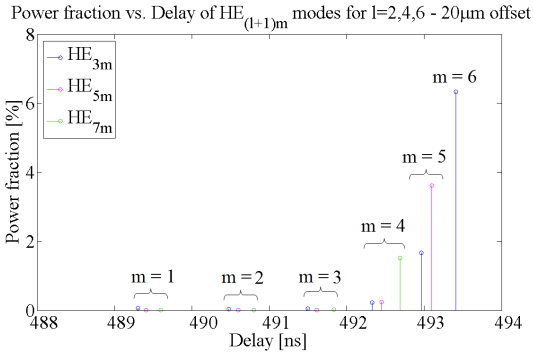

(b) HE_{3m}, HE_{5m} and HE_{7m} modes.

Figure 3.23: Power fraction of the $EH_{(l-1),m}$ modes for $l = 14,16$ and $HE_{(l+1),m}$ modes for $l = 2,4,6$, for a fiber length of 100 m and a launch offset of 20 μm.

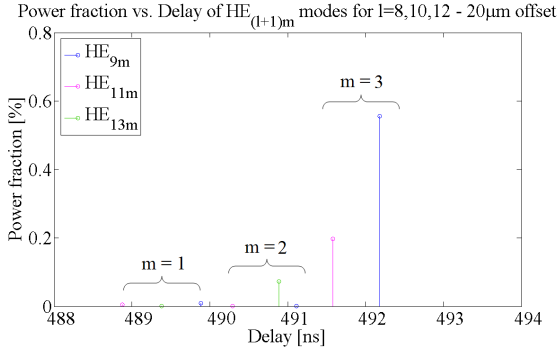

(a) HE_{9m}, HE_{11m} and HE_{13m} modes.

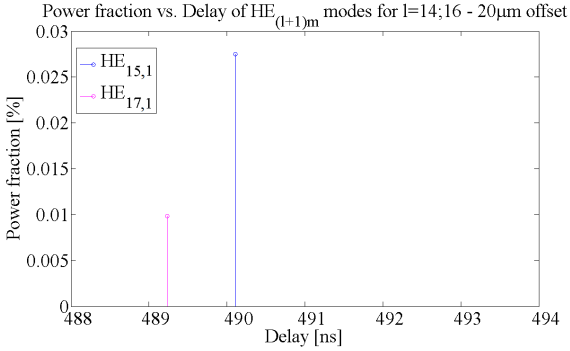

(b) HE_{15m} and HE_{17m} modes.

Figure 3.24: Power fraction of the $HE_{(l+1),m}$ modes for $l = 8,10,12,14,16$, for a fiber length of 100 m and a launch offset of 20 μm.

Analysing the modal power distribution of the existing modes, several conclusions can be obtained. Figure 3.20 shows that, for centred launching conditions, only the lower order modes are excited. In the case of having non-centred launching conditions, the largest amount of power coupled at the multimode fiber is distributed by higher order modes, as it is possible to see in Figure 3.21, Figure 3.22, Figure 3.23 and Figure 3.24. This results are consistent with the results presented in [36].

An important feature of the modal power distribution in the multimode fiber is that, for each mode type, the modes with a higher modal delay, which are the ones with a higher value of the radial mode number m, have more power coupled than the lowest ones, for the two analysed power launching conditions. This means that the higher modes within each mode type, carry more power, as it is possible to see, for example, in Figure 3.20 and 3.21.

Another important conclusion is that, for non-centred launching conditions, only the TE_{0m} and the odd $EH_{(l-1),m}$ and $HE_{(l+1),m}$ modes have coupled power. This characteristic is also observed for the 5

μm and 25 μm launch offset. The simulations results show that this happens due to the small modal amplitude values presented by these modes. Figure 3.25, Figure 3.26 and Figure 3.27 show the modal amplitude values for the first eight modes.

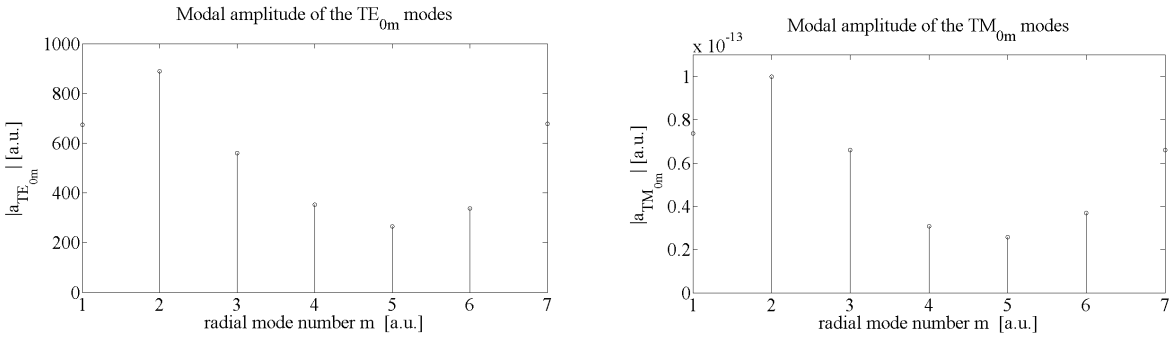

(a) TE_{0m} modes.

(b) TM_{0m} modes.

Figure 3.25: Modal amplitudes of the $TE_{0,m}$ and $TM_{0,m}$ modes.

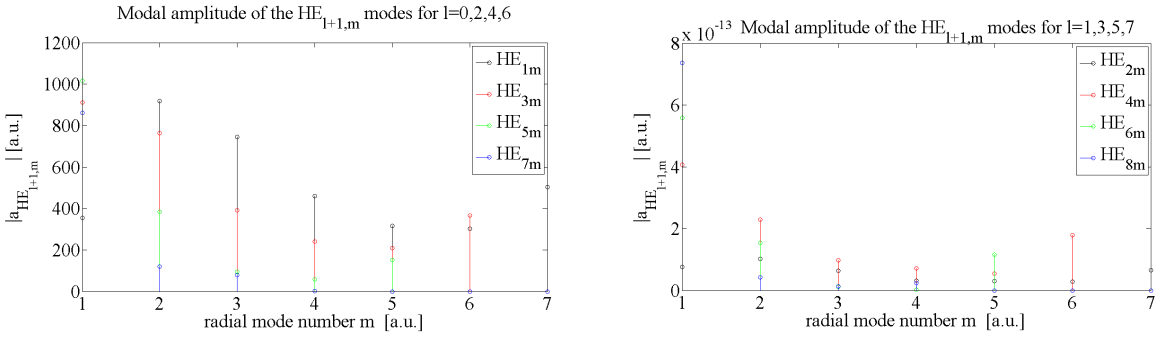

(a) $HE_{l+1,m}$ modes for l=0, 2, 4, 6.

(b) $HE_{l+1,m}$ modes for l=1, 3, 5, 7.

Figure 3.26: Modal amplitudes of the $HE_{l+1,m}$ modes, for the first eight values of the azimuth mode number l.

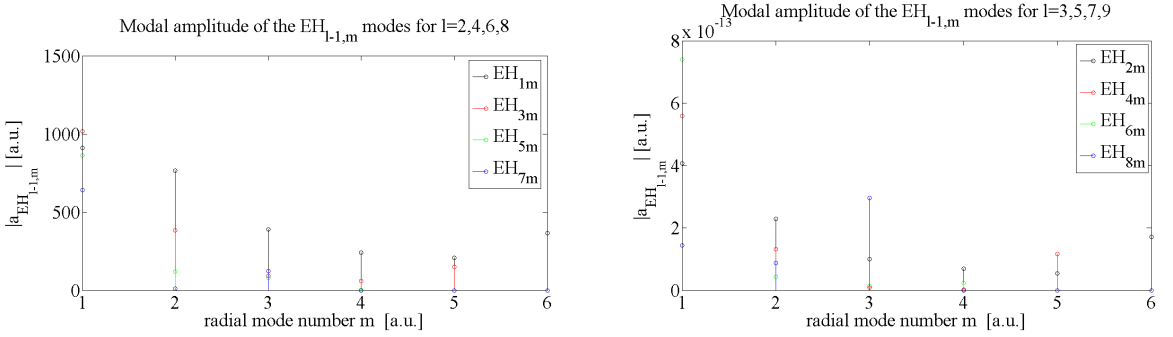

(a) $EH_{l-1,m}$ modes for l=2, 4, 6, 8.

(b) $EH_{l-1,m}$ modes for l=3, 5, 7, 9.

Figure 3.27: Modal amplitudes of the $EH_{l-1,m}$ modes, for the first eight values of azimuth mode number l.

Figures 3.25, 3.26 and 3.27 show that the modal amplitudes of the $TM_{0,m}$ and of the odd $HE_{l+1,m}$ and $EH_{l-1,m}$ modes are significantly smaller than the ones of the $TE_{0,m}$ and the ones of the even $HE_{l+1,m}$ and $EH_{l-1,m}$ modes. Since the modal power is affected by the modal amplitudes through its square (as it is possible to see in Equation 3.18), it is obvious that these modes do not have power coupled to them. In order to try to justify this effect, it is necessary to analyse the modal amplitude expression of each type of mode. Substituting the field expressions presented in Table 3.1 in the Equation 3.22, the modal amplitude of each mode type is obtained:

$$a_{TE_{0,m}} = \frac{\int_{A_\infty} \frac{J_0(U_{SMF}R)}{J_0(U_{SMF})} \frac{J_1(UR)}{J_1(U)} \sin(\phi) dA}{\int_{A_\infty} \frac{J_1^2(U)}{J_1{}^2(U)} dA} \tag{3.32}$$

$$a_{TM_{0,m}} = \frac{\int_{A_\infty} \frac{J_0(U_{SMF}R)}{J_0(U_{SMF})} \frac{J_1(UR)}{J_1(U)} \cos(\phi) dA}{\int_{A_\infty} \frac{J_1^2(U)}{J_1{}^2(U)} dA} \tag{3.33}$$

$$a_{HE_{l+1,m}} = \frac{\int_{A_\infty} \frac{J_0(U_{SMF}R)}{J_0(U_{SMF})} \frac{J_l(UR)}{J_l(U)} \cos(l\phi) dA}{\int_{A_\infty} \frac{J_l^2(U)}{J_l{}^2(U)} dA} \tag{3.34}$$

$$a_{EH_{l-1,m}} = \frac{\int_{A_\infty} \frac{J_0(U_{SMF}R)}{J_0(U_{SMF})} \frac{J_l(UR)}{J_l(U)} \cos(l\phi) dA}{\int_{A_\infty} \frac{J_l^2(U)}{J_l{}^2(U)} dA} \tag{3.35}$$

Analysing Equations 3.32, 3.33, 3.34 and 3.35, several conclusions can be obtained. It is possible to see that, for a x-polarized source, the expression of the modal amplitudes of the $HE_{l+1,m}$ and $EH_{l-1,m}$ modes is the same. This result is expected since they both have a dependence on the $\cos(l\phi)$ for its x component of the electrical field. It is also possible to see that the expression of the modal amplitude of the TM_{0m} modes is a particular case of the $HE_{l+1,m}$ and $EH_{l-1,m}$ modal amplitudes expression (for $l = 1$, the expression of the modal amplitudes of these three types of modes is the same). Another important fact is that all the modes that do not carry power have a azimuthal dependence on $\cos(l\phi)$. Although this is a necessary condition, this is not a sufficient one, since the even $HE_{l+1,m}$ and $EH_{l-1,m}$ modes have dependence on the $\cos(l\phi)$ and they do have power coupled. Nevertheless, the dependence of the x component of the multimode electric field on the odd order Bessel function combined with the $\cos(l\phi)$ dependence is common to all of these modes. A further analyse on this subject on future studies should be accomplished, in order to try to explain this behavior.

3.5 Conclusions

In this chapter, the principal features of the multimode fiber propagation are analysed. The four existing types of modes are identified and its modal field expressions are presented. The modal amplitude and the modal power expressions are presented and the power transfer function of the multimode fiber is

obtained. The results show that the smoothness of the multimode fiber frequency response is highly dependent on the UWB band used and on the fiber length. The study of the modal power distribution dependence on the launching conditions showed that a higher offset contributes to the existence of higher power coupled to the high order modes and, consequently, to the appearance of higher coupling losses. The increase of the launch offset increases the power coupling losses, due to the misalignment between the fibers. This work also showed that not all the existing modes have power coupled and that the modes with a higher radial number have more power coupled than the other ones.

Chapter 4

Transmission along multimode fiber

In this chapter, the transmission performance of the OFDM-UWB system is presented and analysed. As it was mentioned on Chapter 2, the inly noise source of the system is the electric noise associated to the opto-electric conversion performed by the PIN. The bit error ratio of the system is determined by the semi-analytic gaussian approach [31]. The performance of the system for centred launching conditions is presented in Section 4.1. In Section 4.2, the performance of the system for a launch offset of 20 μm is presented.

4.1 Results for centred launching conditions

The maximum assessed distance will be limited by the degradation/distortion of the transmitted signal. In order to analyse the system performance, it is necessary to analyse the bit error ratio of the overall system and the received constellations at the OFDM-UWB receiver output and determine which is the most limiting factor. It was defined that the target bit error ratio of the system is 10^{-4}, since with this value it is possible to use effectively forward error correction (FEC) algorithms and improve the system performance. The numerical results obtained in this chapter are obtained for a launch power of 1 mW, for a Mach-Zehnder modulator with a modulation index of 10% and a V_{bias} point of 2.5 V and for Bessel filters of 6^{th} order with a -3 dB bandwith of 400 MHz. The multimode fiber presents an attenuation of 1.5 dB/km. The equalizer transfer function is obtained by a polynomial interpolation of 3^{rd} order. The modulation index value, as well as the order of the equalization polynomial used in these simulations, are optimized. These optimizations are presented in Appendix E.

4.1.1 Single-band transmission

Figure 4.1, Figure 4.2, Figure 4.3 and Figure 4.4 show the performance of the system for the first four UWB sub-bands, respectively.

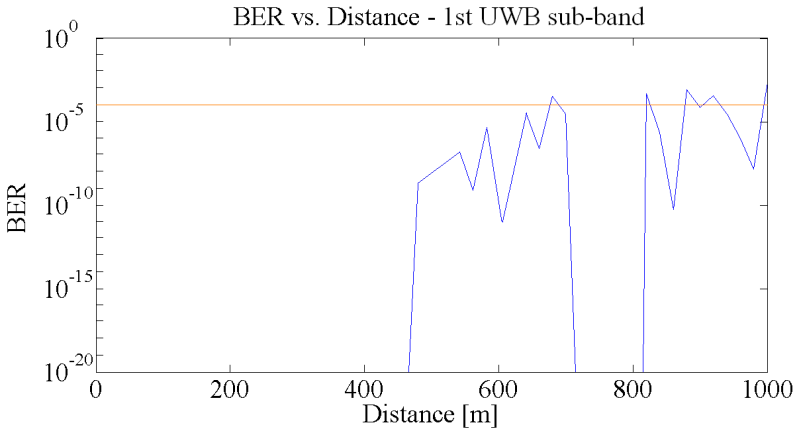

Figure 4.1: Performance of the OFDM-UWB system for the first OFDM-UWB sub-band. The orange line represents the target bit error ratio of this system.

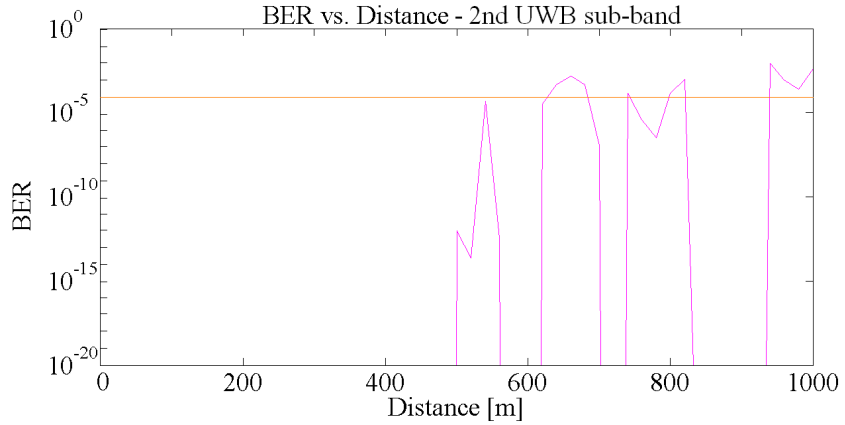

Figure 4.2: Performance of the OFDM-UWB system for the second OFDM-UWB sub-band. The orange line represents the target bit error ratio of this system.

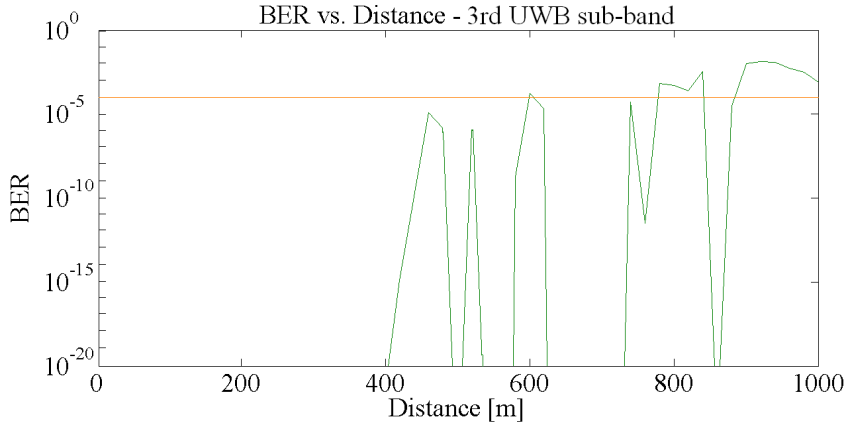

Figure 4.3: Performance of the OFDM-UWB system for the third OFDM-UWB sub-band. The orange line represents the target bit error ratio of this system.

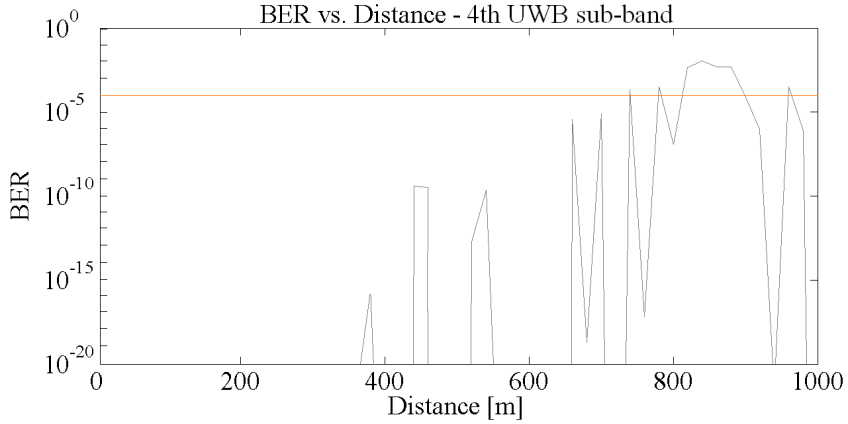

Figure 4.4: Performance of the OFDM-UWB system for the fourth OFDM-UWB sub-band. The orange line represents the target bit error ratio of this system.

Figure 4.1, Figure 4.2, Figure 4.3 and Figure 4.4 show that the degradation of the signal is strongly dependent on the sub-band used and increases with the increase of the fiber length. This result is expected since the multimode fiber transfer function presents a different behavior for the different RF sub-carriers, as it is possible to see in Figure 3.16 and in Figure 3.17, in Chapter 3. The smoother is the behavior of the multimode fiber transfer function for the sub-band used, the better is the system performance. Table 4.1 shows the BER and the SNR values for the first four UWB sub-bands, for fiber lengths of 100 m, 500 m and 1000 m.

Table 4.1: Performance of the overall system for fiber lengths of 100 m, 500 m and 1000 m, for the first four UWB sub-bands.

UWB sub-band	Fiber length [m]					
	100		500		1000	
	BER	SNR [dB]	BER	SNR [dB]	BER	SNR [dB]
1	$< 10^{-20}$	34.8	8.6×10^{-13}	34.1	4.3×10^{-3}	33.4
2	$< 10^{-20}$	37.0	$< 10^{-20}$	35.4	2.2×10^{-3}	33.2
3	$< 10^{-20}$	39.0	$< 10^{-20}$	31.6	7.76×10^{-4}	33.1
4	$< 10^{-20}$	33.4	$< 10^{-20}$	34.8	$< 10^{-20}$	33.4

From the analysis of the results presented in Table 4.1, it is possible to conclude that the good performance of the system is obtained due to its high SNR. The noise power has a low fixed value and the MMF transmission losses are quite low (for example, for 1000 m the transmission losses are 1.5 dB). So, the high SNR values result from the high signal power injected in the MMF. The differences between the SNR values for the same fiber length and different sub-bands can be explained by the MMF transfer function. Figure 4.5 and Figure 4.6 show the multimode fiber amplitude response for a fiber length of 100 m, in the third and the fourth UWB sub-bands, respectively.

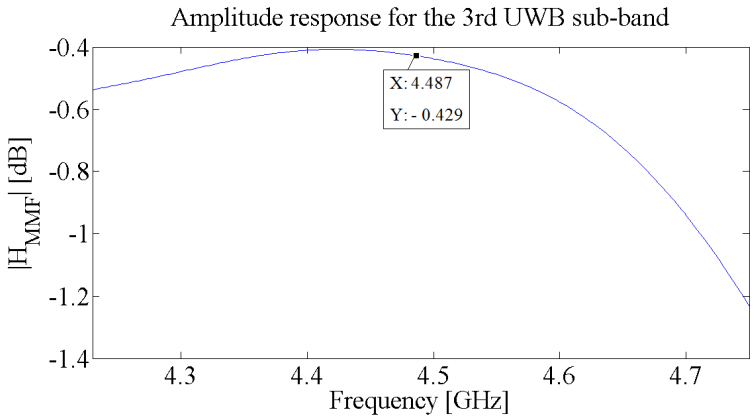

Figure 4.5: Multimode fiber amplitude for a fiber length of 100 m, in the third UWB sub-band.

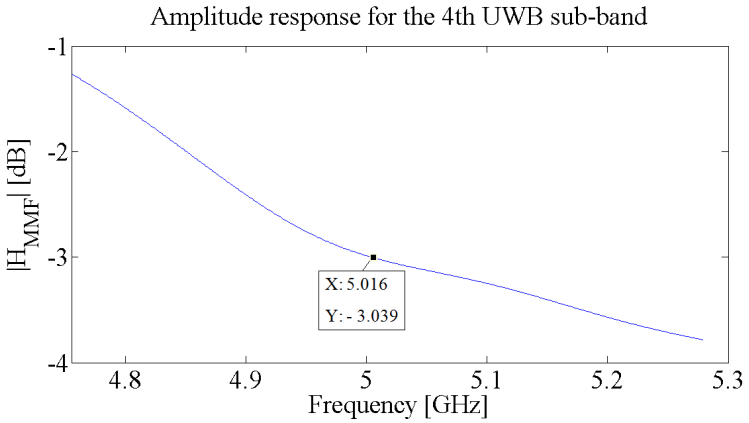

Figure 4.6: Multimode fiber amplitude response for a fiber length of 100 m, in the fourth UWB sub-band.

As it is possible to see in Figure 4.5 and in Figure 4.6, the amplitude response of the MMF fiber is very dependent on the sub-band use. The carrier frequency located on the third OFDM-UWB sub-band (f_{RF} =4.488 GHz) has an amplitude 2.6 dB higher than the carrier located on the fourth OFDM-UWB sub-band (f_{RF} =5.016 GHz). So, the OFDM-UWB signal power is higher when the third UWB sub-band is used which, consequently, generates a higher SNR. Another curious fact is that, for a fiber length of 1000 m, the system presents a bit error ratio inferior to 10^{-20}, for a transmission in the fourth OFDM-UWB sub-band. In fact, by looking at Figure 4.1, Figure 4.2, Figure 4.3 and Figure 4.4, it is possible to see that the fourth sub-band is the only sub-band that presents a BER value inferior to 10^{-4}. This happens due to the irregular behavior of the MMF transfer function, which can present very different values for the same fiber length, as long as the OFDM-UWB signals are transmitted in different sub-bands.

The maximum assessed distance is limited by the performance for the worst sub-band. It is possible to conclude from the analysis of the Figure 4.1, Figure 4.2, Figure 4.3 and Figure 4.4 that the worst sub-band is the third one, since it exceeds the target bit error ratio for a smaller distance than the other sub-bands used. So, the maximum assessed distance which guarantees a bit error ratio inferior to 10^{-4} is 600 m.

Another important component of the system that can limit the system performance is the equalizer. Figure 4.7 shows the equalizer transfer function, the polynomial interpolation and the pilots positions for a fiber length of 600 m, in the third UWB sub-band.

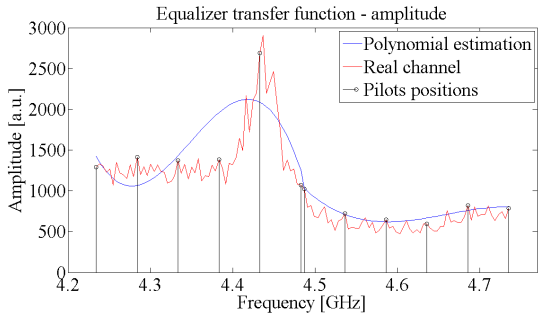

(a) Amplitude.

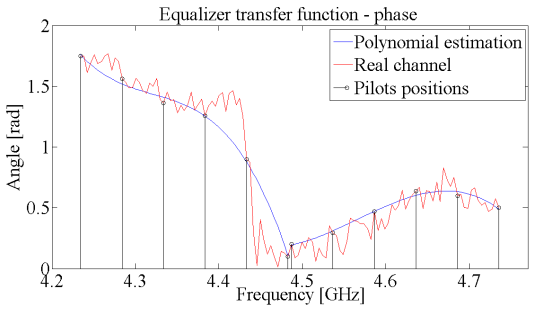

(b) Phase.

Figure 4.7: Equalizer transfer function for a fiber length of 600 m, in the third OFDM-UWB sub-band.

The results presented in Figure 4.7 show that the real channel and the equalizer transfer function are very different from each other. Although the equalizer tries to estimate the channel, its polynomial interpolation is not rigorous enough to do a satisfying estimation of the channel between the pilots. The channel presents a very sharp and irregular behaviour, which makes the polynomial interpolation too simple to estimate the channel. It is obvious from this analysis that the equalizer used in this system it is not a good estimator of this channel. The system performance can be improved by using a better equalizer.

Figure 4.8 and Figure 4.9 show the received constellations without noise, in the third UWB sub-band, for fiber lengths of 100 m, 500 m and 600 m, respectively.

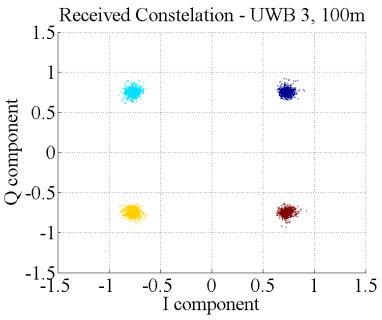

(a) Fiber length of 100 m.

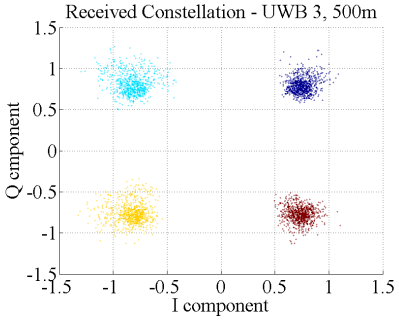

(b) Fiber length of 500 m.

Figure 4.8: Received constellations for fiber lengths of 100 m and 500 m, in the third UWB sub-band.

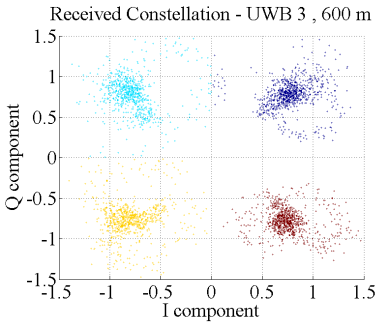

Figure 4.9: Received constellations for a fiber length of 600 m, in the third UWB sub-band.

Analysing the results presented in Figure 4.9 and Figure 4.8, it can be concluded that the distortion of the received constellations increases with the increase of the fiber length. In fact, for a fiber length of 600 m, which is the situation close to the target bit error ratio, the received constellation presents a very high distortion. In this situation, the OFDM-UWB receiver is not able to decode the signal properly, since some of the received constellation points are spread all over the complex plan. So, the signal distortion limits the maximum assessed distance. In order to determine which is the maximum assessed distance of this ystem for a BER of $10^{-}4$ with low distortion of the signal, some simulations were performed and the main conclusion is that, in order to have a perfectly decoded and demaped received constellation (this means, four agglomerations of points sufficiently apart from each other), the fiber length must not exceed 560 m. So, for single-band transmission and centred launching conditions, the OFDM-UWB system is mainly limited by signal distortion and the maximum assessed distance is 560 m.

4.1.2 Multi-band transmission

It is also be interesting to study the performance of the system in a multi-band environment. Figure 4.10 and Figure 4.11 show the system performance when two and three OFDM-UWB sub-bands are transmitted simultaneously, respectively. The performance of the overall system is given by the performance of the worst sub-band.

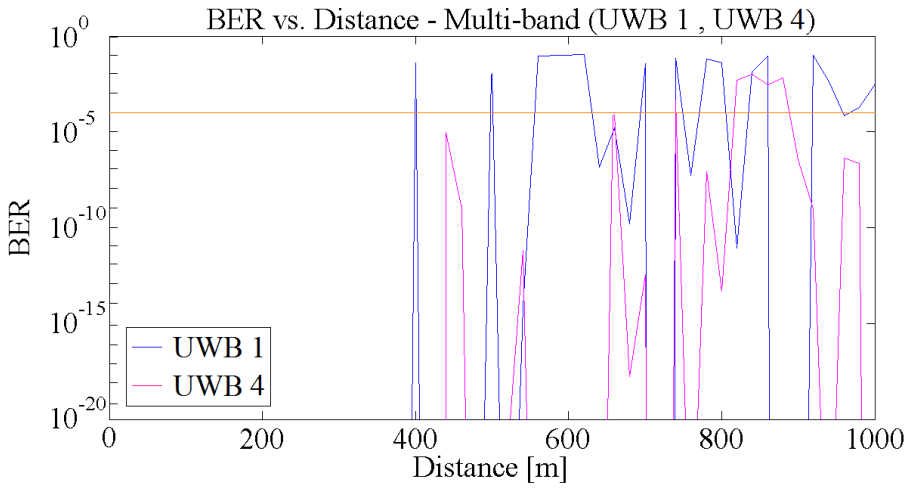

Figure 4.10: Performance of the OFDM-UWB system for simultaneous transmission of the first and the fourth UWB sub-bands. The orange line represents the target bit error ratio of the system.

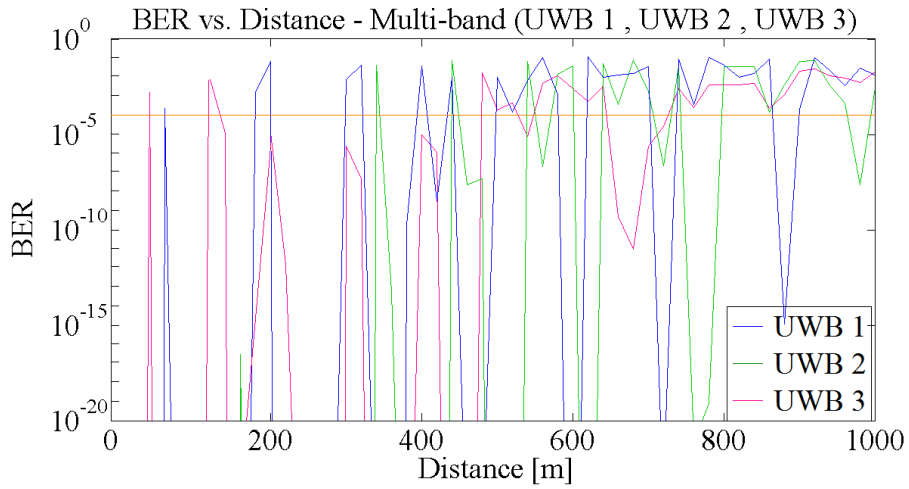

Figure 4.11: Performance of the OFDM-UWB system for simultaneous transmission of the first, second and third UWB sub-bands. The orange line represents the target bit error ratio of the system.

Analysing Figure 4.10 and Figure 4.11, it is possible to see that the degradation of the system increases substantially when more than one sub-band is used simultaneously. For the case presented in Figure 4.10, the sub-band that presents the worst performance is the first one. In this situation, the maximum assessed distance which guarantees a BER inferior to 10^{-4} is 380 m, which is 180 m less than when only a sub-band is used. In the situation presented in Figure 4.11, the performance of the system decreases drastically. When three sub-bands are transmitting simultaneously, the maximum assessed distance is reduced to less than 50 m. Figure 4.12 and Figure 4.13 show the received constellations for a fiber length of 200 m, in the case of having simultaneous transmission of the first three sub-bands.

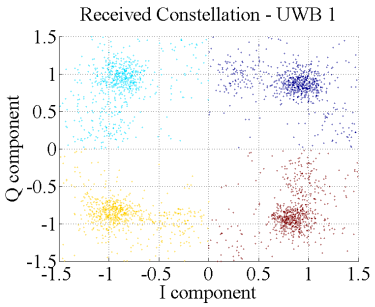

(a) UWB 1

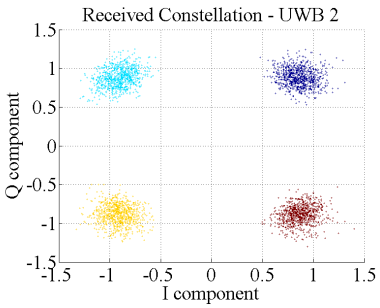

(b) UWB 2

Figure 4.12: Received constellations for a fiber length of 200 m, in the case of having simultaneous transmission of the first three sub-bands.

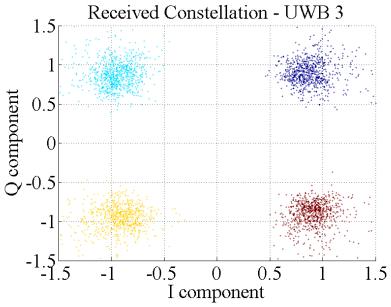

Figure 4.13: Received constellation for a fiber length of 200 m, in the case of having simultaneous transmission of the first three sub-bands - UWB 3.

Figure 4.12 and Figure 4.13 show that, although the second and the third UWB sub-band presents a good received constellation, the constellation presented in the first sub-band presents some significant distortion. This sub-band limits the performance of the overall system. One possible explanation of this effect is the interference between sub-bands. A further study of this subject will allow to confirm if the sub-band interference is responsible for the performance degradation of multi-band transmission.

4.2 Results for a launch offset of 20 μm

The previous BER curves and constellations were obtained of centred launching conditions. The analysis is now repeated for a 20 μm launch offset, in order to study the impact of having high-order modes excitation.

4.2.1 Single-band transmission

Figure 4.14, Figure 4.15, Figure 4.16 and Figure 4.17 present the bit error ratio of the first four UWB sub-bands, respectively.

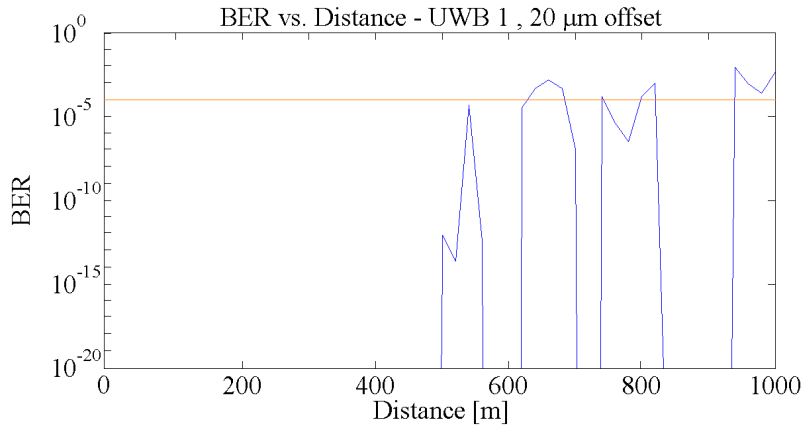

Figure 4.14: Performance of the OFDM-UWB system of the first OFDM-UWB sub-band, for a launch offset of 20 μm. The orange line represents the target bit error ratio of this system.

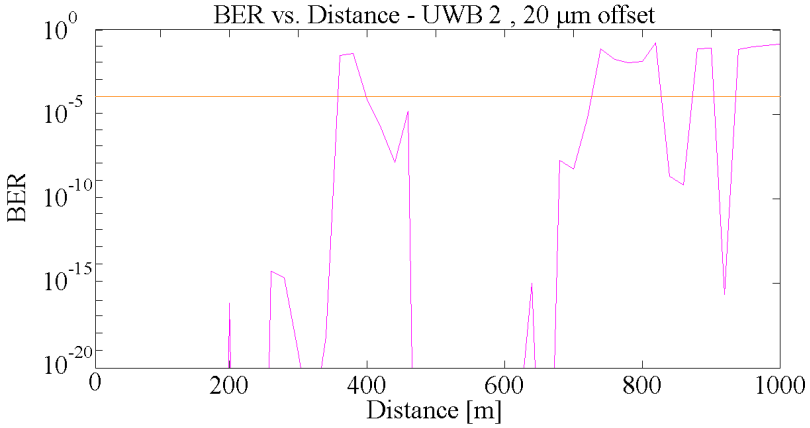

Figure 4.15: Performance of the OFDM-UWB system of the second OFDM-UWB sub-band, for a launch offset of 20 μm. The orange line represents the target bit error ratio of this system.

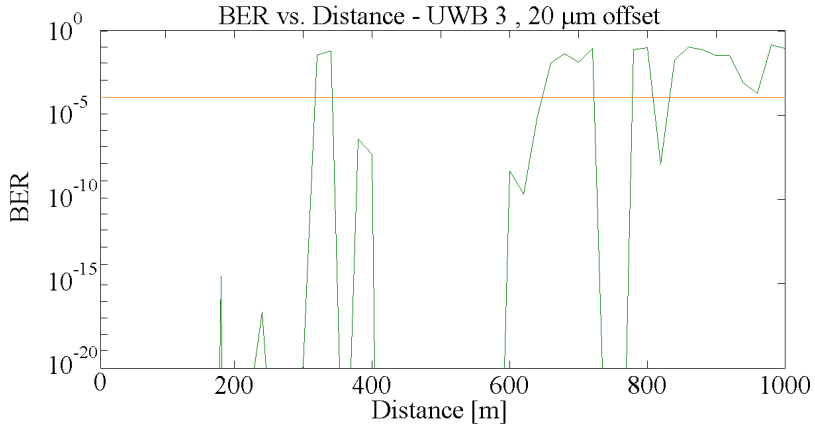

Figure 4.16: Performance of the OFDM-UWB system of the third OFDM-UWB sub-band, for a launch offset of 20 μm. The orange line represents the target bit error ratio of this system.

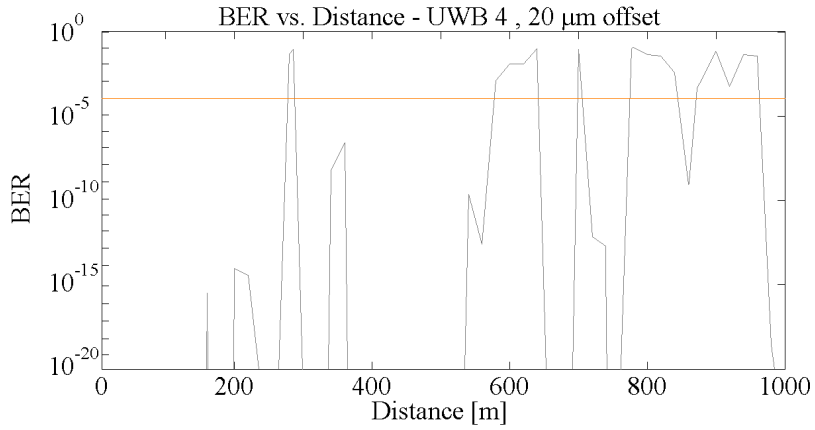

Figure 4.17: Performance of the OFDM-UWB system of the fourth OFDM-UWB sub-band, for a launch offset of 20 μ m. The orange line represents the target bit error ratio of this system.

Figure 4.14, Figure 4.15, Figure 4.16 and Figure 4.17 show that the degradation of the OFDM-UWB system for a launch offset of 20 μm is considerably higher than for centred launch conditions. As it was mentioned previous on the text, the performance of the overall system is limited by the performance of the worst sub-band. For a launch offset of 20 μm, the sub-band which presents a shorter distance for the target bit error rate (10^{-4}) is the fourth one. So, under this condition, the maximum assessed distance which guarantees a good performance of the OFDM-UWB system is about 270 m, less 330 m than for centred launching conditions. Table 4.2 shows the BER and the SNR values of the first four UWB sub-bands, for fiber lengths of 100 m, 500 m and 1000 m.

Table 4.2: Performance of the overall system for a launch offset of 20 μm, for fiber lengths of 100 m, 500 m and 1000 m, for the first four UWB sub-bands.

UWB sub-band	Fiber length [m]					
	100		500		1000	
	BER	SNR [dB]	BER	SNR [dB]	BER	SNR [dB]
1	$< 10^{-20}$	19.6	7.27×10^{-8}	22.6	9.27×10^{-2}	22.9
2	$< 10^{-20}$	24.7	$< 10^{-20}$	23.7	1.17×10^{-1}	19.1
3	$< 10^{-20}$	25.3	$< 10^{-20}$	25.3	8.93×10^{-2}	24.3
4	$< 10^{-20}$	20.1	1.34×10^{-20}	27.0	$< 10^{-20}$	24.6

Table 4.2 shows that the BER and the SNR values are worse for non-centred launching conditions. One possible explanation of this "extra" degradation of the performance of the system are the power coupling losses mentioned in the Chapter 3. These losses decrease the signal power which, consequently decreases the SNR and has a negative impact on the system performance. Once again, the performance of the system for a fiber length of 1000 m presents a BER inferior to 10^{-20}. This effect can be explained by the behavior of the multimode fiber transfer function, which can vary a lot from one distance to another. As for centred launching conditions, the difference between the SNR values for the same fiber length and different sub-bands can be explained by the multimode fiber amplitude response. Figure 4.18 and Figure 4.19 show the MMF amplitude response for a fiber length of 100 m, in the third and the fourth UWB sub-band, respectively.

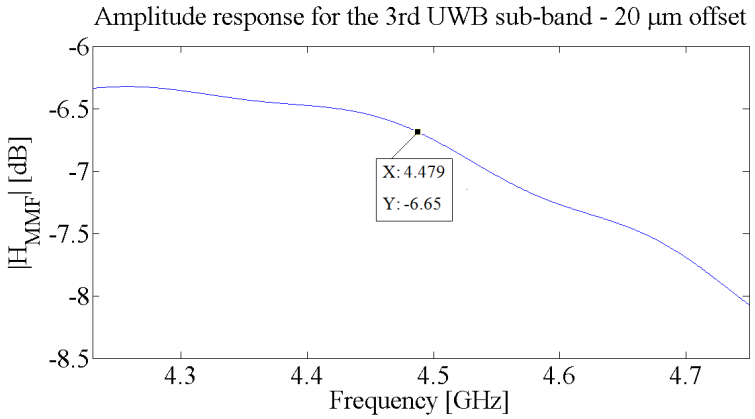

Figure 4.18: Multimode fiber amplitude response of a fiber length of 100 m, in the third UWB sub-band and for a launch offset of 20 μm.

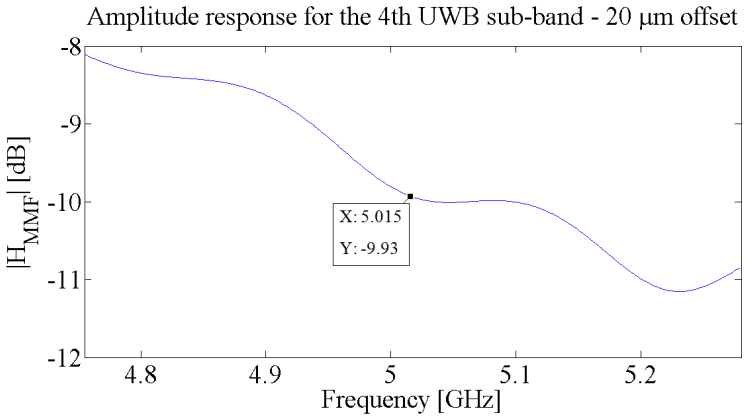

Figure 4.19: Multimode fiber amplitude response of a fiber length of 100 m, in the fourth UWB sub-band and for a launch offset of 20 μm.

Since the MMF transfer function for a launch offset of 20μm is sharper and more irregular than the centred one, a higher degradation and distortion of the OFDM-UWB signal is expected. It is possible to see in Figure 4.18 and Figure 4.19 that the carrier frequency located on the third OFDM-UWB sub-band has an amplitude about 3.3 dB higher than the carrier located on the fourth UWB sub-band. This effect leads to a higher SNR on the third sub-band.

Figure 4.20 shows the equalizer transfer function, the real channel and the pilots positions for a fiber length of 270 m, in the fourth UWB sub-band.

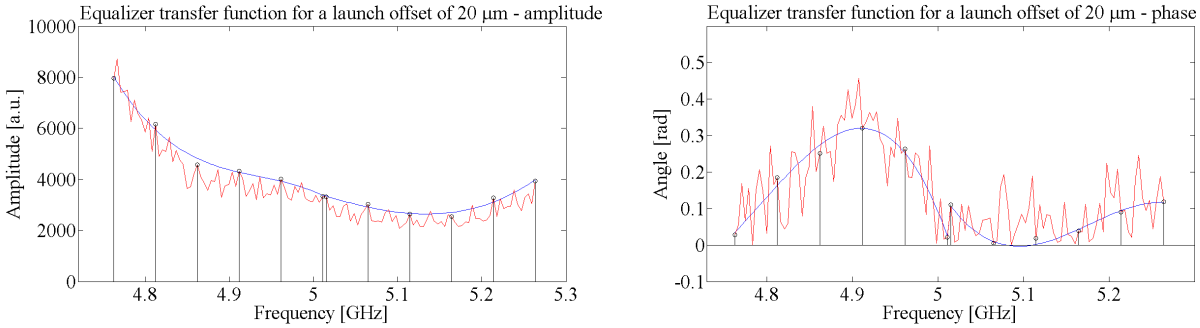

(a) Amplitude.

(b) Phase.

Figure 4.20: Channel transfer functions for a launch offset of 20 μm in the fourth UWB sub-band, for a fiber length of 270 m.

Figure 4.20 shows that the polynomial estimation of the channel given by the pilots information is very different from the real one. As a consequence of that fact, the equalizer can't provide a rigorous estimative of the channel between the pilots. The obtained results confirm that the equalizer used in this system is not adequate to estimate the MMF transfer function. A bad equalizer contributes to the increase of the distortion and the degradation of the system performance.

Figure 4.21 and Figure 4.22 show the received constellations for the fourth UWB sub-band (which is the sub-band that limits the system performance), respectively, for fiber lengths of 100 m, 270 m and 300 m.

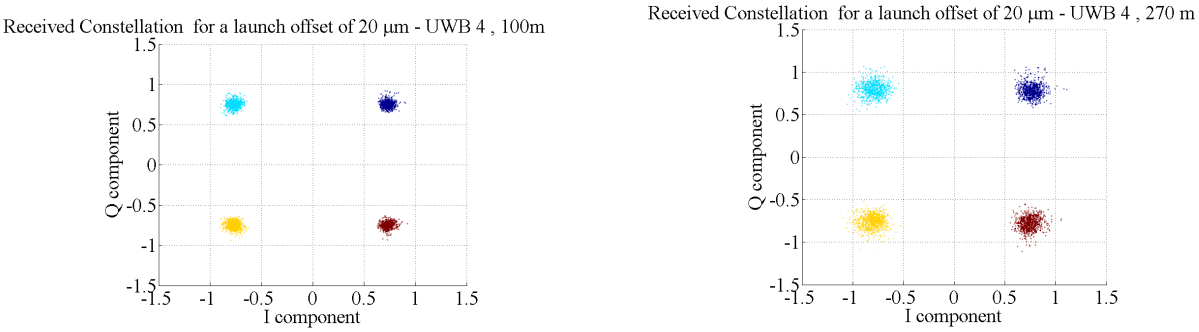

(a) Fiber length of 100 m.

(b) Fiber length of 270 m.

Figure 4.21: Received constellations of the fourth UWB sub-band for a launch offset of 20 μm, for fiber lengths of 100 m and 270 m.

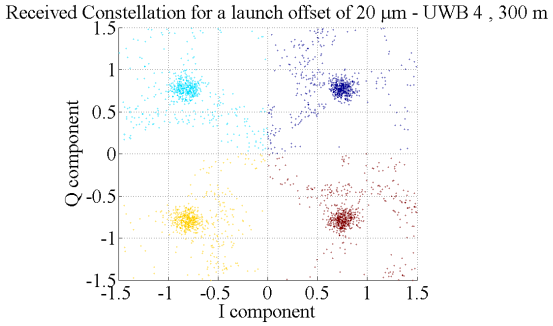

Figure 4.22: Received constellations of the fourth UWB sub-band for a launch offset of 20 μm for fiber lengths of 300 m.

Figure 4.21 and Figure 4.22 show that, like for the centred launching conditions, when we have a launch offset of 20 μm, the increase of the fiber length also increases the distortion of the transmitted signal. The QPSK received constellation can only be demaped correctly for a fiber length equal or inferior to 270 m. The numerical results show that for fiber lengths exceeding 270 m, the received constellation presents a very high distortion, what makes not possible to demap the received constellation correctly.

So, for a launch offset of 20 μm, the maximum assessed distance is 270 m.

4.2.2 Multi-band transmission

The use of a multi-band OFDM-UWB system will certainly have a strong impact on the BER of the overall system. Figure 4.23 and Figure 4.24 present the BER of the system for a launch offset of 20 μm,

when two and three OFDM-UWB sub-bands are transmitted simultaneously, respectively.

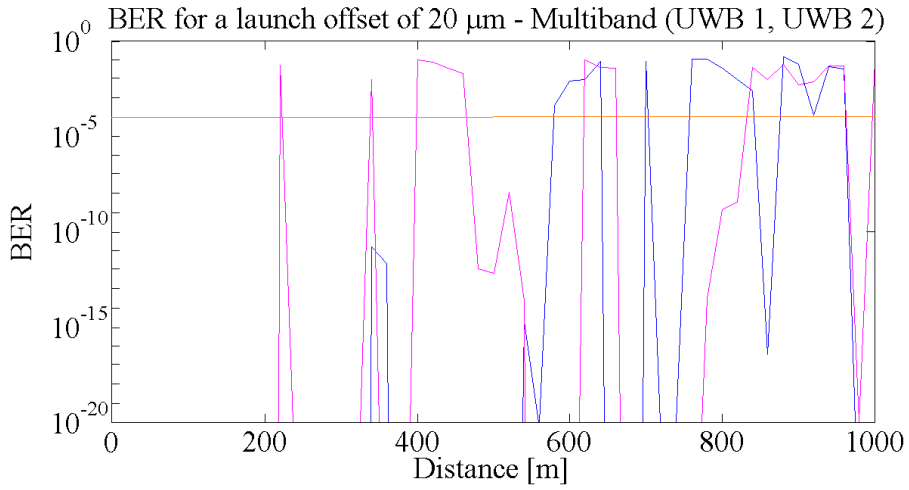

Figure 4.23: Performance of the OFDM-UWB system for simultaneous transmission of the first and second UWB sub-bands, for a launch offset of 20 μm. The orange line represents the target bit error ratio of the system.

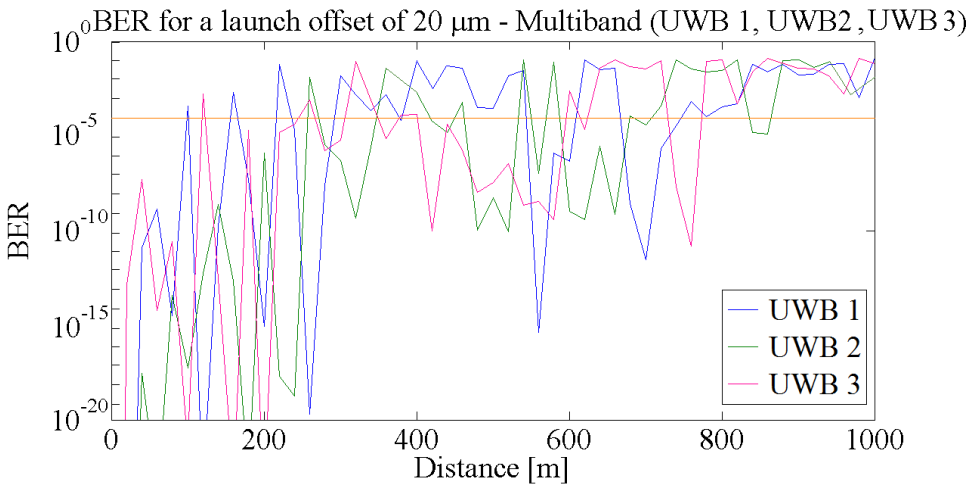

Figure 4.24: Performance of the OFDM-UWB system for simultaneous transmission of the first, second and third UWB sub-band, for a launch offset of 20 μm. The orange line represents the target bit error ratio of the system.

As it was seen for the centred launching conditions, the use of the multi-band technique increases the degradation of the performance of the overall system. In the case of having two sub-bands transmitting simultaneously, the maximum transmission distance is slightly superior to 200 m. For the transmission of three sub-bands simultaneously, the maximum transmission distance is less than 100 m. Nevertheless, this value is superior to the centred launching conditions, for the same conditions. Figure 4.25 and Fig-

ure 4.26 show the received constellations for a fiber length of 300 m, in the case of having simultaneous transmission of the first three sub-bands.

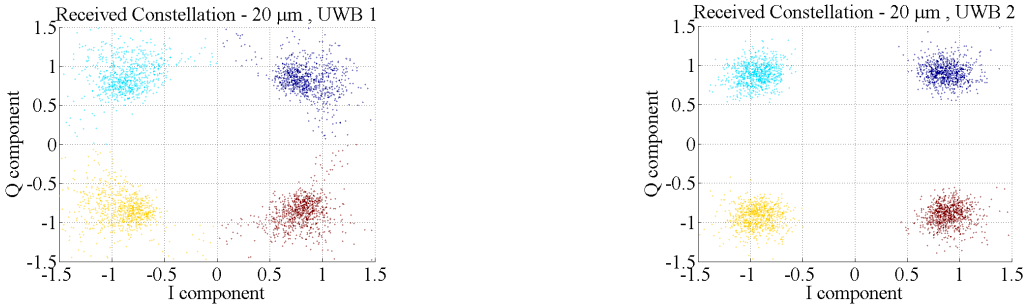

(a) UWB 1

(b) UWB 2

Figure 4.25: Received constellations for a fiber length of 300 m for a launch offset of 20 μm, of the case of having simultaneous transmission of the first three sub-bands.

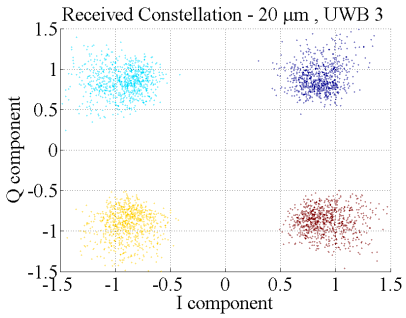

Figure 4.26: Received constellation for a fiber length of 300 m for a launch offset of 20 μm, in the case of having simultaneous transmission of the first three sub-bands - UWB 3.

Figure 4.25 and Figure 4.26 show that the received constellation which presents the worst quality is the one transmitted on the first UWB sub-band. As it was mentioned before in the text, a further study on the impact of having interference between the sub-bands would help to explain the reduction of the maximum assessed distance for multi-band situation.

4.3 Conclusions

In this chapter, the OFDM-UWB transmission system over multimode fiber has been analysed under several conditions. The performance of the system is strongly dependent on the MMF transfer function behavior and on the sub-bands used. The most restrictive factor of the multimode fiber transmission is the fiber length, once the higher is the length, the higher is the modal delay, which leads to a higher degradation (since it presents more dips) of the MMF transfer function.

Another important constraint of the performance of the system is the launching condition. The power coupling losses associated with the excitation of the high-order modes contributes to a significant decrease of the system performance. The transmission of multi-band OFDM-UWB signals also degrades significantly the performance of the system, for both launching conditions considered. It was concluded that the equalizer used in the OFDM-UWB receiver is not appropriate for the multimode fiber propagation system, since it can't estimate correctly the channel behaviour. Due to this fact, the equalizer won't be able to do a correct compensation of the channel transfer function between the pilots sub-carriers. The use of an equalizer that can perform a good estimation of the channel will contribute to improve the overall system performance.

Chapter 5

Conclusions and future work

In this chapter, the final conclusions and some suggestions for the future work in this subject are presented.

5.1 Final Conclusions

In this dissertation, the transmission of OFDM-UWB signals along multimode fiber is studied and evaluated through a numerical simulation. The increasing capacity demands of the current networks and the advantages of using multimode fiber optical systems are presented in Chapter 1.

In Chapter 2, the main components of the OFDM-UWB system are presented and analysed. Once this system transmits OFDM-UWB signals, its characteristics and its main advantages are presented. The system analysis in back-to-back configuration allowed to evaluate the performance of the system without multimode fiber transmission. The obtained results show that system performance depends on the number of sub-bands used.

In Chapter 3, the model of the multimode fiber propagation is developed from the theoretical model. The obtained results showed that the launching conditions, the fiber length and the carrier frequency of the UWB sub-band used have a significant impact on the multimode fiber transfer function. The excitation of higher order modes by setting non-centred launching conditions introduces coupling losses and contributes to the degradation of the multimode fiber transfer function.

In Chapter 4, the overall system performance is evaluated based on the bit error ratio, on the signal to noise ratio and on the received constellations. Three main conclusions are achieved: the launching conditions, the multimode fiber length and the number of UWB sub-bands used have a strong impact on the system performance. The maximum assessed distance for single-channel transmission and centred launching conditions is 560 m, while for a launch offset of 20 μm the maximum distance is only 270 m. In the case of having multi-band transmission of two sub-bands, for centred launching conditions the

maximum transmission distance is 380 m and for a launch offset of 20 μm, the maximum transmission distance is 210 m. For the simultaneous transmission of the first three UWB sub-bands, the maximum transmission distance is less than 50 m, for centred launching conditions, and less than 100 m, for a launch offset of 20 μm. It was also concluded that the equalizer used in this simulator is not appropriated to the multimode fiber propagation, since it can't estimate correctly the channel's behavior between the pilots. A suggestion that will improve the system's performance is to use an equalizer more able to the channel's estimation between the pilots.

5.2 Future Work

The most obvious future direction of this dissertation is to improve the MMF link by enhancing the bandwidth-distance while reducing the system complexity and cost. As a result of the developed work in this dissertation, some suggestions for future work to continue/complement this subject are:

- study the use of equalizers more efficient than the one considered in this dissertation;
- study the impact of having chromatic dispersion on the multimode fiber propagation model;
- study the impact of having non-linear effects on the multimode fiber propagation model;
- study the use of other modulation techniques for the OFDM sub-carriers like, for example, 16-QAM.

Appendix A

Mathematical Background

In this section, some mathematical relationships are presented [32]. Applying these expressions allows to simplify some of the equations presented in this dissertation.

A.1 Relationships between Cartesian and cylindrical polar coordinates

$$\begin{cases} x = r\cos(\phi) \\ y = r\sin(\phi) \end{cases} \tag{A.1}$$

$$\begin{cases} r = \sqrt{x^2 + y^2} \\ \\ \phi = \arctan\frac{y}{x} \end{cases} \tag{A.2}$$

A.2 Bessel Functions

Bessel function equation

$$\left\{ x^2 \frac{d^2}{dx^2} + x\frac{d}{dx} + (x^2 - \alpha^2) \right\} y = 0 \tag{A.3}$$

Bessel function of first kind and of the modified Bessel function of the second kind - Recurrence relations

$$J_{-l}(r) = \{-1\}^l J_l(r) \tag{A.4}$$

$$K_{-l}(r) = K_l(r) \tag{A.5}$$

$$J_l(r) = \frac{r}{2l}\left\{J_{l-1}(r) + J_{l+1}(r)\right\} \tag{A.6}$$

$$J_{l+1}(r) = \frac{l}{r}\left\{J_l(r) - \frac{dJ_l(r)}{dr}\right\} \tag{A.7}$$

$$J_{l-1}(r) = \frac{l}{r}\left\{J_l(r) + \frac{dJ_l(r)}{dr}\right\} \tag{A.8}$$

$$\frac{dJ_l(r)}{dr} = \frac{1}{2}\left\{J_{l-1}(r) - J_{l+1}(r)\right\} \tag{A.9}$$

$$\frac{dJ_0(r)}{dr} = -J_1(r) \tag{A.10}$$

$$K_l(r) = \frac{r}{2l}\left\{K_{l+1}(r) - K_{l-1}(r)\right\} \tag{A.11}$$

$$K_{l+1}(r) = \frac{l}{r}\left\{K_l(r) - \frac{dK_l(r)}{dr}\right\} \tag{A.12}$$

$$K_{l-1}(r) = -\frac{l}{r}\left\{K_l(r) - \frac{dK_l(r)}{dr}\right\} \tag{A.13}$$

$$\frac{dK_l(r)}{dr} = -\frac{1}{2}\left\{K_{l-1}(r) + K_{l+1}(r)\right\} \tag{A.14}$$

$$\frac{dK_0(r)}{dr} = -K_1(r) \tag{A.15}$$

Bessel function of first kind and of the modified Bessel function of the second kind - Indefinite integrals

$$\int rJ_0(ar)dr = \frac{a}{a}J_1(ar) \tag{A.16}$$

$$\int rJ_l{}^2(ar)dr = \frac{r^2}{2}\left\{J_l^2(ar) - J_{l-1}(ar)J_{l+1}(ar)\right\} \tag{A.17}$$

$$\int rJ_0{}^2(ar)dr = \frac{r^2}{2}\left\{J_0^2(ar) + J_1^2(ar)\right\} \tag{A.18}$$

$$\int \frac{J_1{}^2(ar)}{2}dr = -\frac{1}{2}\left\{J_0^2(ar) + J_1^2(ar)\right\} \tag{A.19}$$

$$\int rJ_l(ar)J_l(br)dr = \frac{r^2}{a^2-b^2}\left\{bJ_l^2(ar)J_{l-1}(br) - aJ_l(br)J_{l-1}(ar)\right\} \tag{A.20}$$

$$\int rK_l{}^2(ar)dr = \frac{r^2}{2}\left\{K_l^2(ar) - K_{l-1}(ar)K_{l+1}(ar)\right\} \tag{A.21}$$

$$\int rK_0{}^2(ar)dr = \frac{r^2}{2}\left\{K_0^2(ar) - K_1(ar)^2\right\} \tag{A.22}$$

$$\int rK_l(ar)K_l(br)dr = \frac{r^2}{a^2-b^2}\left\{bK_l^2(ar)K_{l+1}(br) - aK_l(br)K_{l+1}(ar)\right\} \tag{A.23}$$

$$\int rJ_l(ar)K_l(br)dr = \frac{r^2}{a^2-b^2}\left\{aK_l^2(ar)J_{l+1}(br) - bJ_l(br)K_{l+1}(ar)\right\} \tag{A.24}$$

Appendix B

Numerical results for $\lambda = 1310$ nm

B.1 Mode Classification

$TE_{0,m}$ and $TM_{0,m}$ modes

The propagation constants of the $TE_{0,m}$ and $TM_{0,m}$ modes for can be determined numerically by solving the Equation 3.12. The obtained results are presented in Table B.1. A graphical interpretation of the results is shown in Figure B.1.

Table B.1: Computed eigenvalue for $TE_{0,m}$ and $TM_{0,m}$ modes.

$TE_{0,m}$, $TM_{0,m}$ modes			
m	u_{0m}	w_{0m}	β_{0m} $[10^6 \mathrm{m}^{-1}]$
1	24.5605	5.6504	7.0302
2	21.7216	12.7797	7.0452
3	18.7756	16.8114	7.0587
4	15.7935	19.6395	7.0704
5	12.7915	21.7146	7.0801
6	9.7752	23.2291	7.0878
7	6.7447	24.2828	7.0934
8	3.6850	24.9312	7.0970

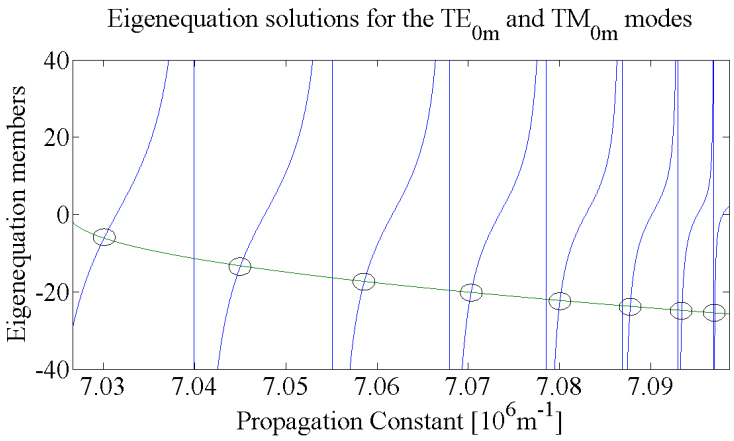

Figure B.1: Graphical solutions of the eigenvalue equation for $TE_{0,m}$ and $TM_{,0m}$ modes.

The $TE_{0,m}$ and $TM_{0,m}$ modes have one more mode for $\lambda = 1310$ nm than the for the corresponding modes for $\lambda = 1550$ nm.

$HE_{l+1,m}$ modes

For every fixed value of l, the propagation constants of the $HE_{l+1,m}$ modes are determined numerically by solving the Equation 3.13, for $l = 0$, and Equation 3.13, for $l \geq 1$. The obtained results are presented in Table B.2, for $l = 0,1,2,3,4$. A graphical interpretation of the eigenequation solutions for the HE_{1m} modes is shown in Figure B.2. The number of the allowed modes is given by the number of intersections in the graphic.

Table B.2: Computed eigenvalue for $HE_{l+1,m}$ modes for $l = 0,1,2,3,4$.

$HE_{l+1,m}$ modes						
m	u_{lm}	w_{lm}	$\beta_{1m}[10^6\mathrm{m}^{-1}]$	$\beta_{2m}[10^6\mathrm{m}^{-1}]$	$\beta_{3m}[10^6\mathrm{m}^{-1}]$	$\beta_{4m}[10^6\mathrm{m}^{-1}]$
1	25.2048	0.0000	7.0377	7.0302	7.0381	7.0309
2	25.1923	0.7036	7.0521	7.0452	7.0525	7.0460
3	25.1797	1.0618	7.0647	7.0587	7.0651	7.0595
4	25.1672	1.3266	7.0754	7.0704	7.0758	7.0712
5	25.1546	1.5467	7.0841	7.0801	7.0845	7.0809
6	25.1420	1.7392	7.0908	7.0878	7.0912	7.0886
7	25.1294	1.9124	7.0954	7.0934	7.0958	7.0943
8	25.1169	2.0711	7.0980	7.0970	———	———

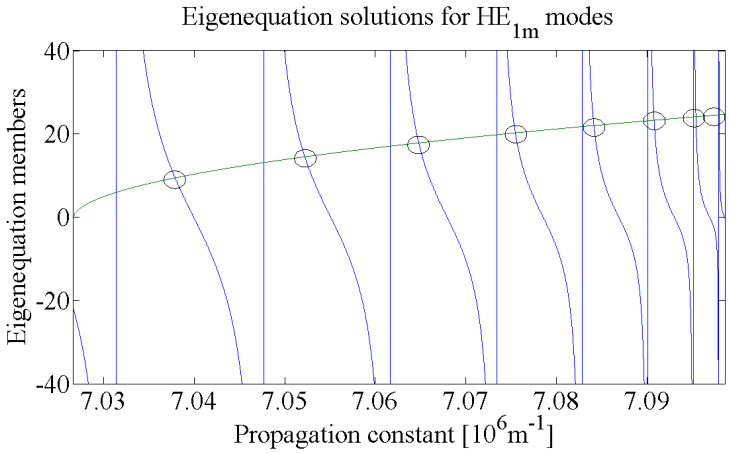

Figure B.2: Graphical solutions of the eigenvalue equation for HE_{1m} modes.

Like for $\lambda = 1550$ nm, there is a cut-off value that when is exceeded, no more mode numbers are allowed. For $\lambda = 1310$ nm, the last allowed mode is the $HE_{21,m}$. For the successive $HE_{22,m}$, the eigenequation does not present any solution, as it is possible to see in Figure B.3.

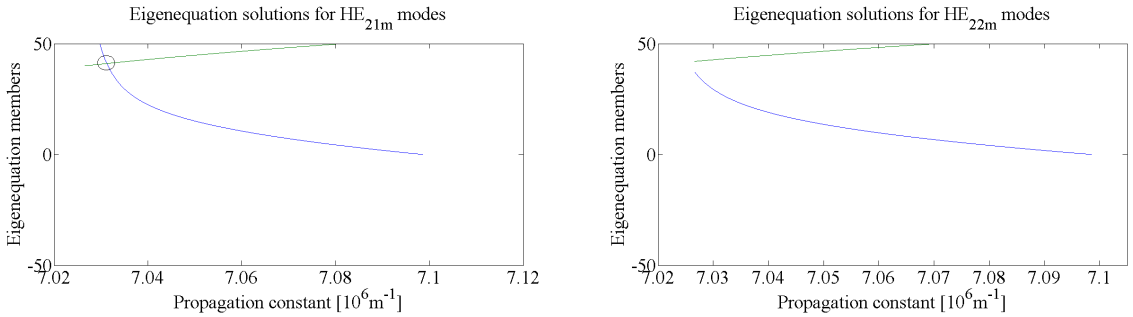

(a) $HE_{21,m}$ modes.

(b) $HE_{22,m}$ modes.

Figure B.3: Eigenequation solutions near to the cut-off value. For the $HE_{22,m}$, there is no intersections between the eigenequation members, so the $HE_{21,m}$ mode is the last allowed mode for this fiber.

$EH_{l-1,m}$ modes

The propagation constants of the $EH_{l-1,m}$ modes can be determined numerically by solving the Equation 3.14, for $l > 1$.Table B.3 show the numerical results for $l = 1,2,3,4$. A graphical interpretation of the results for the $EH_{1,m}$ modes is shown in Figure B.4. The number of the allowed modes is given by the number of intersections of the eigenequation members.

Table B.3: Computed eigenvalue for $EH_{l-1,m}$ modes for $l = 2,3,4,5$.

$EH_{l-1,m}$ modes						
m	u_{lm}	w_{lm}	$\beta_{1m}[10^6\mathrm{m}^{-1}]$	$\beta_{2m}[10^6\mathrm{m}^{-1}]$	$\beta_{3m}[10^6\mathrm{m}^{-1}]$	$\beta_{4m}[10^6\mathrm{m}^{-1}]$
1	25.2048	0.0000	7.0381	7.0309	7.0392	7.0324
2	25.1923	0.7036	7.0525	7.0460	7.0537	7.0476
3	25.1797	1.0618	7.0651	7.0595	7.0664	7.0612
4	25.1672	1.3266	7.0758	7.0712	7.0771	7.0729
5	25.1546	1.5467	7.0845	7.0809	7.0858	7.0827
6	25.1420	1.7392	7.0912	7.0886	7.0926	7.0905
7	25.1294	1.9124	7.0958	7.0943	———	———

Table B.3 shows that the increasing of the azimuth number leads to the decreasing number of allowed modes.

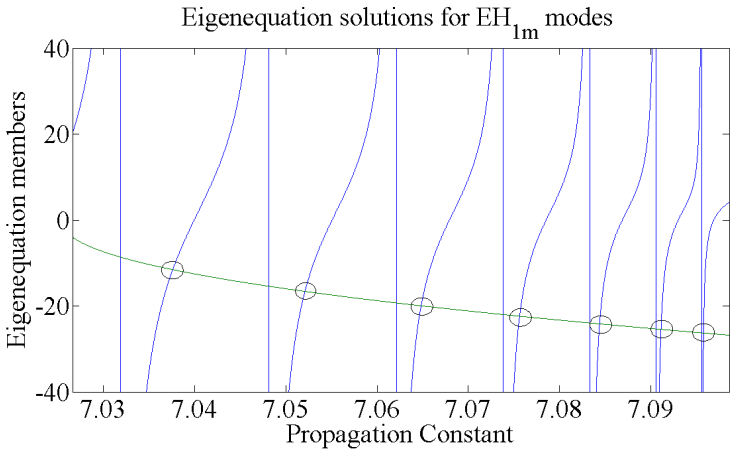

Figure B.4: Graphical solutions of the eigenvalue equation for $EH_{1,m}$ modes.

Like for the $HE_{l+1,m}$ modes, there is a finite number of allowed $EH_{l-1,m}$ modes that can propagate in the multimode fiber. Figure B.5 shows the mode cut-off situation for the multimode fiber used.

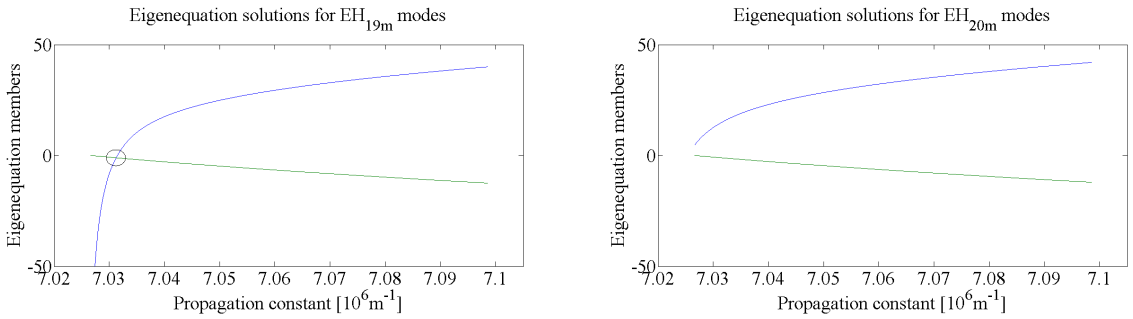

(a) $EH_{19,m}$ modes.

(b) $EH_{20,m}$ modes.

Figure B.5: Eigenequation solutions near to the cut-off value. For the $EH_{20,m}$, there is no intersections between the eigenequation members, so the $EH_{19,m}$ mode is the last allowed mode for this fiber.

This results are coincident with the results obtained in [34].

B.2 Modal power distribution

In the following figures, the modal power distribution for centred and launch offset of 20 μm for fiber length of 100 m are presented.

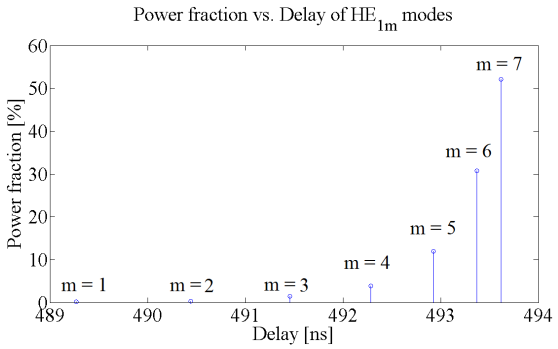

Figure B.6: Power fraction of the $HE_{1,m}$ modes for centred launching conditions. In this situation, only the lower order $HE_{1,m}$ modes are excited.

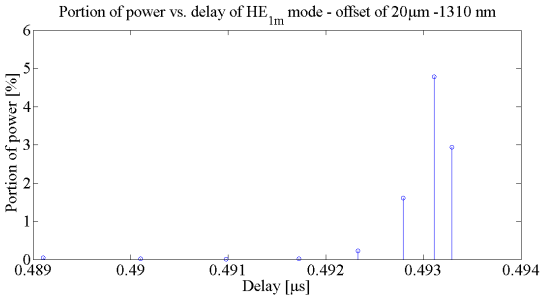

(a) HE_{1m} modes.

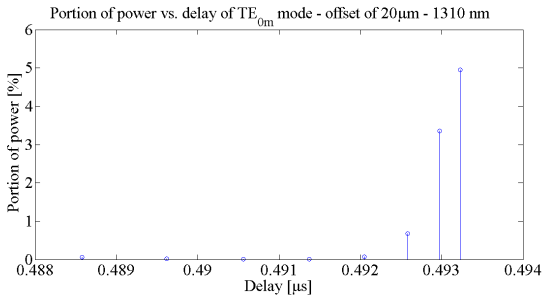

(b) TE_{0m} modes.

Figure B.7: Power fraction of the $HE_{1,m}$ and $TE_{0,m}$ modes for a launch offset of 20 μm.

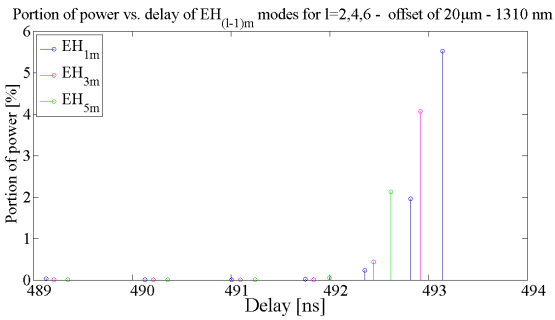

(a) EH_{1m}, EH_{3m} and EH_{5m} modes.

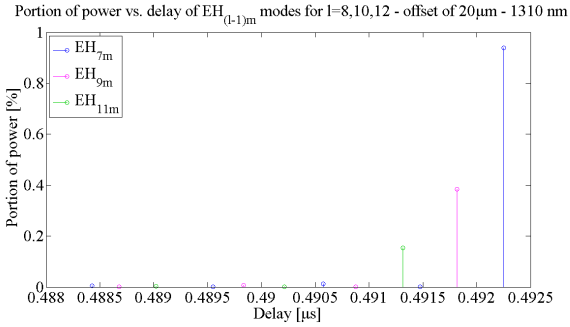

(b) EH_{7m}, EH_{9m} and EH_{11m} modes.

Figure B.8: Power fraction of the $EH_{(l-1),m}$ modes for $l = 2,4,6,8,10,12$, for a launch offset of 20 μm.

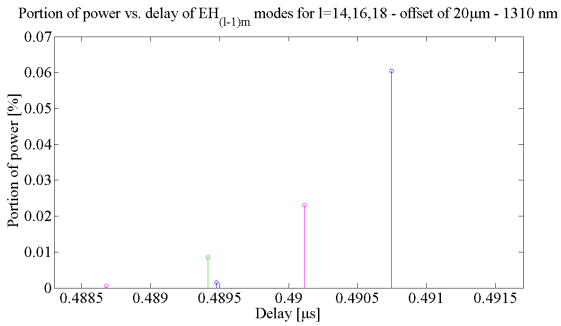

(a) EH_{13m}, EH_{15m} and EH_{17m} modes.

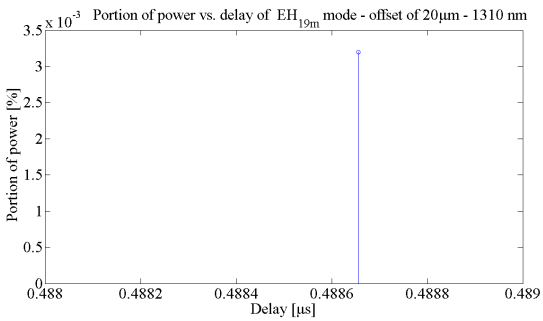

(b) EH_{19m} modes.

Figure B.9: Power fraction of the $EH_{(l-1),m}$ modes for $l = 14,16,18,20$, for a launch offset of 20 μm.

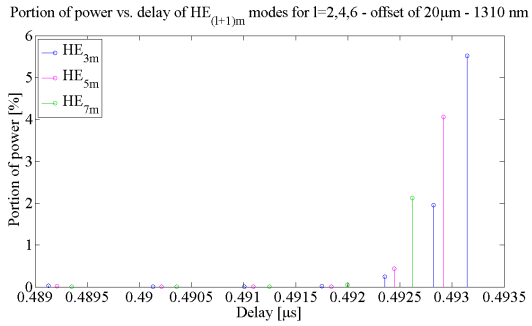

(a) HE_{3m}, HE_{5m} and HE_{7m} modes.

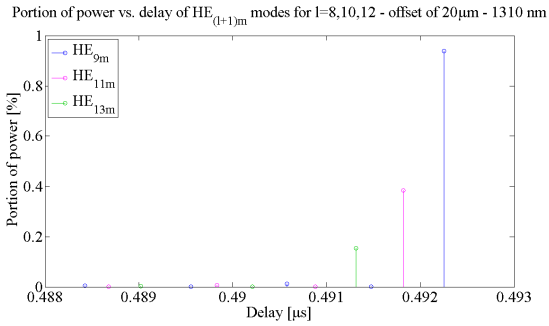

(b) HE_{9m}, HE_{11m} and HE_{13m} modes.

Figure B.10: Power fraction of the $HE_{(l+1),m}$ modes for $l = 4,6,8,10,12,14$, for a launch offset of 20 μm.

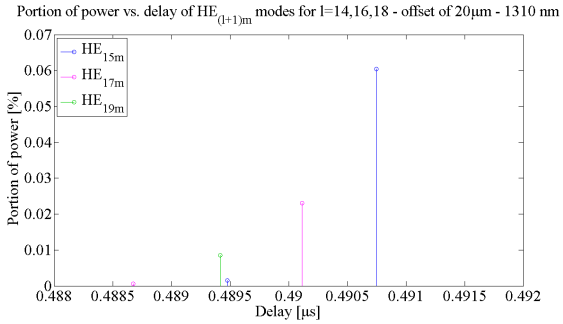

(a) HE_{15m}, HE_{17m} and HE_{19m} modes.

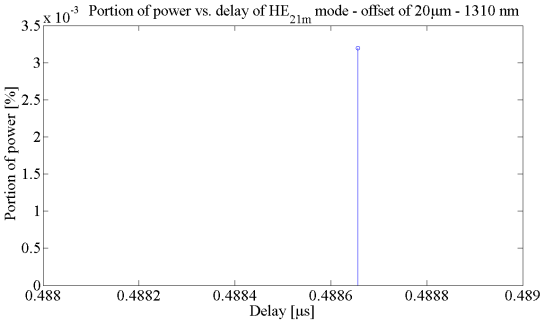

(b) HE_{21m} modes.

Figure B.11: Power fraction of the $HE_{(l+1),m}$ modes for $l = 14,16,18,20$, for a launch offset of 20 μm.

Since there are more allowed modes for $\lambda = 1310$ nm than for $\lambda = 1550$ nm, for non-centred launching conditions, the total launched power is split for more modes.

Appendix C

Mathematical derivation of the modal amplitude expression

In this section, the mathematical derivation of the modal amplitude expression is presented.

Assuming that the fiber is a non-absorbing waveguide, the electromagnetic modal fields satisfy the following orthogonality condition [34]:

$$\int_{A_\infty} \{\mathbf{E}_{t,lm}(\rho,\phi) \times \mathbf{H}^*_{t,lm}(\rho,\phi)\} \cdot \mathbf{z} dA = 0, \tag{C.1}$$

In order to proceed with the derivation of the modal amplitudes as consequent to a given source field excitation, the total electromagnetic field must be equalized at the launching section at $z = 0$. The total field expansion in Equation 3.16, evaluated at the launching section at $z = 0$, must coincide with the source electromagnetic field $\mathbf{E}_s$,$\mathbf{H}_s$. Due to this fact, and assuming that the longitudinal dependence of the source field can be factorized using the same phase factor $e^{j(wt-\beta_s z)}$ shown in Equation 3.2, the electromagnetic field expansion can be written as [34]:

$$\mathbf{E}_s(\rho,\phi) = \sum_{l,m} a_{lm} \{\mathbf{E}_{t,lm}(\rho,\phi) + E_{z,lm}(\rho,\phi)\mathbf{z}\} \tag{C.2}$$

$$\mathbf{H}_s(\rho,\phi) = \sum_{l,m} a_{lm} \{\mathbf{H}_{t,lm}(\rho,\phi) + H_{z,lm}(\rho,\phi)\mathbf{z}\} \tag{C.3}$$

For each generic bound mode characterized by the index (l,m), the following vector product is formed by the integration over the infinite fiber cross-section A_∞ between the source electric field $\mathbf{E}_s$ and the complex conjugate of the normalized magnetic field $\mathbf{H}^*_s$:

$$\int_{A_\infty}\{\mathbf{E}_s(\rho,\phi)\times\mathbf{H}_s^*(\rho,\phi)\}\cdot\mathbf{z}dA = \tag{C.4}$$

$$= \int_{A_\infty}\sum_{l,m} a_{lm}\{[\mathbf{E}_{t,lm}(\rho,\phi)+\mathbf{E}_{z,lm}(\rho,\phi)\mathbf{z}]\times[\mathbf{H}_{t,lm}^*(\rho,\phi)+\mathbf{H}_{z,lm}^*(\rho,\phi)\mathbf{z}]\}\cdot\mathbf{z}dA$$

Simplifying and manipulating Equation C.4, allows to determinate the general expression of the modal amplitude of each (l,m) mode:

$$a_{l,m} = \frac{\int_{A_\infty}\{\mathbf{E}_s(\rho,\phi)\times\mathbf{H}_{t,l,m}^*(\rho,\phi)\}\cdot\mathbf{z}dA}{\int_{A_\infty}\mathbf{E}_{t,l,m}(\rho,\phi)\times\mathbf{H}_{t,l,m}^*(\rho,\phi)\cdot\mathbf{z}dA} \tag{C.5}$$

Weakly guiding approximation

The modal fields presented in Table 3.1 are defined for weakly guiding waveguides, so it is possible to simplify the modal amplitude expression presented in Equation C.5, once the following expression is valid under the weakly guiding approximation [34]:

$$\mathbf{H}_{t,lm}(\rho,\phi) \cong \frac{n_{co,clad}}{Z_0}\mathbf{z}\times\mathbf{E}_{t,lm}(\rho,\phi) \tag{C.6}$$

where $Z_0 = \sqrt{\frac{\mu_0}{\varepsilon_0}}$ represents the vacuum impedance, μ_0 and ε_0 represents the vacuum magnetic and electric permittivity, respectively.

Applying the weakly waveguide approximation presented in Equation C.6 and the vector identity $\mathbf{e}\times(\mathbf{z}\times\mathbf{e}) = \mathbf{z}$ to the integrand functions of the modal amplitude expression, simplifies the modal amplitude integrand functions:

$$\mathbf{E}_{t,lm}(\rho,\phi)\times\mathbf{H}_{t,lm}^*(\rho,\phi)\cdot\mathbf{z} = \frac{n_{co,clad}}{Z_0}\mathbf{E}_{t,lm}(\rho,\phi)\times[\mathbf{z}\times\mathbf{E}_{t,l,m}^*(\rho,\phi)]\cdot\mathbf{z} = \frac{n_{co,clad}}{Z_0}|\mathbf{E}_{t,l,m}(\rho,\phi)|^2 \tag{C.7}$$

$$\mathbf{E}_s(\rho,\phi)\times\mathbf{H}_{t,lm}^*(\rho,\phi)\cdot\mathbf{z} = \frac{n_{co,clad}}{Z_0}\mathbf{E}_s(\rho,\phi)\times\mathbf{z}\times\mathbf{E}_{t,lm}^*(\rho,\phi)\cdot\mathbf{z} \tag{C.8}$$

This means that, under the weakly waveguide approximation, the modal amplitude in Equation C.5 can be expressed only in terms of the electric field. Substituting Equation C.7 and Equation C.8 in Equation C.5, the modal amplitude of each guided mode under the weakly guiding approximation is obtained:

$$a_{l,m} = \frac{\int_{A_\infty}\{\mathbf{E}_s(\rho,\phi)\times\mathbf{z}\times\mathbf{E}_{t,lm}^*(\rho,\phi)\}\cdot\mathbf{z}dA}{\int_{A_\infty}|\mathbf{E}_{t,lm}(\rho,\phi)|^2 dA} \tag{C.9}$$

Once the source field $E_s(\rho,\phi)$ is known, the modal amplitude depends exclusively on the transversal component of the electric field.

Appendix D

Coordinates System Conversion

In this work, it is assumed that the source field is launched from a single mode fiber, as it was mentioned in the section 3.3.1. In Figure D.1, a schematic representation of the SMF and MMF core radius is presented.

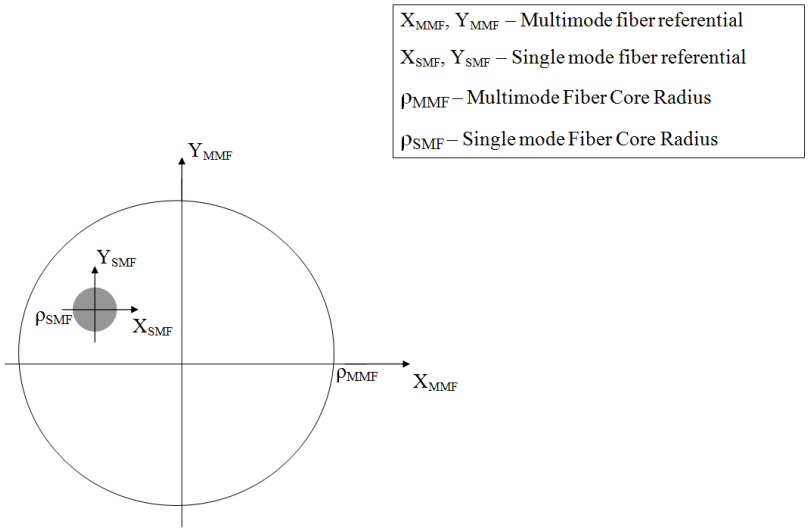

Figure D.1: Axial representation of the SMF and the MMF core radius.

As it is possible to see in Figure D.1, unless for the case of having centred launching conditions, the SMF and the MMF referential is not the same. So, in order to do the light launch from the SMF to the MMF, it is necessary to identify how they are related with each other.

In order to have a direct correspondence between the SMF and the MMF referentials, a coordinates system conversion is required. Figure D.2 shows the geometrical interpretation of the coordinates system conversion.

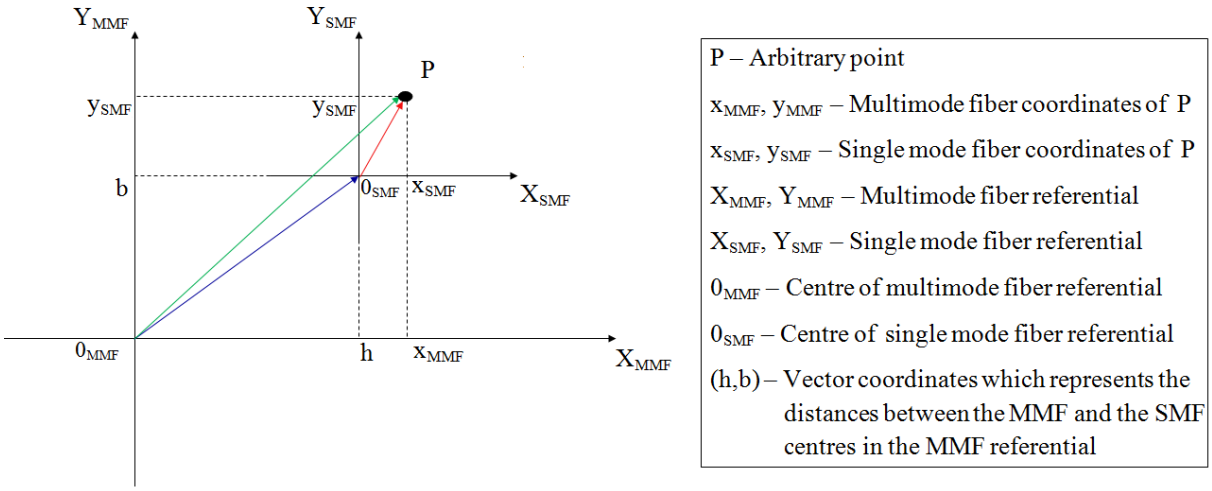

Figure D.2: Geometrical interpretation of the coordinates system conversion problem.

The first step is to determine the SMF coordinates as a function of the MMF coordinates. Assuming that the relative position of the two core centres is known:

$$(0_{MMF}, 0_{SMF}) = (h, b) \tag{D.1}$$

where h represents the horizontal coordinate and b represents the vertical coordinate of the vector that gives the distance between the two core centres, in the MMF referential. The SMF coordinates of a given arbitrary point P written as a function of its MMF coordinates, are given by the sum of the two vectors represented in blue and red in Figure D.1:

$$\overrightarrow{P} = (x_{SMF}, y_{SMF}) = (x_{MMF}, y_{MMF}) - (h, b) = (x_{MMF} - h, y_{MMF} - b) \tag{D.2}$$

Simplifying,

$$\begin{cases} x_{SMF} = x_{MMF} - h \\ y_{SMF} = y_{MMF} - b \end{cases} \tag{D.3}$$

Since the electromagnetic field used in the multimode fiber propagation model is presented in polar coordinates, it is necessary to convert the Cartesian coordinates of the point P into polar coordinates. In the Appendix A, the relationships between Cartesian and cylindrical coordinates are presented. Substituting Equation A.1 and Equation A.2 in Equation D.3, allows to determined a general expression to convert a point in the SMF referential to the MMF referential, in cylindrical polar coordinates is obtained:

$$r_{SMF} = \sqrt{r_{MMF}^2 - 2r_{MMF}(b\sin\phi_{MMF} + h\cos\phi_{MMF} + b^2 + h^2)} \tag{D.4}$$

$$\phi_{SMF} = \arctan \frac{r_{MMF} \sin \phi_{MMF} + b}{r_{MMF} \cos \phi_{MMF} + h} \tag{D.5}$$

Appendix E

Optimizations

In this chapter, the optimizations of the OFDM-UWB system over the multimode fiber are presented. In Section E.1, the optimization of the modulation index and the V_{bias} of the Mach-Zehnder modulator are presented. The optimization of the order of the interpolation polynomial used to determinate the equalizer transfer function is presented in Section E.2.

E.1 Mach-Zehnder Modulator

In order to improve the system performance, it is necessary to determine which is the modulation index and the V_{bias} point of the Mach-Zehnder modulator that leads to the best combination of the BER/SNR values. This combination will lead to the increase of the performance of the overall system. Table E.1 shows the results of the optimization of the Mach-Zehnder modulator. These optimizations are performed for a fiber length of 500 m and for a signal transmission on the third UWB sub-band, which is the sub-band that presents the highest value of BER.

Table E.1: Optimization of the modulation index and of the V_{bias} based on the BER and on the SNR of the overall system.

V_{bias}	Modulation Index [%]					
	2		10		30	
	BER	SNR [dB]	BER	SNR [dB]	BER	SNR [dB]
$\frac{V_\pi}{6}$	8.5×10^{-3}	9.3	2.6×10^{-7}	23.3	$< 10^{-20}$	32.4
$\frac{V_\pi}{3}$	2×10^{-5}	20.1	$< 10^{-20}$	33.9	$< 10^{-20}$	41.9
$\frac{V_\pi}{2}$	1.2×10^{-8}	24.9	$< 10^{-20}$	38.4	1.1×10^{-2}	44.8
$\frac{2V_\pi}{3}$	4.2×10^{-10}	26.1	$< 10^{-20}$	39.3	0.17	44.1
$\frac{5V_\pi}{6}$	2.6×10^{-7}	23.3	$< 10^{-20}$	36.0	0.31	39.3

Table E.1 shows that the values around $V_{bias} = \frac{V_\pi}{2}$ are the ones that present a better BER/SNR relation. This is expected since this is the most linear point of the Mach-Zehnder modulator characteristic. It is possible to see that the better results are achieved for the combinations: i) $V_{bias} = \frac{V_\pi}{2}$, modulation index= 10%, ii) $V_{bias} = \frac{2V_\pi}{3}$, modulation index= 10% and iii) $V_{bias} = \frac{V_\pi}{3}$, modulation index= 30%. As it was mentioned in Chapter 2, the increase of the modulation index and to place the V_{bias} point in a non linear region of the modulator characteristic, increases the fiber distortion, as it can be seen in Figure E.1 and in Figure E.2. So, the optimal values for the Mach-Zehnder modulator used in this work are $V_{bias} = \frac{V_\pi}{2}$, modulation index= 10%.

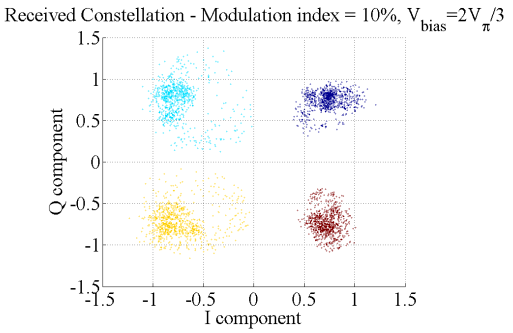

(a) Modulation Index = 10% , $V_{bias} = 2\frac{V_\pi}{3}$

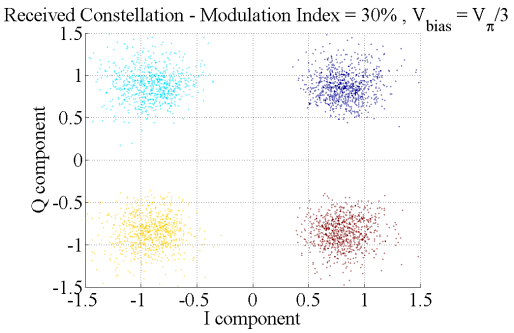

(b) Modulation Index = 30% , $V_{bias} = \frac{V_\pi}{3}$

Figure E.1: Received constellations for $V_{bias} = 2\frac{V_\pi}{3}$ and a modulation index of 10% and for $V_{bias} = \frac{V_\pi}{3}$ and a modulation index of 30%, respectively.

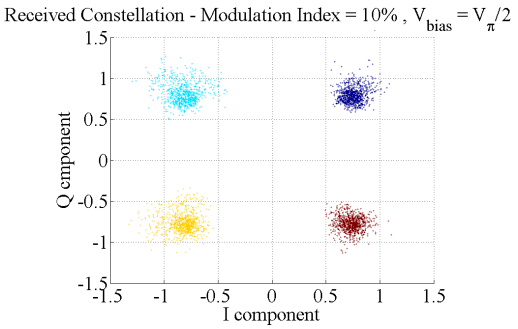

Figure E.2: Received constellation for a $V_{bias} = \frac{V_\pi}{2}$ and a modulation index of 10%.

E.2 Order of the polynomial interpolator used to estimate the equalizer transfer function

The overall system performance is very dependent on the equalization process of the transmitted signal. By changing the order of the polynomial used to perform the interpolation of the estimated channel between the pilots, it is possible to alter substantially the quality of the received signal. Table E.2 shows the BER and the SNR values obtained by changing the polynomial order of the equalizer for a fiber length of 500 m and signal transmission of the third UWB sub-band. The results present in E.2 were obtained for a launch power of 1 mW in the MMF.

Table E.2: Optimization of the polynomial interpolation order as a function of the SNR and of the BER of the overall system.

Equalizer order	BER	SNR [dB]
1	5.6×10^{-7}	37.6
3	$< 10^{-20}$	37.6
6	$< 10^{-20}$	37.6

The first obvious conclusion is that the change of the equalizer order does not change the SNR. This result is expected since the polynomial order does not affect the signal power. It is very clear from Table E.2 that a linear regression (which corresponds to use a polynomial order of 1) is not sufficient to have an acceptable BER. The other two values of the polynomial order used presented a good value of BER that are both inferior to $< 10^{-4}$. In order to decide which is the most appropriate value for the order of the polynomial interpolator of the equalizer, it is necessary to analyse the received constellations. Figure E.3 show the received constellation for a polynomial interpolation of order 1 and 6.

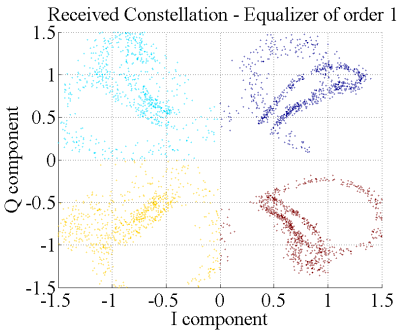

(a) Equalizer of order 1.

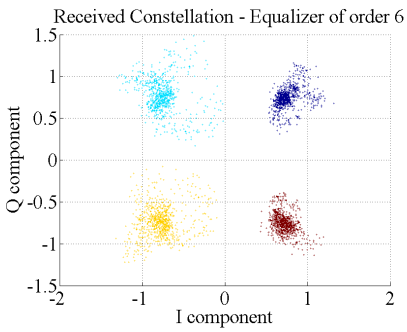

(b) Equalizer of order 6.

Figure E.3: Received constellations for a fiber length of 500 m and signal transmission on the third UWB sub-band and for a interpolation polynomial of order 1 and 6.

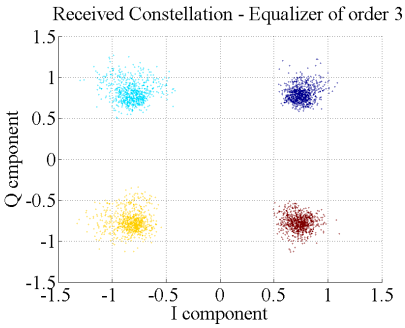

Figure E.4: Received constellations for a fiber length of 500 m, and signal transmission on the third UWB sub-band and for interpolation polynomial of order 3.

Comparing Figure E.4 with Figure E.3, it is possible to see that the received constellation for a equalizer of order 3 is the one that presents better a better result. So, the optimal order of the equalizer used in this work is 3.

Bibliography

[1] Webb and Associates. The 1930s (The Great Depression: Rebuilding). *on http://www.webbconsult.com/1930.html*, October 2010.

[2] Webb and Associates. The 1920s (The Roaring Twenties). *on http://www.webbconsult.com/1920.html*, October 2010.

[3] Webb and Associates. The 1960s (Into a New Age of Technology). *on http://www.webbconsult.com/1960.html*, October 2010.

[4] Webb and Associates. The 1970s (Growth and Regulation). *on http://www.webbconsult.com/1970.html*, October 2010.

[5] Webb and Associates. The 1980s (Divestiture and a "Whole New Ballgame"). *on http://www.webbconsult.com/1980.html*, October 2010.

[6] AT&T. Inventing the Telephone. *on www.corp.att.com/history/inventing.html*, October 2010.

[7] V. Alwayn. Fiber-Optic Technologies - A Brief History of Fiber-Optic Communications. *on www.ciscopress.com/articles/article.asp?p=170740,ciscopress*, October 2010.

[8] S. Kuram. Advantages of the optical fibers - Optical fibers communications. *on http://knol.google.com/k/sudharani-kuram/advantages-of-optical-fibres/3tq1bhnm4l2up/6*, October 2010.

[9] B. Leiner, V. Cerf, D. Clark, R. Kahn, L. Kleinrock, D. Lynch, J. Postel, L. Roberts and S. Wolff. A Brief History of the Internet. *on www.isoc.org/internet/history/brief.shtml*, October 2010.

[10] K. Coffman and A. Odlyzko. Growth of the Internet - in Optical Fibre Telecommunications. *Academic Press*, IVB, 2002.

[11] PT Comunicações. A melhor fibra aos melhores preços. *on http://www.meo.pt/aderir/fibra/pacotes/Pages/tvnetvoz.aspx*, October 2010.

[12] Zon Multimédia. Pacotes de canais - Grelha digital cabo. *on http://www.zon.pt/Televisao/cabo/canaisporpacote.aspx*, October 2010.

[13] Digital Tv Europe.net. Play it again. *on http://www.digitaltveurope.net/feature/29-sep-10/play-it-again*, October 2010.

[14] PT Comunicações. 3D no meo. *on http://www.meo.pt/conhecer/tv/3d/Pages/default.aspx*, October 2010.

[15] Zon Multimédia. Decida o que quer ver. *on http://www.zon.pt/Videoclube/IntroducaoVideoclube.aspx*, October 2010.

[16] ARC Electronics. Brief over view of fiber optic cables - advantages over copper. *on http://www.arcelect.com/fibercable.htm*, October 2010.

[17] C. Tsekrekos. Mode group diversity multiplexing in multimode fiber transmission systems. *on http://alexandria.tue.nl/extra2/200712406.pdf*, October 2010.

[18] R. Paschotta. Encyclopedia of Laser Physics and Technology. *Wiley-VCH*, October 2008.

[19] C. Duan et al. Transmitting Multiple HD Video Streams over UWB links. *Consumer Communications and Networking Conference*, 2006.

[20] FCC 02-48. Revision of Part 15 of the Commission Rules Regarding Ultra-Wideband Transmission Systems. *FCC*, April 2008.

[21] M. Benedetto and G. Giancola. Understanding Ultra Wideband Radio Fundamentals. *Prentice Hall*, July 2004.

[22] R. Llorente, T. Alves, M. Morant, M. Beltran, J. Perez, A. Cartaxo and J. Marti. Optical Distribution of OFDM and Impulse Radio UWB in FTTH Networks. *OFC/NFOEC*, 2008.

[23] A. Cartaxo. OFDM-based optical communications systems. February 2010.

[24] J. Armstrong. OFDM for Optical Communications. *Journal of Lightwave Technology, vol:27*, pages 189–204, 2009.

[25] E. Schubert. Light Emitting-Diodes. *Cambridge University press*, June 2006.

[26] Arden Photonics. Modal launch conditions - measurement and control . *on www.ardenphotonics.com/datasheets/wpmodcon.pdf*, June 2010.

[27] J. Balakrishnan A. Batra and A. Dabak. Multiband OFDM: Why it Wins for UWB. *EETIMES Design*, June 2003.

[28] T. Alves and A. Cartaxo. Performance Degradation Due to OFDM-UWB Radio Signal Transmission Along Dispersive Single-Mode Fiber. *IEEE Photonics Technology Letters, vol.21, No.3*, pages 158–160, February 2009.

[29] G. Agrawal. Lightwave technology components and devices. *John Wiley & Sons*, pages 37–52, 2005.

[30] A. Cartaxo. Transmissão por fibra optica. *IST - folhas de apoio a disciplina de sistemas e redes de telecomunicações*, March 2005.

[31] T. Alves and A. Cartaxo. Semi-analytical approach for performance evaluation of direct-detection OFDM optical communication systems . *Optics Express, Vol. 17*, pages 18714–18729, 2009.

[32] A. Snyder and J. Love. Optical Waveguide Theory. *Chapman and Hall, Ltd*, pages 205–335, 1983.

[33] D.Marcuse. Theory of Dielectric Optical Waveguides. *Academic Press, Inc*, pages 60–82, 1991.

[34] S. Bottacchi. Multi-gigabit Transmission Over Multimode Optical Fiber: Theory and Design Methods for 10 GbE Systems. *John Wiley & Sons, Inc.*, pages 307–374, 2006.

[35] Corning - White paper. TIA-568 Rev. C Impact on Optical Connectivity. *on http://catalog2.corning.com/CorningCableSystems/media/NAFTA/White_ Papers/LAN-1135-EN.pdf*, page 3, April 2009.

[36] A.Castro,V. Teichman,D. Mello and A.Cartaxo. Impact of the Launch Conditions on the Transfer Function of Multimode Fibers. *Porto*, June 2010.